Beata Tyburska

**Deuterium Retention in Carbon and
Self-Implanted Tungsten**

Marie Curie-Skłodowska University
Department of Mathematics,
Physics, and Computer Science

Beata Tyburska

Deuterium Retention in Carbon- and Self-Implanted Tungsten

Retencja deuteru w próbkach wolframu
implantowanych jonami węgla i wolframu

Dr hab. Jerzy Żuk, prof. UMCS
Marie Curie-Skłodowska University, Lublin, Poland

Dr. Karl Ertl
Max Planck Institute for Plasma Physics, Garching, Germany

Lublin 2010

To my beloved Moritz

Abstract

Due to its favorable physical properties, like low erosion yield and high melting temperature, tungsten is employed as a plasma-facing component in both current and future fusion devices, such as ASDEX Upgrade and Iter. Deuterium retention in undamaged tungsten has been observed to be sufficiently low to not become a concern, but some uncertainty remains regarding the influence of damage caused by 14 MeV fusion neutrons. In order to properly predict the tritium inventory in Iter, the time and temperature dependencies of damage development, the trap density, and the tritium behavior in the presence of superabundant defects have to be known. The estimated damage in Iter at the end of its lifetime is 0.4 dpa for an assumed threshold energy $E_{th} = 68$ eV for the displacement of W atoms.

The production of n-induced defects was simulated by means of tungsten self-implantation at three different fluences which correspond to three damage levels of 0.04, 0.4, and 1.2 dpa (displacements per atom) in the maximum of the damage profile. After tungsten pre-irradiation, some of the samples were heated at 1200 K for 2 h in order to investigate the annealing of radiation-induced defects. Both sets of samples were either implanted with deuterium ions or exposed to deuterium plasmas at two temperatures. For the purpose of comparison, D implantation into undamaged tungsten was investigated in a similar fashion.

The deuterium depth profiles were measured by means of NRA, using the $D(^3He,\alpha)p$ reaction, and the D desorption was measured with TDS. The surface morphology was investigated by means of SEM/FIB.

Using this setup, it is found that deuterium is mostly retained in traps created by pre-irradiation. This increases the D retention in the damaged zone by a factor of five to eight in comparison with undamaged W. The D inventory does not grow linearly with dpa but approaches saturation at 0.4 dpa with a D/W ratio of 1.6%. TDS spectra reveal that the ion pre-irradiation produces traps with desorption temperatures of ~ 530 and ~ 820 K. The lower temperature corresponds to D de-trapping from interstitial-type dislocation loops, the higher one to de-trapping of deuterium decorating the walls of vacancy clusters. Around 30% of the retained D is trapped in high-energy defects.

In the presence of defects, D diffusion will be slower. To account for this effect, the trapping of permeating deuterium in defects induced in the rear side of tungsten samples was studied. The front side of each sample was exposed to a deuterium plasma at elevated temperatures of $460 - 755$ K. Additionally, this experiment made it possible to separate the effect of plasma interaction with defects and measure the "pure" trap density. The results show that D atoms diffuse through the whole width of the sample

and are trapped in vacancies and vacancy clusters. The highest D retention and trap density of $0.57\,$at.% was measured at $460\,$K—beyond that point, due to the de-trapping process, it decreases with increasing irradiation temperature.

In Iter's divertor, not only W but also carbon fiber composite will be present which will lead to the formation of W-C mixed materials. To measure the influence of C on the D retention, pure W samples were damaged by C ions and then irradiated by D. The main conclusion from these measurements is that in the presence of C, deuterium diffusion is hindered, possibly due to WC formation.

The NRA and SEM results suggest that the worst operation temperature for a thermonuclear reactor would lie around $460 - 550\,$K; while in order to keep the deuterium retention low and to avoid tungsten blistering, the effective temperature at the tungsten surface should be adjusted to values above $800\,$K.

Streszczenie

W reaktorze termojądrowym Iter planuje się użycie wolframu jako materiału stykającego się z plazmą przy konstrukcji między innymi przegrody diwertora oraz kopuły. Zaobserwowany poziom retencji deuteru w nieuszkodzonym radiacyjnie wolframie okazuje się być niski, jednak brakuje informacji, jak wpływają na niego uszkodzenia radiacyjne powodowane przez neutrony. Podczas pracy reaktora uszkodzenia te spowodowane są neutronami o energii 14 MeV, które wprowadzają pułapki w objętosci materiału. Szacuje się, że poziom uszkodzeń w reaktorze Iter na koniec jego okresu pracy osiągnie wartość 0.4 dpa (liczba przemieszczonych atomów na atom materiału). Dlatego też w eksperymencie zdecydowano się symulować uszkodzenia wywołane neutronami poprzez implantację jonów wolframu o energii 5.5 MeV i jonów węgla o energii 0.5 MeV do płytek wolframowych w temperaturze pokojowej dla różnych dawek odpowiadających 0.04 do 50 dpa. Dla porównania zbadano także nieuszkodzony radiacyjnie wolfram. Po wstępnej implantacji jonami W niektóre z próbek W zostały wygrzane w temperaturze 1200 K przez 2 h w celu usunięcia defektów radiacyjnych. Tak przygotowane próbki były albo zaimplantowane jonami deuteru lub też poddane działaniu plazmy deuterowej dla wysokiej dawki. Te naświetlania przeprowadzono dla temperatury próbki 470 K lub w temperaturze pokojowej.

Profile głębokościowe deuteru w wolframie były otrzymywane przy użyciu techniki NRA (Nuclear Reaction Analysis) stosując reakcję $D(^3He,\alpha)p$, natomiast wartości temperatury desorpcji deuteru wyznaczono z pomiarów TDS (Thermal Desorption Spectroscopy). Morfologia powierzchni próbek była zbadana metodą mikroskopii SEM/FIB (Scanning Electron Microscope/Focused Ion Beam).

Otrzymane wyniki wskazują, że deuter jest przede wszystkim zatrzymywany w nowopowstałych pułapkach. Zaobserwowano pięcio- do ośmiokrotny wzrost poziomu retencji deuteru w stosunku do nieuszkodzonego wolframu. Ilość deuteru nie wzrasta liniowo z dpa ale zaczyna osiągać nasycenie przy 0.4 dpa. Stosunek koncentracji deuteru i wolframu utrzymuje się wtedy na poziomie 1.6%. Widma TDS pokazują, że wakanse i klastry wakansów odpowiadają za pułapkowanie deuteru.

Wzrost retencji deuteru w wolframie zaimplantowanym węglem do głębokości 700 nm jest porównywalny z wynikami otrzymanymi dla tychże próbek po implantacji wolframem. Poza tym obszarem koncentracja D szybko spada poniżej poziomu detekcji. To oznacza, że obecność węgla hamuje dyfuzję deuteru w głąb wolframu. Dzieje się tak, ponieważ współczynnik dyfuzji deuteru w węglu jest bliski zeru.

W obecności defektów dyfuzja deuteru będzie wolniejsza. Żeby zbadać ten efekt, pułapkowanie deuteru dufundującego do defektów wprowadzonych na tylniej stronie próbki

było badane. Przednia strona była poddana działaniu plazmy deuterowej przy temperaturach od 460 do 755 K. Rezultaty pokazują, że deuter jest w stanie przeniknąć przez nawet grubą próbkę i jest spułapkowany w defektach radiacyjnych. Największa gęstość pułapek 0.57% została zmierzona dla temperatury 460 K i wraz z rosnącą temperaturą spadała.

Zaprezentowane wyniki pokazują, że najbardziej niekorzystny zakres temperatur to 460−550 K i reaktor termojądrowy powinien pracować przy temperaturze powyżej 800 K aby utrzymywać niski poziom retencji deuteru i uniknąć pęcherzykowania powierzchni.

Contents

Abbreviations

CFC	carbon fiber composite
d	diffusion-limited release
D	diffusivity
dpa	displacement per atom
e^-	electron
E_n	neutron energy
E_T	trap energy
E_{th}	displacement energy threshold
FIB	Focus Ion Beam
FIM	Field Ion Microscopy
FP	Frenkel pair
HCS	High Current Source
I	interstitial site
IBA	Ion Beam Analysis
IC	interstitial cluster
IRM	Isochronal Resistivity Measurements
K_r	recombination rate coefficient
K_T	trap equilibrium constant
J	deuterium incident flux
NRA	Nuclear Reaction Analysis
NRT	Norgett-Robinson-Torrens model
N_W	tungsten atomic density, $6.32 \times 10^{28}\,\mathrm{m^{-3}}$
o	octahedral site
p	proton
Φ	deuterium incident fluence

|	
PA	Positron Annihilation
PCW	policrystalline tungsten
PFC	plasma-facing component
PKA	primary knock-on atom
PWI	plasma wall interaction
r	recombination-limited release
ρ_{tr}	trap density
RBS	Rutherford backscattering
R_{p}	projected range
RT	room temperature
S	solubility
SCW	single crystal tungsten
SEM	Scanning Electron Microscope
SOL	scrape-off layer
SRIM	Stopping and Range of Ions in Matter
t	tetrahedral site
T_{PKA}	PKA energy
θ	backscattering angle
T_{D}	desorption temperature
TDS	Thermal Desorption Spectroscopy
TEM	Transmission Electron Microscope
T_{irr}	irradiation/exposure temperature
T_{m}	tungsten melting temperature
V	vacancy site
VC	vacancy cluster

Chapter 1

Introduction

An increasing global energy demand, depleting fossil fuel resources, and concerns over carbon emissions call for new, sustainable energy sources. At present, renewable energies and fission are available. However, the first suffer from low efficiency and high costs, whereas the latter's biggest problem is the radioactive waste disposal and a lack of public endorsement. Nuclear fusion has the potential to overcome these obstacles. It is designed to provide large scale energy production with no emission of greenhouse gases. The fusion process is inherently safe because it is not based on a runaway chain reaction, and it produces waste which will not be a burden for future generations. However, humanity still has to wait for a few decades for its commercial development.

1.1 Fusion

Nuclear fusion is a process which occurs naturally in the core of the Sun where energy is produced via the proton-proton (p-p) chain reaction. Due to this reaction's reliance on the weak interaction, it is a rather slow process which is responsible for the long lifetime of the Sun. The enormous mass of the Sun makes up for that and allows for its vast energy production, but in reactors on Earth, such a mass is not be feasible, and therefore, the weak interaction has to be avoided. Terrestrially, the power will have to be obtained via the nuclear reaction between two hydrogen (H) isotopes, deuterium (D) and tritium (T):

$$^{2}_{1}\text{D} + {}^{3}_{1}\text{T} \rightarrow {}^{4}_{2}\text{He}\,(3.5\,\text{MeV}) + {}^{1}_{0}\text{n}\,(14.1\,\text{MeV}) \tag{1.1}$$
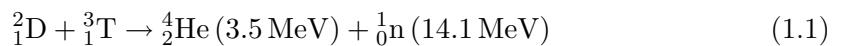
This is the most efficient of all fusion reactions, as it requires the lowest temperature to ignite and produces the most energy. The products of this reaction, namely helium (He) and neutrons (n), carry enormous amounts of energy, part of which can be converted
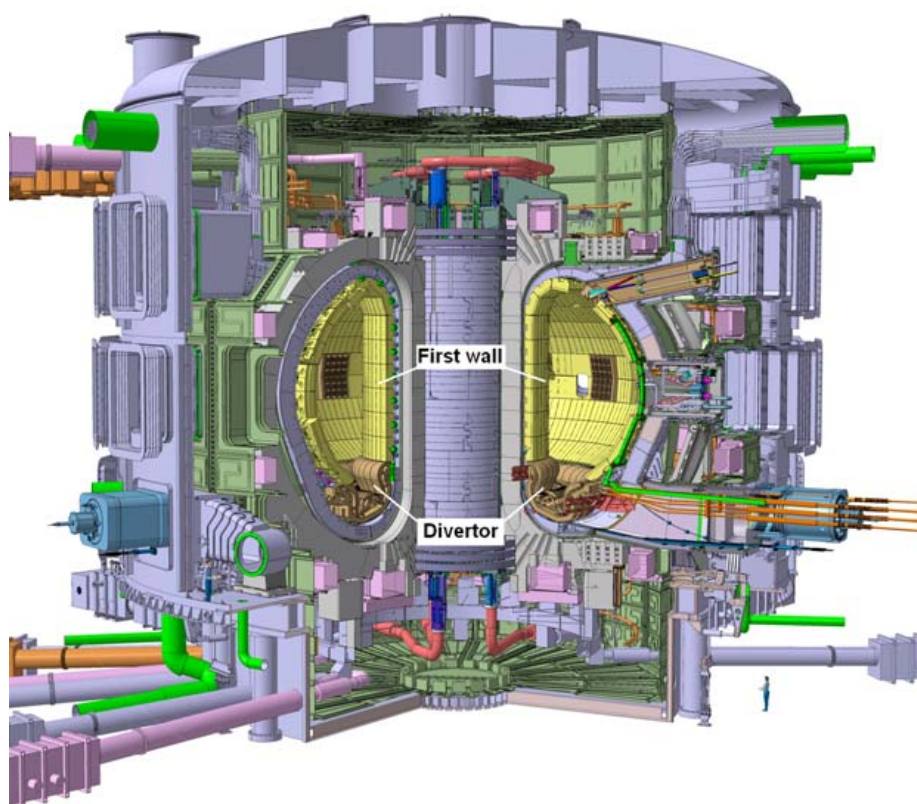
Figure 1.1: Cross-section view of Iter. The person in the lower right corner is included to provide a scale. Source: [1]

to electricity using conventional steam turbines. D is abundant in water $(30\,\mathrm{g/m^3})$ and can be extracted via electrolysis. T does not exist in nature and has to be bred from natural lithium $(\mathrm{n} + {}^7\mathrm{Li} \rightarrow {}^4\mathrm{He} + \mathrm{T} + \mathrm{n})$ which is found in the Earth's crust and brines. This gives us a practically inexhaustible, widely available fuel, the supply of which is not controlled by any single country.

Among other devices, nuclear fusion has already been tested in machines called toka-maks, albeit with negative energy output. Iter (see Fig. 1.1), from Latin "the way" (formerly: International Thermonuclear Experimental Reactor), is an international re-search project which, currently, is under construction in Cadarache, France. Iter's objectives are to prove the scientific and technological feasibility of fusion power, to integrate and test all crucial reactor technologies and components, and to demonstrate the positive safety and environmental properties of fusion. It is designed to be the
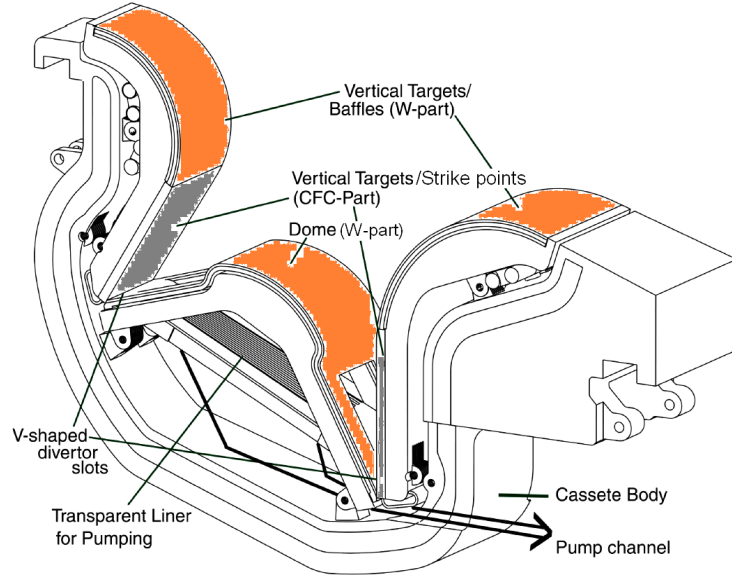
Figure 1.2: Divertor PFC arrangement in Iter. The orange color corresponds to W at the dome and baffles, and grey to CFC at the strike points. Source: [2].

first reactor which will exceed the so-called break-even point—the condition at which positive net power is reached. Iter is meant to be the final step before building DEMO (a DEMOnstration power plant), the first fusion reactor designed for electrical power generation. D-T fuel will be introduced into the empty torus and then ionized to form plasma using an electrical discharge. The plasma will then be heated up to 150 MK using ohmic heating, neutral beam injection, and high frequency electromagnetic waves [1].

No material is able to withstand such high temperatures. Therefore, a strong magnetic field will be required to keep the hot plasma away from the torus walls. Nonetheless, due to the slow particle diffusion across the toroidal field lines, some plasma wall interaction (PWI) will be inevitable. A region that has to be able to withstand particularly large fluxes is the divertor (see Fig. 1.2) where vertical targets interact directly with the scrape-off layer (SOL) plasma. The materials which have direct contact with the plasma, the so-called plasma-facing components (PFCs), will face a number of challenges. Firstly, they have to handle large power densities due to the bombardment of the surface by fusion neutrons, charged plasma particles, and photons. Secondly, particle irradiation will lead to surface erosion, which determines the lifetime of the PFCs and is a source of dust. Deposition of these impurities onto PFCs alters their surface

dpa ($E_{\text{th}} = 68\,\text{eV}$)	0.4
neutron wall loading	$0.4\,\text{MW/m}^2$
neutron fluence	$3.5\times10^{21}\,\text{cm}^{-2}$
operation time	$2\times10^7\,\text{s}$
temperature	$440 - 760\,\text{K}$
D/T flux	$10^{22} - 10^{23}\,\text{m}^{-2}\text{s}^{-1}$
energy	$15 - 500\,\text{eV}$

Table 1.1: Assessment of the conditions for tungsten in Iter's divertor. The upper part of the table considers neutrons and the given values were estimated at the end of Iter's lifetime. The lower part gives the parameters of DT plasma. Sources: [4–7]

composition and, in consequence, their physical properties. Retention and recycling of radioactive tritium ($T_{1/2} = 12.3\,\text{yrs}$) from PFCs presents a safety concern – which stems from the contamination of the PFCs and the coolant – and affects fueling efficiency. The total in-vessel T inventory which is allowed for Iter is $700\,\text{g}$ [3]. Additionally, the choice of materials is constrained by the requirement that they must not produce long-lived radioactive waste when being irradiated by neutrons. The final selection of materials is $700\,\text{m}^2$ beryllium (Be) in the main vessel, $50\,\text{m}^2$ of carbon fiber composite (CFC) at the vertical targets, and around $210\,\text{m}^2$ of tungsten (W) in the divertor (at the dome, baffles) and limiter.

1.2   Tungsten as a Material for Iter's Divertor

Iter's divertor is segmented into 54 cassettes [6]. Its main function is to extract He and impurity particles from the plasma, while minimizing the impurity influx to the plasma. The divertor's PFCs are in direct contact with the SOL and therefore have to be able to withstand large power densities (up to $20\,\text{MW/m}^2$) and D/T particle fluxes ($10^{22} - 10^{23}\,\text{m}^{-2}\text{s}^{-1}$; see Tab. 1.1) from the plasma. As previously mentioned, W will be present in the dome and baffle areas, a refractory metal with the highest melting point ($3683\,\text{K}$) among all elements. It has been chosen as a divertor PFC because of its high thermal conductivity ($155\,\text{W/mK}$) and high thermal stress resistance. Among the materials which were chosen for Iter's first wall, it has the highest threshold for sputtering which leads to a high resistance to ion and charge exchange particle erosion. It is estimated that by keeping the tritium energy below $700\,\text{eV}$, the erosion would be avoided completely. W does neither form hydrides nor co-deposits with T, and it

shows low T retention while revealing a strong resilience against neutron irradiation and activation. However, tungsten also has several negative features. One of the problems lies in excessive radiation losses due to the accumulation of W in the plasma caused by transient events such as edge localized modes (ELMs) and disruptions. According to the Nuclear Analysis Report [5], during each of the planned operational campaigns – i.e., 0.63 of a full power year (FPY), corresponding to 2×10^7 s – tungsten will be exposed to 14 MeV neutrons to a fluence of 3.5×10^{21} cm^{-2} (see Tab. 1.1), which corresponds to a damage level of 0.4 displacements per atom (dpa) for the displacement energy threshold $E_{\text{th}} = 68$ eV (see Ch. 3). This will lead to a deterioration of the mechanical properties of the material and – like in all bcc metals – will cause embrittlement and, in consequence, delamination. Additionally, there are concerns about surface cracking and blistering due to D/T implantation at the expected fluxes and exposure temperatures (see Tab. 1.1). To avoid these effects, it is recommended to use a material with the grain orientation parallel to the heat flow [8]. Another problem with tungsten is the formation of oxide layers due to a strong chemical affinity to oxygen. Furthermore, oxide layers can be formed due to O$_2$ gas introduction into the reactor chamber for tritium removal. As a result of the reduction of the binding energy of tungsten oxide molecules, the presence of the oxide layer on the surface causes a decrease of the threshold energy for the sputtering of W by hydrogen [9].

Despite these difficulties, W was successfully tested in ASDEX Upgrade, an all-W, divertor tokamak. During the operation phase, W erosion takes place, but the plasma contamination by W was found to be small [10] and can even be reduced by optimizing certain plasma parameters. There are plans to test W under Iter-like conditions which may be the basis for using only W-based armor in future reactors.

1.3 Motivation for the Thesis

As a plasma-facing material, W will be subjected to intense fluxes of energetic deuterium and tritium particles, as well as 14 MeV neutrons. Due to the rather weak interaction of neutrons with the wall material, the introduced defects will be distributed volumetrically throughout the entire thickness of the tungsten components. The International Fusion Materials Irradiation Facility (IFMIF) is currently under construction and is designed to test the materials for use in the Iter reactor. The main idea behind this project is to use an accelerator-based neutron source which can deliver large highly energetic neutron fluxes to create damage in those various materials. The first operation phase is planned for 2013, and until then, other methods have to be considered to simulate

the production of n-induced defects in tungsten. There have already been attempts to characterize n-induced defects in W by exposing it to fission neutrons, but the problem is that these neutrons have much lower energies and a broader spectrum than the monoenergetic fusion neutrons. Additionally, simulating n-induced damage by fission neutrons is costly, time consuming, and activates the irradiated material. Therefore, other particles have to be used as surrogates. Deuterium retention and diffusion in W damaged by protons [11–15], electrons [15], and heavy ions [16] have already been investigated. Unfortunately, the results are very scattered, and there is no agreement as to in what kinds of defects D is trapped and what the de-trapping energy from ion-induced defects is. This is probably due to the differences in damage morphology for the various types of damaging particles.

In this work, tungsten and carbon ions were used to simulate the damage morphology typical for neutron irradiation, i.e.: dense cascades with large vacancy clusters were generated. The presence of CFC at the vertical target strike points is a consequence of its resilience to high heat fluxes and temperatures. During exposure to the plasma, not only mixed W/C materials but also ion-induced defects are created by both fuel and PFC particles. Tritium inventory calculations [16–18] are based on experimental results in mono-materials. The combination of self- and C-implantation allows discriminating between chemical effects and damage-induced changes of the D retention. The irradiation parameters were chosen in such a way that the damage level is comparable to the one which is estimated for W in Iter (see Tab. 1.1). This implies that the fluences used for C pre-implantation are irrelevant to Iter. The purpose of using carbon is to study its impact on D retention. Therefore, the C and W ion energies were chosen in such a way that the created damage zones were similar, which means that the energy of the C ions is much higher than it would be in Iter.

The goal of this thesis is to answer the question what kind of defects are present in tungsten after heavy ion irradiation and how they are redistributed. Studies of the influence of ion-induced defects on D retention as a function of the dpa are performed to further the understanding of how the trap concentration develops with time. Since T is radioactive, and thus not used in many present-day fusion experiments, D was employed to study its retention in relation to the damage level, deuterium fluence, and irradiation temperature. Again the chosen experimental parameters are comparable to those in Iter. The total T retention in Iter will depend not only on the amount of available defects which serve as traps but also on the T diffusion rate to these traps. D diffusion in undamaged W is rather fast, but the presence of ion-induced traps may hinder it.

Ch. 3 provides a foundation of how defects are produced in the material and – by comparing the damage morphologies created by different types of particles – tackles the question if heavy ions are a good proxy for neutrons. The methods and facilities which were used in these studies are described in Ch. 4. All experimental results from self-implanted and carbon-implanted tungsten are collected in Chs. 5 and 6, respectively. In Ch. 7, it is investigated whether D would be able to populate all accessible traps. This is done by measuring the D permeation to the defects which were introduced in the rear side of the 25 and $500\,\mu$m samples. All results are summarized in Ch. 8.

Chapter 2

Background

2.1 Plasma-Tungsten Interaction

During tokamak operation, interactions between the plasma and the PFCs are inevitable. It is a very dynamic, non-equilibrium process, influencing the retention of hydrogen isotopes and recycling (see Fig. 2.1).

The processes which govern plasma recycling are reflection and recombination. High recycling increases the fuel rate, but at the same time lowers the temperature of the plasma due to the re-insertion of cold hydrogen isotopes. The amount of kinetically reflected particles depends on their energy and the type of the irradiated material, e.g.: for W implanted with $200\,\mathrm{eV}$ D ions the reflection coefficient is $r = 0.56$ [19]. The remaining part is implanted (up to $\sim 15\,\mathrm{nm}$ for the D-T energies given in Tab. 1.1) and then trapped in intrinsic and n-induced defects. According to SRIM calculations [20], no radiation defects are induced by a D-T plasma with the energies given in Tab. 1.1. Tungsten has a low solubility for hydrogen isotopes (see Sec. 2.3), and therefore, the hydrogen deposited in the implanted zone is trapped not only in atomic form but also as molecules [21, 22]. As soon as the concentration of the implanted particles in the stopping zone reaches saturation, they begin to diffuse toward the surface or into the bulk. Atoms migrating outward have to undergo recombination before being re-emitted from the surface. It depends on the magnitude of the recombination rate whether the release will be rapid and – in consequence – the surface concentration low, or if the release will be slow and the hydrogen inventory and possibly the permeation large. Particles moving inward may be trapped or may permeate through the entire material, which, in the case of permeating tritium, may lead to contamination of the coolant. Trapping and diffusion control the retention of hydrogen isotopes, which due to the fuel cost and safety limits, should be kept low. Tungsten present in the divertor will
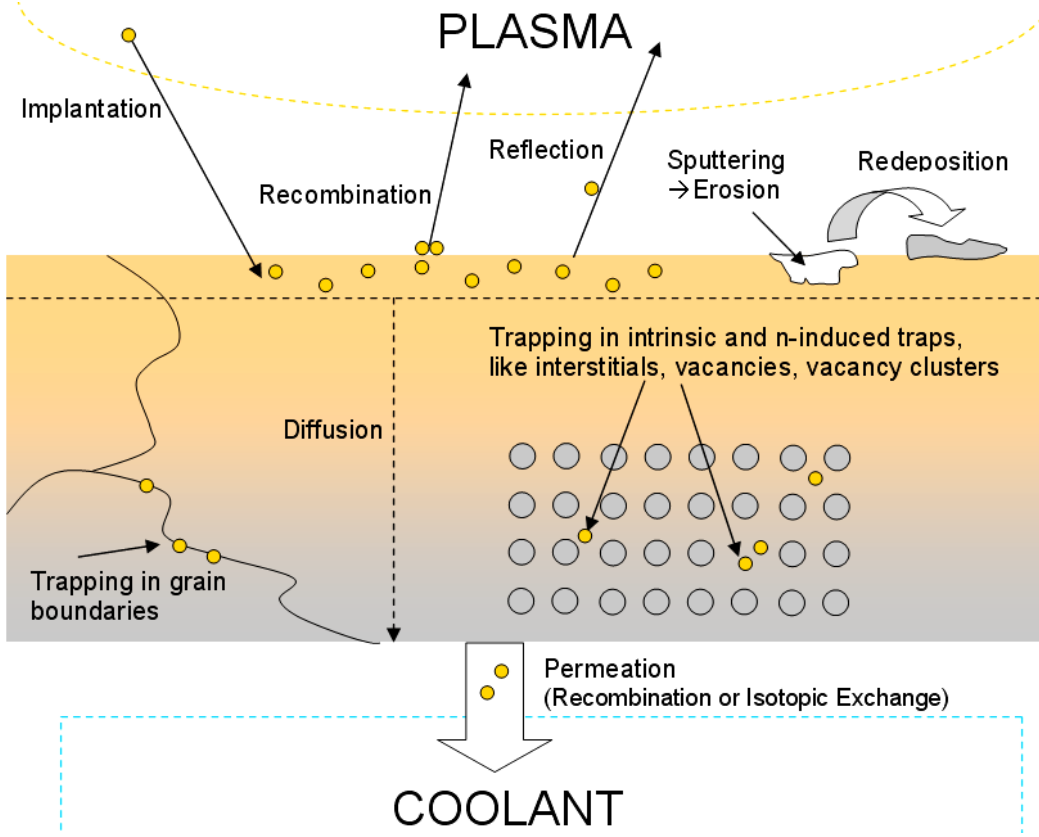
Figure 2.1: Plasma interaction with PFCs.

also be physically sputtered which may lead to material erosion. This would result in a reduction of the material's lifetime and in a contaminating release of heavy tungsten atoms into the plasma, as well as in the formation of mixed materials due to material co-deposition. By keeping the tritium energy below $700\,\mathrm{eV}$, erosion can be avoided [23].

2.2   Hydrogen Transport

Fick's second law describes the change of the H concentration with time and depth:

$$\frac{\partial C}{\partial t} = D\frac{\partial^2 C}{\partial x^2} + G(x,t) \tag{2.1}$$

where C is the H concentration in solution, D is the diffusion rate, and $G(x,t)$ is a H source term. For steady state ($\partial C/\partial t = 0$), the situation is illustrated in Fig. 2.2. To allow easier calculations, some assumptions can be made [24, 25]:
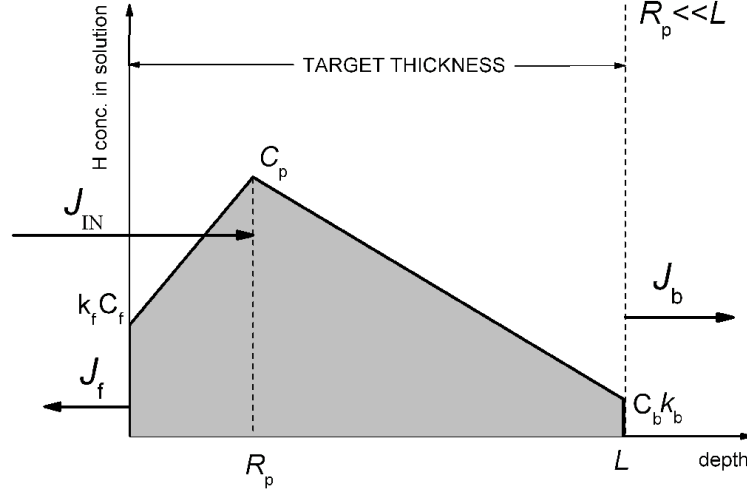
Figure 2.2: Hydrogen solute concentration as a function of depth during steady-state without trapping (not to scale). All parameters are explained in the text. The arrows marked J indicate the relevant in- and outward fluxes. The dashed lines mark the projected range.

- The projected incident ion range R_p is much smaller than the thickness of the wall ($R_p \ll L$). This condition will be fulfilled for Iter ($R_p \sim 15\,\text{nm}$, $L \sim 1\,\text{cm}$).

- The diffusion rate D is constant.

- The deposited flux J_{IN} is constant.

- The implanted range distribution is a δ-function (no range straggling) at a projected ion range $x = R_p$. Thus, the H source term can be written as $G(x) = J_{\text{IN}}\delta(x - R_p)$.

- Trapping is not included.

- The boundary conditions are:

$$J_{\text{IN}} = J_f + J_b \tag{2.2}$$

$$J_f = k_f C_f^2 = D \left. \frac{\partial C}{\partial x} \right|_{x=0} = \frac{D(C_p - C_f)}{R_p} \tag{2.3}$$

$$J_b = k_b C_b^2 = D \left. \frac{\partial C}{\partial x} \right|_{x=L} = \frac{D(C_p - C_b)}{L} \tag{2.4}$$

Here, J_f and J_b denote the H flux towards the front (recycled flux) and back surface (permeated flux), respectively. They are rate-limited by diffusion (d) and/or recombi-

nation (r) on both sides. k_f and k_b are phenomenological recombination coefficients for the front and back site of the wall, respectively; C_f and C_b are the hydrogen surface concentration in the front and back of the wall, respectively; and C_p is the H concentration at a depth of $x = R_p$.

For the purpose of simplification, it is useful to introduce some dimensionless parameters:

$$u \quad = \quad C_f\sqrt{\frac{k_f}{J_{IN}}} \tag{2.5}$$

$$v \quad = \quad C_b\sqrt{\frac{k_b}{J_{IN}}} \tag{2.6}$$

$$\alpha \quad = \quad \frac{R_p}{L} \tag{2.7}$$

$$\gamma \quad = \quad \sqrt{\frac{k_f}{k_b}} \tag{2.8}$$

$$W \quad = \quad \frac{R_p}{D}\sqrt{k_f J_{IN}} \tag{2.9}$$

Then C_f, C_p, and C_b can be expressed as:

$$C_f \quad = \quad \sqrt{\frac{J_{IN}}{k_f}}\sqrt{1 - v^2} \tag{2.10}$$

$$C_p \quad = \quad \sqrt{\frac{J_{IN}}{k_f}}\left[\left(\frac{W}{\alpha\gamma}\right)v^2 + v\right]\gamma \tag{2.11}$$

$$C_b \quad = \quad \sqrt{\frac{J_{IN}}{k_f}}\gamma v \tag{2.12}$$

Here, W is a factor which describes the conversion from diffusion- to recombination-limited release. Since it depends on the projected range R_p (i.e., the incident energy of the ions) and the deposited flux J_{IN}, by changing these values a transition from diffusion- to recombination-limited transport can occur. Doyle [24] distinguishes three situations:

1) *dd-regime*: $W > 1$ (i.e., $C_f \approx 0$ and $C_b \approx 0$)—the H release is diffusion-limited on both sides,

2) *rd-regime*: $\gamma^2\alpha < W < 1$ (i.e., $C_p \approx C_f$ and $C_b \approx 0$)—the front surface is recombination-limited and the back surface diffusion-limited, and

3) *rr-regime*: $W < \gamma^2\alpha$ (i.e., $C_p \approx C_f \approx C_b$)—the H release is recombination-limited on both sides.

The previous assumption of a constant diffusion rate does not account for a *dr-regime* in this model. Shu et al. [26] assumed the diffusivity to be different at the front and
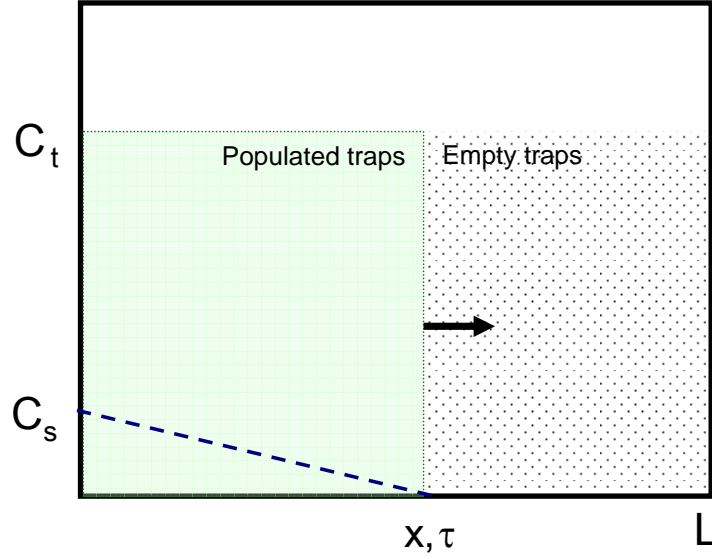
Figure 2.3: Schematic picture of the hydrogen concentration in the presence of traps. C_t is the H concentration in traps populated by the moving H front (green), and C_s denotes the concentration of H in solution (blue dashed line).

the back side of the wall and split it into D_f and D_b, where f and b denote the front and the back surface, respectively. They also introduced one additional parameter:

$$V = \frac{D_b}{L k_b} \sqrt{\frac{k_f}{J_{IN}}} \tag{2.13}$$

With this parameter, one can obtain conditions for the fourth regime:

4) *dr-regime*: $W > 1$ and $V/W > 1$ (i.e., $C_f \approx 0$ and $C_p \approx C_b$)—the front surface is diffusion-limited and the back surface recombination-limited.

Since no metal has a perfect lattice structure, H atoms not only occupy interstitial sites but can also be trapped in lattice imperfections or radiation-induced defects like grain boundaries, dislocations, vacancies, voids etc. Generally, these traps can be characterized by their density ρ_{tr} and the trapping energy E_T which is the energy that needs to be delivered to the H atom for it to be able to leave the trap. Basically, traps can be divided into saturable traps – which have a finite capacity for storing H – and unsaturable traps like bubbles which hold varying amounts of hydrogen, depending on its

pressure. To account for this effect, a trapping term should be added to Fick's law:

$$\frac{\partial C_\text{s}}{\partial t} = D\frac{\partial^2 C_\text{s}}{\partial x^2} + G(x,t) - \frac{\partial C_\text{t}}{\partial t} \tag{2.14}$$

Here, C_s and C_t denote the solute and trapping concentration, respectively (see Fig. 2.3). Since it is a rather difficult task to solve the above equation, one can apply a simplified diffusion-limited model [25] which assumes that if the ion mean range $R_\text{p} \ll L$ is much smaller than the wall thickness, $J_\text{IN} \approx J_\text{f}$, and the permeated flux is neglected. Then the entire situation can be interpreted as the D front moving inside the material with a velocity of [16]:

$$\frac{\mathrm{d}x}{\mathrm{d}t} = \frac{\Phi_\text{diff}}{C_\text{t}} \tag{2.15}$$

where Φ_diff is the D diffusive flux to the depth at which traps are populated, which, at depth R_p, equals the incident flux J_IN. Similarly to Eq. (2.3), one can express Φ_diff as:

$$\Phi_\text{diff} = \frac{DC_\text{s}}{x} \tag{2.16}$$

Inserting Eq. (2.16) into Eq. (2.15), one obtains the depth to which traps are populated:

$$x\mathrm{d}x = \frac{DC_\text{s}}{C_\text{t}}\mathrm{d}t \;\Rightarrow\; x = \sqrt{\frac{2tDC_\text{s}}{C_\text{t}}} \tag{2.17}$$

From Fig. 2.3, one can see that the amount Q_ret of D retained in the traps can be written as:

$$Q_\text{ret} = C_\text{t}x = \sqrt{2tDC_\text{s}C_\text{t}} \tag{2.18}$$

2.3   Transport Parameters

Dynamic hydrogen retention is governed mainly by diffusion (D), solubility (S), and recombination (K_r). These fundamental processes are briefly described below. Because of their small size, hydrogen isotopes can occupy interstitial sites (i.e., be in solution) in a metal lattice and diffuse much more quickly and easily than any other type of atom in solids. Tungsten, as a bcc metal, has three octahedral (o) and six tetrahedral (t) interstitial sites (per atom). According to both experimental [27] and theoretical [28] studies, t-sites are energetically more favorable for hydrogen. Each interstitial site can be occupied only by a single hydrogen atom, which implies that H_2 molecules cannot be formed there.

Above room temperature, when both the Debye energy of the host lattice and the vibration energy of the interstitial are much smaller than the thermal energy kT, the
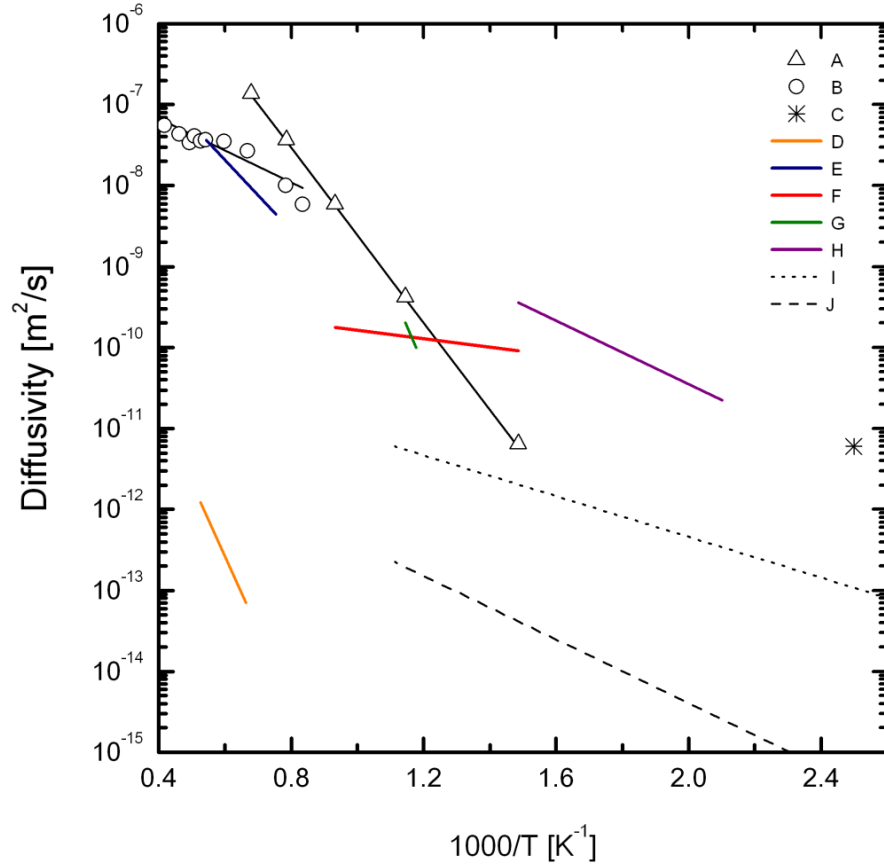
Figure 2.4: Hydrogen and deuterium diffusivities in tungsten measured by (A) Zakharov et al. [29], (B) Frauenfelder [30], (C) Zhetbaev et al. [31], (D) Moore and Unterwald [32], (E) Ryabchikov [33], (F) Esteban et al. [34], (G) Benamati et al. [35], and (H) Otsuka et al. [36]; and modeled by (I) Franzen et al. [37] and (J) Garcia-Rosales et al. [38].

hydrogen isotope can be considered to be a classical particle, and its diffusion can be viewed in the context of the theory of over-barrier jump processes of interstitials via thermal excitation. Then the solute diffusivity – which has the unit of surface area over time – can be expressed as:

$$D = D_0 \exp\left(\frac{-E_A}{kT_{irr}}\right) \tag{2.19}$$

where E_A is the activation energy for diffusion (an energy barrier that must be overcome in order for an atom to move from one equilibrium site in the lattice to the next), k is Boltzmann's constant, T_{irr} is the temperature, and D_0 is the diffusion coefficient which is proportional to the square of the jump distance δ and to the jump frequency ν_H of an hydrogen isotope. Wert and Zener [39] determined that ν_H is inversely proportional to the square root of the mass m_H of the hydrogen isotope. This dependence is found to hold for bcc metals, unlike for fcc metals [40]. On the other hand, the experimentally measured diffusivities shown in Fig. 2.4 have uncertainties higher than $\sqrt{3}$.

There have been many attempts to measure the diffusivity of hydrogen isotopes in tungsten. The scatter of the obtained data (see Fig. 2.4) shows how difficult it is to determine this parameter. Most commonly, Frauenfelder's [30] result of $D = 4.1 \times 10^{-7} \exp(-0.39\,\text{eV}/kT)\,\text{m}^2/\text{s}$ is used. He measured the outgassing rate of hydrogen in sintered, rolled tungsten (99.95% purity) at a very high temperature range of $1200 - 2400\,\text{K}$, thus avoiding the effect of trapping, and determined the interstitial diffusion. The results of Ryabchikov [33], Zhetbaev et al. [31], and Otsuka et al. [36], obtained by other techniques and at other temperatures, are similar to Frauenfelder's. The experimental results obtained by Frauenfelder are also in good agreement with a first-principle study of H diffusion in tungsten [28]. The activation energy calculated for the optimal (t-t) diffusion path was estimated to be $0.2\,\text{eV}$, and for the t-o-t path as $0.38\,\text{eV}$.

Solubility (S with $[S] = 1\,\text{mol}/(\text{m}^3\text{atm}^{1/2})$)) is a measure of the amount of H which can be dissolved interstitially at a particular exposure pressure and can be written as [41]:

$$S = S_0 p^{1/2} \exp\left(\frac{-E_S}{kT}\right) \tag{2.20}$$

Here, S_0 is the solubility coefficient, p is the exposure pressure, and E_S is the solubility activation energy. From a solubility point of view, materials can be divided into endothermic – where energy must be added to introduce H into a solution – and exothermic (with the opposite behavior). Materials with a low solubility are likely to have blisters appearing on their surface. The database for solubility is very scarce. Direct measurements were performed by Frauenfelder [30], Mazayev et al. [42], and Benamati et al. [35].

Indirectly, by using the relation $P = SD$, the solubility can be obtained from the permeability (P) and diffusion results from Zakharov et al. [43]. The solubility measured by Frauenfelder is most commonly in use: $S = 9 \times 10^{-3} \exp(-1.04\,\mathrm{eV}/kT)\,\mathrm{mol}/(\mathrm{m^3 atm^{1/2}})$. Release of atomic gas through the surface is called recombination, and its rate can be written as (see Eq. (2.3)):

$$J_\mathrm{r} = K_\mathrm{r} C_\mathrm{s}(0)^2 \tag{2.21}$$

where K_r is the recombination rate coefficient and $C_\mathrm{s}(0)$ is the gas concentration just below the surface. The K_r values obtained in experiments by Anderl et al. [44] and by modeling [37, 38] are very scattered and inconsistent. Anderl et al. [44] reported a value of $K_\mathrm{r} = 3.2 \times 10^{-15} \exp(-1.04\,\mathrm{eV}/kT)\,\mathrm{m^4/s}$ which was measured on powder metallurgy W (99.95% purity) using permeation techniques over a temperature range of $690 - 825\,\mathrm{K}$.

2.4 Deuterium Retention in Tungsten

Research regarding D retention in polycrystalline tungsten (PCW) and single crystal tungsten (SCW) has already been conducted over three decades and was studied as a function of the incident fluence, flux, energy, exposure temperature, type of material, and impurity presence. The main result of these investigations is that due to the low number of intrinsic defects in W at a level $\sim 5 \times 10^{-4}\,\mathrm{at.\%}$ [45], there should be no concerns about tritium retention in undamaged W. Retained D can be held in the material in both atomic and molecular form [22, 46, 47]. The presence of D_2 is confined to the implanted zone, and the number of retained molecules increases nonlinearly with the incident fluence, approaching saturation at around $10^{23}\,\mathrm{D/m^2}$ at RT. Above an irradiation temperature of $T_\mathrm{irr} = 650\,\mathrm{K}$, deuterium can be accumulated only in atomic form. Atomic D was observed to be present in the implanted zone as well as in the bulk, and, depending on the material, its retention increases with the incident fluence as $\Phi^{0.5-0.7}$ [46, 48]. The D retention dependence on the incident fluence has been studied in PCW and SCW by Ogorodnikova et al. [48, 49], Poon et al. [50, 51], Haasz et al. [52], and Alimov and Scherzer [53]. Although the retention data is scattered over roughly one order of magnitude, it seems that at RT in both types of material, saturation is reached at an incident fluence of around $10^{24}\,\mathrm{D/m^2}$. Here, it is to be noted that the total D retention is lower in SCW due to the smaller number of intrinsic defects. Generally, the retained amount at RT at the saturation point ranges from 0.5×10^{21} to $5 \times 10^{21}\,\mathrm{D/m^2}$ which is rather low. Since the reflection coefficient for $200\,\mathrm{eV/D}$ in W is $r = 0.56$ and the total D retention is much less than half the incident fluence, most of it must be

re-emitted from the sample during irradiation. At $500\,\text{K}$, no saturation was observed up to incident fluences of $1 \times 10^{25}\,\text{D/m}^2$ [48–50, 52].

Haasz et al. [52] reported that by increasing the incident energy, the saturation starting point is shifted toward higher fluences, but this does not lead to a reduction of the retained amount. Later, Ogorodnikova et al. [49] noticed that at low fluences (up to $1 \times 10^{24}\,\text{D/m}^2$) the retention is higher at higher incident energies, while at high fluences this behavior is reversed. Here, higher energies are understood to be energies above the threshold for displacement which for D is $940\,\text{eV}$. Therefore, the higher D retention at higher energies can be explained by the presence of ion-induced defects which serve as additional traps for D. Although low-energy irradiation cannot introduce vacancies in the material, it is impossible to model TDS spectra assuming a presence of only natural defects in the sample [49]. Thus, some other high-energy traps must be produced during D irradiation. The likely responsible mechanism is that due to a low D solubility in W, supersaturation of D_2 occurs in the implanted zone which results in high tension and stress fields. This leads to the displacement of the neighboring atoms and to D bubble creation and, furthermore, can be a cause for dislocation loop formation [22, 49, 54].

Research on the influence of the exposure temperature on D retention was published in Refs. [48–50, 55, 56]. Haasz et al. [52] investigated 25 and $250\,\mu\text{m}$ re-crystallized PCW foils irradiated with 500 and $1000\,\text{eV}$ deuterium ions at $\Phi = 1 \times 10^{24}\,\text{D/m}^2$ and observed a maximum retention of $7 \times 10^{20}\,\text{D/m}^2$ at $450\,\text{K}$ for the lower energy and $2 \times 10^{21}\,\text{D/m}^2$ at $500\,\text{K}$ for the higher energy. This is in contradiction with the results of Ogorodnikova et al. [48, 49] who also irradiated re-crystallized PCW with $500\,\text{eV}$ D ions at $\Phi = 1 \times 10^{23}\,\text{D/m}^2$ and found that with increasing temperature, the D retention was increasing. The same tendency was seen by Poon et al. [50] in two kinds of SCW irradiated with $500\,\text{eV}$ D ions at $\Phi = 1 \times 10^{24}\,\text{D/m}^2$ in the temperature range of $300 - 700\,\text{K}$. Ogorodnikova et al. [49] concluded that at low fluences up to around $1 \times 10^{24}\,\text{D/m}^2$, the D retention drops with the increase of the temperature, while at higher fluences, the retention displays a parabolic dependence on the temperature with the maximum at around $450 - 500\,\text{K}$. This was confirmed by Alimov et al. [55] who measured a value of $1 \times 10^{22}\,\text{D/m}^2$ on re-crystallized W exposed to a $38\,\text{eV}$ D plasma to a very high fluence of $1 \times 10^{27}\,\text{D/m}^2$.

Impurities originating from the bulk or the irradiation gas phase can influence D retention. Poon et al. [50] compared retention between the SCW manufactured by the State Institute of Rare Metals, Moscow – with a high purity of $99.9\,\text{at.\%}$ – and SCW delivered by Johnson Matthey with a ten times larger amount of oxygen (O) and carbon (C). All samples were irradiated with $500\,\text{eV}$ D ions at either 300 or $500\,\text{K}$ and various

fluences. The results revealed that after D irradiation, the number of impurities and their diffusion from the surface into the bulk was enhanced. The presence of impurities significantly influenced D retention which was much higher in the lower purity SCW.

2.5 Blistering in Tungsten

Generally, blisters are pictured as hemispherical structures which appear on the surface and have a lenticular cavity underneath [57, 58]. The thickness of the blister lid increases with increasing ion energy and is called deckeldicke. At low ion energies, the deckeldicke is larger than the mean implantation range of ions, whereas this effect is becoming less pronounced at higher energies. In order for a blister to grow, the nucleation of hydrogen bubbles has to take place first. Impurities, vacancies, or low energy traps such as grain boundaries can serve as nucleation sites [59]. Essentially, a bubble can grow via plastic deformation, loop punching, or vacancy agglomeration into a void. For the first two mechanisms, a high hydrogen fugacity is required. Additionally, as observed by Matsui et al. [60] and Sakamoto et al. [61, 62] who used TEM for dislocation loop investigations, the incident energy of hydrogen must lie above the threshold energy for displacement in tungsten in order for loop punching to occur. Matsui et al. [60] observed interstitial-type loop punching in W irradiated with $10\,\mathrm{keV/D}$ at RT at a low-flux of $6\times10^{18}\,\mathrm{D/(m^2s)}$ and different fluences. From their measurements, they concluded that self-interstitial atom (SIA)-D complexes are formed and act as the nuclei of dislocation loops. Sakamoto et al. [61] investigated dislocation loop formation as a function of the hydrogen incident energy and the irradiation temperature. They noticed that a minimum energy of $4\,\mathrm{keV}$ per H was necessary for the formation of interstitial-type dislocation loops, which means that during hydrogen irradiation, radiation defects were introduced in the material and later served as nucleation sites for loop punching. For the third mechanism to occur, vacancy supersaturation is required. In that case, this mechanism is dominant over loop punching [58]. Additionally, the presence of hydrogen increases the chance of vacancy clustering due to its combining with vacancies into H_xV complexes and lowering the free energy of such a system.

There are two main models which explain blister formation. One of them is the gas-driven model [63, 64] which is able to explain the spherical shape of the blister and the deckeldicke thickness which is larger than the mean range of the incident ions. At low irradiation temperatures, when the vacancies are immobile and their collection cannot take place, highly overpressurized bubbles are formed via, e.g., loop punching, and the final blister formation is caused by the coalescence of these bubbles via, e.g., the

inter-bubble fracture mechanism [63].

The lateral-stress model [65, 66], on the other hand, is based on the discovery that the blister thickness is appreciably larger than the depth of the incident ion peak, especially for low-energy ions. Local bubble swelling leads to an expansion in the direction normal to the implanted layer, introducing compressive stress parallel to it which results in a surface buckle when the stress is too high. This model, however, cannot explain, among other things, the spherical shell shape, and is considered by Evans [64] to play a secondary role in blister formation. Notwithstandingly, this model is able to explain the blistering which appears after low-energy ($< 1\,\mathrm{keV}$) D irradiation [67–71] where – according to Matsui et al. [60] and Sakamoto et al. [61, 62] – loop punching cannot take place and the vacancy abundance is low.

Blister occurrence is favored in materials which are endothermic for hydrogen solution (i.e., with a negative enthalpy of the solution) and which are irradiated at low temperatures (which implies slow diffusion) at high fluxes and fluences. There are many parameters which affect the development of surface structures during hydrogen isotope implantation. Among the most important are the flux and fluence, energy, and temperature of the ion irradiation, the type of implanted material, its roughness, the method of its preparation, and the presence of impurities in the irradiation beam. Depending on the combination of these parameters, different mechanisms of blister formation apply.

In order for blistering to appear, a critical fluence has to be reached. Then, when the fluence increases, the number and size of the blisters also increase until saturation is reached. With time, the number of blisters drops, but they still grow in size. This suggests that small blisters combine into bigger ones either via coalescence or via the inter-bubble fracture mechanism [63]. Further increasing the fluence eventually leads to flaking and exfoliation.

From the perspective of Iter's divertor, the experiments performed at low energies and high fluxes ($> 10^{22}\,\mathrm{D/(m^2 s)}$) and fluences ($> 10^{26}\,\mathrm{D/m^2}$) [59, 69, 72–76] are more important as they reflect realistic conditions. This kind of irradiation typically causes the appearance of not only blisters but also dome-shaped buildings of various sizes. Their occurrence is limited by the grain boundaries, and their size depends on the grain orientation. Under the bigger specimens of those structures, the formation of huge cavities takes place (see Fig. 2.5). According to Shu [72], the vacancy formation mechanism due to a lower vacancy formation energy applies in this case, rather than the one due to plastic deformation. $D_x V$ clusters diffuse to the grain boundaries and agglomerate there, resulting in small blisters.

The critical fluence for blistering, as well as the fluence at which the blisters' size
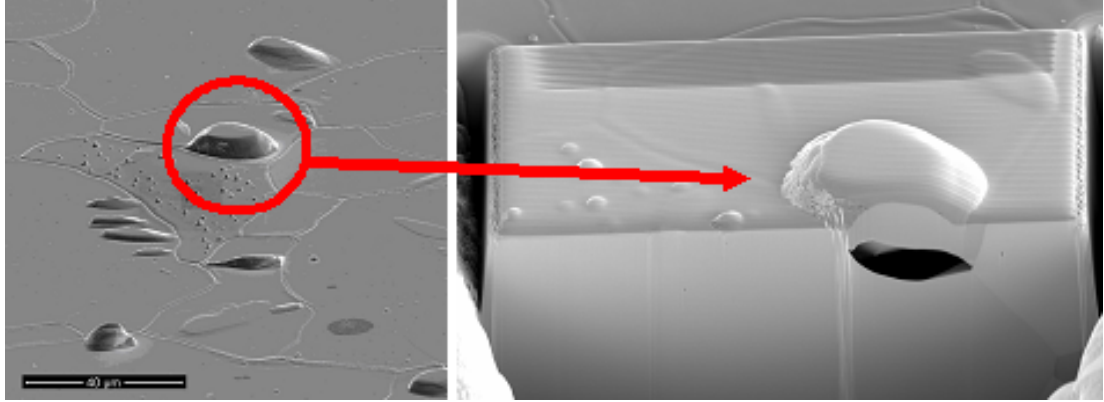
Figure 2.5: SEM micrograph of blisters and a dome-shaped buildings on the surface of re-crystallized tungsten irradiated by a $38\,\mathrm{eV/D}$ plasma to a fluence of $10^{26}\,\mathrm{D/m^2}$ at $T_{\mathrm{irr}} = 505\,\mathrm{K}$ (left), and a cross-section of one of the domes, revealing a huge cavity underneath (right). The pictures were kindly provided by Dr. V.Kh. Alimov.

and number saturate, depends on the incident ion energy [73]. With an increase of energy, a higher fluence is necessary for blisters to appear. This is the case because ions with higher energies are implanted more deeply, and therefore, more hydrogen can be dissolved interstitially. It has also been observed that at the same fluence, irradiation at lower energies results in smaller blisters [68, 71]. As previously mentioned, irradiation at energies below the threshold energy for displacement can also cause blistering [67–71]. The influence of the temperature on blistering has been investigated by many researchers [59, 68, 71, 72, 76], with all results showing the blister size enhancement with increasing temperature [72] up to around $1000\,\mathrm{K}$ where no large blisters were formed [68]. Depending on the material, there is a critical temperature (usually around $500\,\mathrm{K}$) at which the blister size reaches its maximum.

The impact of carbon impurities present in the irradiation beam on the blistering has been studied by Shimada et al. [71, 77], Ueda et al. [78, 79], and Funabiki et al. [80]. They noticed that if the carbon concentration in the beam is kept between 0.15% and around 1%, extensive blistering occurs on the tungsten surface. The reason for that may lie in the formation of a WC layer which prevents H from leaving the tungsten, thus allowing a hydrogen build-up and an increasing internal gas pressure.

Chapter 3

Displacement Damage

As plasma-facing material, W will be subjected to continuous irradiation of $14\,\text{MeV}$ neutrons which are emitted from the fusion plasma. This will cause a modification of the lattice structure resulting in changes of the mechanical (hardening, swelling, and embrittlement) and physical properties. The influence of n-induced damage on tritium retention is of particular concern. In this chapter, the process of displacement damage formation is briefly reviewed.

3.1   Damage Mechanism

When the incident particle strikes the target, it transfers its kinetic energy to the solid, which results in the displacement of lattice atoms along its trajectory. Each directly dislodged atom (by an impinging ion), a so-called primary knock-on atom (PKA), can penetrate the sample, encounter other atoms, and, if its energy T_{PKA} is sufficient, can cause further collisions and form collision cascades. Eventually, the PKA reaches an energy below the displacement energy threshold E_{th}, and no further damage is produced by the PKA. Roughly $10\,\text{ps}$ after the collisional phase, the cooling phase starts during which some of the introduced defects anneal. The number of residual Frenkel pairs which survive and reach the steady state increases with increasing PKA energy [81].

Basically, ion irradiation results in the production of displacement spikes [81–84] which comprise two elementary types of defects: vacancies (V) in the central core of the cascade and interstitial atoms (I) on its periphery. The vacancy core is observed, e.g., by means of field ion microscopy (FIM), to be a depleted zone surrounded by an interstitial mantel and can be considered a source of vacancy clusters (VC). An explanation of the displacement spike formation can be found in the different migration energies of V and I which depend on the crystal orientation. Interstitials are very mobile in W, with the
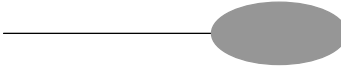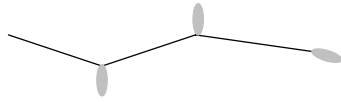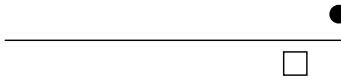
1 MeV neutrons
$\bar{T}_{\mathrm{PKA}} = 35\,\mathrm{keV}$
$\epsilon = 2\%$

1 MeV heavy ions (Ni)
$\bar{T}_{\mathrm{PKA}} = 5\,\mathrm{keV}$
$\epsilon = 4\%$

1 MeV protons
$\bar{T}_{\mathrm{PKA}} = 200\,\mathrm{eV}$
$\epsilon = 25\%$

1 MeV electrons
$\bar{T}_{\mathrm{PKA}} = 60\,\mathrm{eV}$
$\epsilon \approx 100\%$

Table 3.1: Difference in damage morphology after various types of particle irradiation of pure nickel at the same energy. The average PKA energy $\bar{T}_{\mathrm{PKA}}$ and the displacement efficiency ϵ of freely migrating defects is specified for each case [89]. The lines schematically show the path of the incident particles, the ovals illustrate the size of the formed defect clusters, the square denotes V, and the dot represents I.

migration energy $E_{\mathrm{I}}^{\mathrm{m}}$ lying between 0.03 and 0.15 eV [85, 86], whereas vacancies are very slow, with a migration energy $E_{\mathrm{V}}^{\mathrm{m}}$ between 1.4 and 3.3 eV [81, 85–88]. Interstitials can quickly move away from the cascade, while vacancies remain inside. At temperatures far above RT, these point defects can migrate further and thus agglomerate in interstitial clusters (ICs) and VCs, and later even form dislocation loops and voids.

3.2   Simulation of the Effects of Neutron Irradiation

The usage of energetic ion (protons (p), electrons (e$^-$), and heavy ions) irradiation as a surrogate for n irradiation benefits from shorter experiment durations, the production of little or no radioactivity, and lower costs. Each type of ion has its advantages and drawbacks when emulating n irradiation, but it is well-known that the effects of n irradiation cannot be fully simulated by ion irradiation. Tab. 3.1 illustrates the difference in damage morphology after 1 MeV particle irradiation of pure nickel [89].

	neutron	heavy ion	proton	electron
depth of penetration	$\sim$ cm flat profile	nm $-$ μm peaked profile	$\sim$ μm $-$ mm quasi-flat profile	$\sim$ μm
damage morphology	large clusters, dense cascades	large clusters, dense cascades	small clusters, widely spaced cascades	isolated Frenkel pairs no cascades
energy transfer	large	large	small	small
transmutation	yes	no	no	no

Table 3.2: Advantages (green) and disadvantages (red) of irradiation with various particle types with respect to simulating neutron damage.

Neutrons have no electrical charge, therefore they can easily penetrate a material (< 0.1 m) and produce volumetrically distributed atomic displacements [18, 90]. Due to the short range of the nuclear potential in collisions with lattice atoms, collisions with large energy transfer dominate. Transmutation effects always accompany n irradiation and cannot, in any way, be simulated by ion irradiation.

Protons have about the same mass as neutrons, but their electrical charge does not let them penetrate as deeply into a material as neutrons. Nevertheless, they are the best choice for simulating a flat damage profile (at least to some extent) which expands over hundreds of micrometers. The damage morphology is characterized by isolated Frenkel pairs and many widely spaced cascades [91].

Electron irradiation is mostly performed in a transmission electron microscope (TEM). This method limits the achievable energy to ~ 1 MeV and therefore the depth of penetration. On one hand, a very high beam current makes a high fluence possible over a short period, but on the other hand it increases the temperature of the sample. The damage morphology is characterized by widely separated FPs with a low probability for recombination [91].

Because of their high electronic energy loss, the projected range of the heavy ions is the shortest among all aforementioned irradiation particles. For the same reason, the damage profile is strongly peaked, which results in a non-uniform defect distribution. On the positive side, heavy ions reproduce the energy distribution of recoils of neutrons better. They are very efficient in creating dense cascades with large clusters like in

the case of neutrons. Potential chemical composition changes can be avoided by self-implantation. Tab. 3.2 summarizes all important features of ion irradiation with respect to neutrons. Heavy ions seem to be the most suitable choice to simulate the damage morphology caused by fusion neutrons.

3.3 Dpa Simulations

Kinchin and Pease [92] were the first to estimate the displacements per atom (dpa) caused by PKA. Their idea was later modified by the Norgett, Robinson, and Torrens model (NRT) [93] which is based on the Binary Collision Approximation (BCA). The NRT standard takes into account atomic displacements generated by elastic collisions and, by application of Lindhard's theory [94], also by inelastic ones, which is very important since high neutron energies employed in fusion reactors will cause many such displacements. According to this model [93], the number of created Frenkel pairs is given by:

$$N_{\mathrm{d}} = \underbrace{\frac{1}{1 + k\,g(\varepsilon)}}_{\text{inelastic}} \cdot \underbrace{\frac{\kappa T_{\mathrm{PKA}}}{2E_{\mathrm{th}}}}_{\text{elastic}} \tag{3.1}$$

where T_{PKA} is the PKA energy and κ is the displacement efficiency, the latter having a value of 0.8, independently of the PKA energy, the target material, or its temperature. E_{th} is the minimum energy required to eject a target atom from its lattice position. Its value depends on the crystallographic direction of the bombarding particle [88].

$$k = \frac{0.1337 Z_1^{2/3}}{A_1^{1/2}} \tag{3.2}$$

$$g(\varepsilon) = 3.4008\varepsilon^{1/6} + 0.40244\varepsilon^{3/4} + \varepsilon \tag{3.3}$$

$$\varepsilon = \frac{A_2 T}{A_1 + A_2} \frac{a}{Z_1 Z_2 e^2} \tag{3.4}$$

$$a = \left(\frac{9\pi^2}{128}\right)^{1/3} a_0 \left(Z_1^{2/3} + Z_2^{2/3}\right)^{-1/2} \tag{3.5}$$

where a_0 is the Bohr radius, e is the elementary charge, Z_1 and Z_2 are the atomic numbers of the projectile and target, respectively, and A_1 and A_2 are the mass numbers of the two atoms. It is worth to mention that the dpa is not a measure of the amount of defects remaining in the irradiated material. It rather describes how many target atoms could, at most, be ejected from their lattice position. Although the dpa is widely used as a normalization parameter, results obtained by different researchers are sometimes very difficult to compare because they use different values of E_{th}. The results cited

in this thesis are always specified with the dpa normalization that was given by the authors of a particular reference and are not normalized to the same dpa. If available, E_{th} is provided.

In this thesis, the publicly available code Stopping and Range of Ions in Matter (SRIM) [20], version 2008.03, was used to simulate the displacement damage. It is a Monte Carlo based, BCA code. All calculations were performed according to the NRT standard [95] by using the "Detailed calculation with full damaged cascades" option. As input, the types, energies, and angles of incidence of the projectile, as well as the density, thickness, and displacement energy of the target atoms were provided. For W, a minimum displacement threshold energy $E_{\mathrm{th}} = 68\,\mathrm{eV}$ was used [88]—SRIM's E_{th} default value of $25\,\mathrm{eV}$ is unrealistic and far below the measured minimum. The maximum damage concentration was calculated according to the formula:

$$\mathrm{dpa}_{\mathrm{peak}} = \frac{N_{\mathrm{d}}\Phi_i}{N_{\mathrm{W}}} \tag{3.6}$$

The number of displacements ($N_{\mathrm{d}}\,[10^7/(\mathrm{ion}\cdot\mathrm{m})]$) was taken from SRIM. Φ_i denotes the implantation fluence, where i corresponds to either C or W ions, and $N_{\mathrm{W}}\,[\mathrm{at/m^3}]$ is the W atomic density. Using the above formula, the dpa values were calculated under the assumption that Frenkel pairs are not annihilated (simulation at $0\,\mathrm{K}$) and vacancies and interstitials did not diffuse. These effects are not included in the program, and the actual damage structure will be far more complex than the calculated one.

3.4 Defects in W and Their Recovery

The general properties of particle irradiation were given in Sec. 3.2. In this section, the results of defect observation are summarized for W irradiated above RT with different types of particles. Direct and indirect investigations of defect presence and recovery in damaged W were performed using such experimental techniques such as FIM, isochronal resistivity measurements (IRM), positron annihilation (PA), and thermal desorption spectroscopy (TDS), among others. The results are very scattered and sometimes even contradicting, mostly where vacancy cluster and void observations are concerned.

Interstitials, vacancies, and vacancy clusters were observed in n-irradiated W ($E_{\mathrm{n}} > 1\,\mathrm{MeV}$, $T_{\mathrm{irr}} < 370\,\mathrm{K}$) using FIM [96–98]. No voids were seen. Additionally, in these studies as well as in IRM [87, 96–99], the recovery of n-induced defects was reported, mainly at $\approx 0.15\,T_{\mathrm{m}}$ and $\approx 0.31\,T_{\mathrm{m}}$, where T_{m} is the W melting temperature. The point with $\approx 0.15\,T_{\mathrm{m}}$ is called Stage III and is attributed to interstitial annihilation at immobile vacancies. Stage IV at $\approx 0.31\,T_{\mathrm{m}}$ is attributed to vacancy and vacancy cluster

recovery. According to the aforementioned studies, the full defect removal takes place at around 1350 K. Voids ($\varnothing$ 2.6 nm) with low density and big loops ($\varnothing$ 15.8 nm) with high density were seen in W damaged by fast neutrons (0.15 dpa, 870 K) utilizing TEM [100]. Using the same technique, big voids ($\varnothing$ 3.6 nm) with high density and small loops ($\varnothing$ 7.6 nm) with low density were observed in p-irradiated W (1 MeV, 0.15 dpa, T_{irr} = 770 K) [100]. Big voids ($\varnothing$ 12 nm) were also observed by FIM in 800 MeV p-irradiated W (0.13 dpa, RT) [84]. Molecular dynamics (MD) simulations of p-irradiated W confirm the formation of voids ($\varnothing \approx 1.5$ nm containing ≈ 25 vacancies) and defect recovery observed with FIM in n-damaged material. Full defect recovery was reported by Oliver et al. [11] after annealing p-irradiated samples (800 MeV, T_{irr} = 310−440 K, up to 8 dpa) at 1273 K for 6 h. In contrast to the aforementioned findings, this indicates an absence of voids in the damaged W as it is impossible to anneal out voids at this temperature. Positron lifetime and Doppler broadening measurements of W irradiated by 32 MeV α particles [101, 102] show that above 670 K, vacancy migration and VC formation take place. At around 820 K, vacancy loops and microvoids ($\sim$ 10 monovacancies) are formed. Further heating starts up the defect annealing ($\sim$ 1000 K), but even a temperature of 1320 K is not sufficient to complete the process of damage recovery. Other PA studies [103] on heavily damaged W (2 and 20 dpa by 80 MeV ^{12}C and 85 MeV ^{19}F, RT) reported an increase of the free positron annihilation lifetime from $\tau_1 = 105$ ps for undamaged W to 136 ps and 178.4 ps for 2 and 20 dpa, respectively. This increase in lifetime can be attributed to mono- and di-vacancy production (2 dpa), as well as the additional generation of tri- and quadric-vacancies (20 dpa). The increase of the long lifetime component from 2 to 20 dpa was from $\tau_2 = 372.6$ ps to $\tau_2 = 424.1$ ps. The authors suggest that such a long positron lifetime comes from VCs (2 dpa) and from large-size voids (20 dpa). But in light of studies by Troev et al. [104], the lifetimes obtained above can be assigned to VCs composed of at most around 20 vacancies. Many vacancy clusters ($\varnothing < 1$ nm) were observed using FIM in self-implanted W (up to 5.5 dpa, 50 keV, RT) [83]. A decrease of the number of vacancies with increasing irradiation fluence was observed. This is explained by a coalescence of depleted zones originating from different cascades.

Based on the experimental results and computer simulations, one can conclude that ion irradiation leads to vacancy, interstitial, and VC formation. The formation of voids depends on the energy of the bombarding particles, the damage level, and the irradiation temperature, and may not always be possible. The recovery process described by all these methods is similar and in good agreement with the migration energies of V and I. If voids are present, the full recovery temperature is shifted to higher values.

Chapter 4

Experimental Facilities

4.1   Tandem Accelerator

Carbon and tungsten implantations were performed on a 3 MV tandem accelerator
(HVEE) located in the material research division at the IPP Garching. This accelerator
has a dual source injector system (see Fig. 4.1) with an RF ion source model 173 and
a cesium sputter ion source model 860 [105, 106]. The latter was used for heavy ion
irradiation.

The negative ions are delivered by sputtering a suitable cathode with cesium ions and
then are pre-accelerated by a voltage of 36 kV and guided into the low-energy accel-
eration tube (C region) where they are accelerated by a voltage U_a. In the next step,
the beam enters the high voltage terminal (D region) which is located in the center of
the pressure vessel. There, electrons are stripped from the ions by a N_2 gas stripper,
producing a positively charged beam. If the negative beam contains molecules, they
are fragmented here. Finally, the positively charged ions are accelerated by the voltage
U_a in the high-energy acceleration tube (E region) and, by using a switching magnet
(G), the ions with the desired charge (X^{Q+}) are deflected to the correct beam line. The
method of calculating U_a for X^{Q+} ions obtained from an XY cathode is shown below.

- Low energy acceleration tube—acceleration of the negative molecule obtained by
  sputtering the XY cathode:

$$E_{XY^-} = e(U_a + 36) \tag{4.1}$$

$$\frac{1}{2}m_X v^2 + \frac{1}{2}m_Y v^2 = e(U_a + 36) \tag{4.2}$$
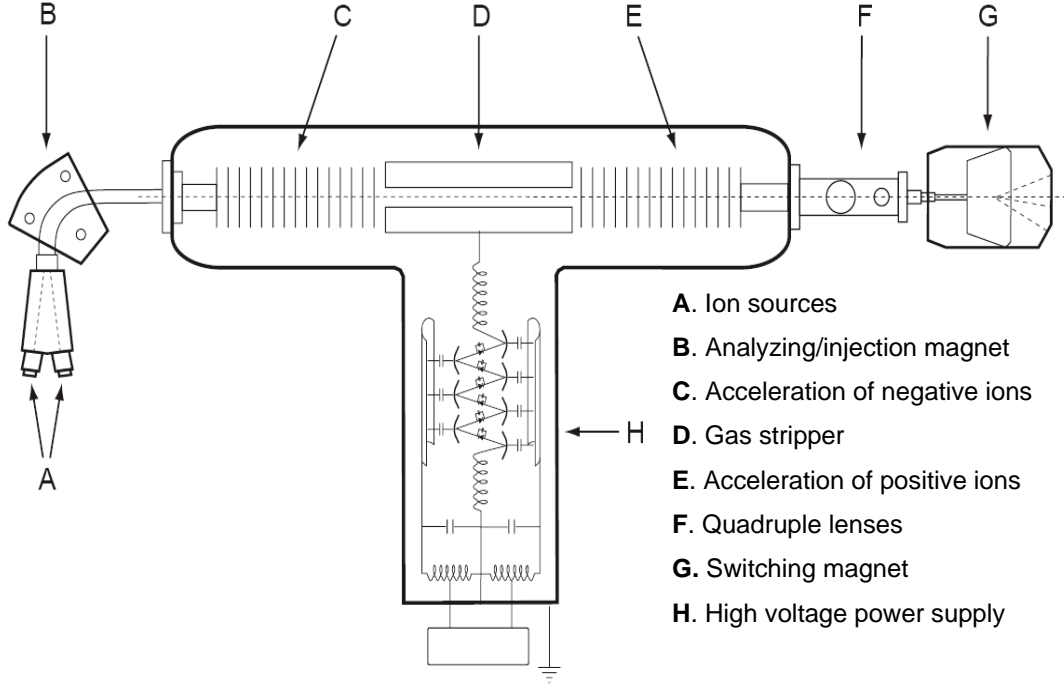
$$v^2 = \frac{2e(U_a + 36)}{m_X + m_Y} \tag{4.3}$$

Figure 4.1: Scheme of the 3 MV tandem accelerator. Source: [105]

$$E_{X^-} \quad = \quad \frac{e(U_a + 36)m_X}{m_X + m_Y} \tag{4.4}$$

- High energy acceleration tube—acceleration of the positive molecule, used for the implantation ions X^{Q+}:

$$E_{X^{Q+}} \quad = \quad E_{X^-} + eQU_a = \frac{e(U_a + 36)m_X}{m_X + m_Y} + eQU_a \tag{4.5}$$

$$U_a \quad = \quad \frac{E_{X^{Q+}}(m_X + m_Y) - 36m_X}{m_X + Q(m_X + m_Y)} \cdot \frac{1}{e} \tag{4.6}$$

Here, E_{XY^-} is the energy of an XY^- molecule (before stripping) in the field free stripper region, E_{X^-} is the energy of an X^- ion (after stripping) in the field free stripper region, U_a is the requested accelerator voltage, m_X and m_Y are the masses of ions X and Y, respectively, $E_{X^{Q+}}$ is the energy of the X^{Q+} ions after passing through the high energy acceleration tube, and Q is the charge of the X ions.

All sample irradiations with heavy ions were performed in the chamber connected to the 3 MV tandem accelerator. The entire beam path from exiting the switching magnet until reaching the sample is shown in Fig. 4.2.
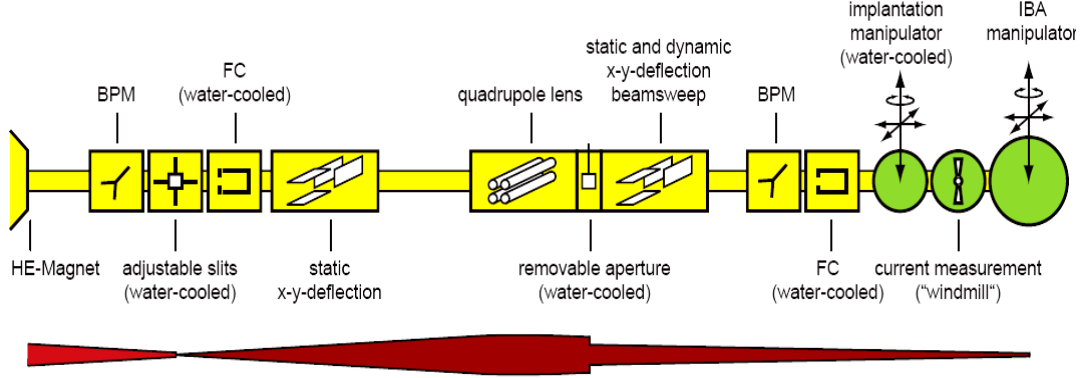
Figure 4.2: Implantation beam line and beam profile of the tandem accelerator at different stages.

	tungsten	**carbon**
cathode	tungsten carbide	carbon
negative ions	WC^-	C^-
ions used for implantation	$^{184}W^{2+}$	$^{12}C^+$
irradiation energy [keV]	5500	500
requested U_a [V] from Eq. (4.6)	1860	232

Table 4.1: Parameters of the tungsten and carbon implantation. Note that the parameters used to obtain the results in Ch. 7 are different.

The background pressure in the implantation chamber was lower than 1×10^{-5} Pa. In order to obtain a homogeneous fluence distribution over the sample surface, the ion beam was swept vertically and horizontally over the target. Beam position, ion flux, and fluence were controlled by an arrangement of four small-diameter Faraday cups located at the four corners of the sample mask. The implanted fluence Φ_i, where i corresponds to either C or W ions, was calculated according to:

$$\Phi_i \left[\frac{\text{ions}}{\text{m}^2} \right] = \frac{q_{\text{total}}}{eAQ} \tag{4.7}$$

where q_{total} [C] is the total collected charge by the Faraday cups, $e = 1.602 \times 10^{-19}$ C is the elementary charge, A is the total area of all four Faraday cups (either 0.0908 or 0.0707 cm^2), and Q is the charge of the ions which were implanted (1 for carbon and 2 or 6 for tungsten).
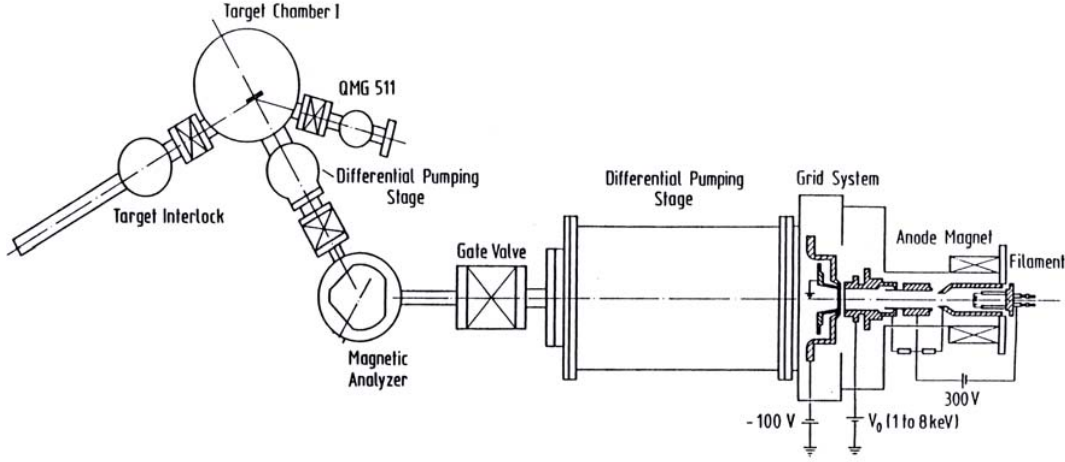
Figure 4.3: HCS experimental setup. The main components are the ion source, differential pumping stages, and a magnet for mass separation. Source: [23]

To check whether the sample/Faraday cup arrangement was working properly, Au ions were implanted into a Si substrate to a fluence of $1.8 \times 10^{20}\,\text{Au}^+/\text{m}^2$, and the thusly prepared sample was analyzed via Rutherford backscattering (RBS). The difference between the Faraday cup value and the value obtained from RBS was within the experimental uncertainties of the RBS measurement. The temperature of the sample was measured by a thermocouple attached directly to the target and was kept at around 290 K during the W ion bombardment.

Carbon and tungsten carbide compressed-powder cathodes were used for $^{12}\text{C}^+$ and $^{184}\text{W}^{2+/6+}$ implantations, respectively. These cathodes are convenient to use and easy to sputter, but they do not last as long. The usage of either doubly or six-fold charged tungsten was dictated by the ability of the HE-magnet to deflect the beam. This depends on the charge of the deflected ions, and less current is required to deflect W^{2+} than W^+. The stripping efficiency for W^{2+} ions allows for implantation of the same dose in half the time. All parameters of the performed irradiations are summarized in Tab. 4.1.

4.2   High Current Source

The undamaged (0 dpa) and damaged W samples were subjected to D ion irradiation and D plasma exposure. The irradiation with monoenergetic D ions was performed at the IPP Garching high current source (HCS) in a vacuum chamber connected to a high

current ion source at normal angle of incidence. A schematic of the experimental device is shown in Fig. 4.3.

A 3600 V D_3^+ ion beam was extracted from the Duo Pigatron ion source, magnetically filtered, and decelerated in front of the sample by a positive target bias of 3000 V to achieve an energy of 600 eV, corresponding to 200 eV/D. Before the bombardment, a pressure of $\sim 1 \times 10^{-6}$ Pa was measured in the target chamber, and during irradiation, it increased to $\sim 5 \times 10^{-5}$ Pa. A liquid N_2 cold trap was installed in the target chamber to reduce the hydrocarbon and water partial pressure, thus reducing surface contamination during the D irradiation. The W samples were irradiated at an ion flux of $\sim 4 \times 10^{19}$ D/(m^{2}s) to fluences from 5×10^{23} up to 5×10^{24} D/m^2, depending on the experiment. An aperture of size 3×6 mm^2 was installed in front of the sample, resulting in a ~ 45 mm^2 irradiation spot (measured via NRA). The implantation fluence Φ was calculated according to:

$$\Phi \left[\frac{D}{m^2} \right] = \frac{3q_{\text{total}}}{eA} \tag{4.8}$$

where A [m^2] is the spot size, and the factor of 3 stems from the D_3^+ molecule. During D irradiation, the W samples were heated up to 320 ± 20 K by the ion beam. By electron bombardment from the rear, the irradiation temperature could also be held at 470 ± 20 K. The temperature of irradiation was measured by an infrared pyrometer (TMSR 95/105, Dr. Georg Mauer GmbH) with an accuracy of ± 20 K, mainly due to changes of the tungsten emissivity.

4.3   Linear Plasma Generator

Some of the W samples were not implanted at IPP Garching but were exposed to a plasma beam in the linear plasma generator [107] installed at JAEA, Tokai, Japan. These implantations were kindly performed by Dr. V.Kh. Alimov. To generate the D plasma, D_2 gas was filled into the plasma generation section at a pressure of about 0.8 Pa. That way, a plasma beam highly enriched with species of D_2^+ to over 80% and less than 20% of D^+ was obtained. Bias voltages of -80, -100, and -140 V were applied to the W specimens, resulting in incident energies of 38, 48, and 68 eV/D, respectively, taking into account the plasma potential of about 4 V as measured by a Langmuir probe. The incident deuterium ion flux was fixed at $(1 \pm 0.05) \times 10^{22}$ D/(m^{2}s). The samples were exposed to an ion fluence of either 1×10^{26} D/m^2 (see Ch. 5) or 3×10^{26} D/m^2 (see Ch. 7). The homogeneously implanted spot had a circular shape with a diameter of 8 mm. All samples were heated by the plasma itself, and the exposure temperature was determined by the thermal contact between the sample and the cooled holder. The
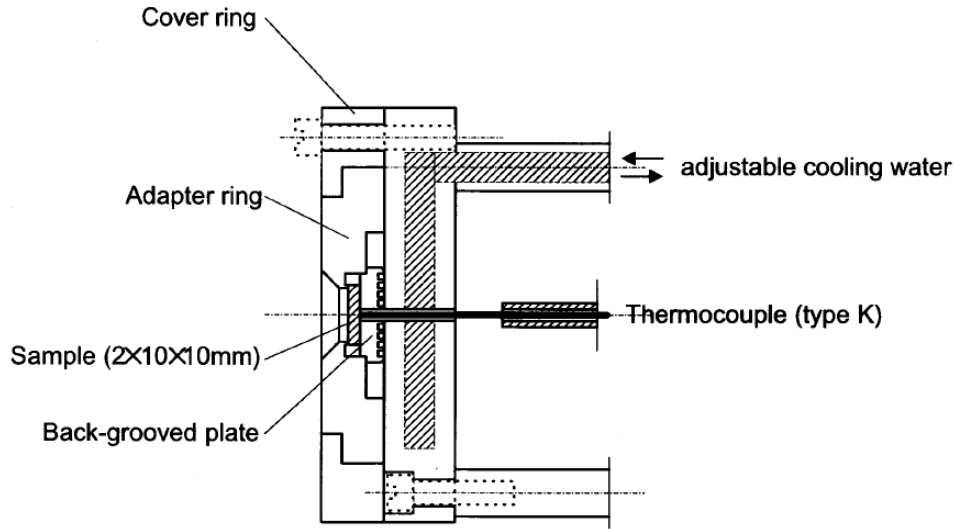
Figure 4.4: Water-cooled Cu sample holder used for D plasma exposure (kindly provided by Dr. V.Kh. Alimov).

resulting sample temperatures during implantation were $350 \pm 20\,\mathrm{K}$ and $470 \pm 20\,\mathrm{K}$ (see Ch. 5) or between 460 and $755\,\mathrm{K}$ (see Ch. 7).

Fig. 4.4 shows the sample holder assembly used during D plasma exposure. Although the specimens were tightly attached to the holder, there was still a possibility of D_2 gas entering the samples from the back side. To study the effect of D_2 gas exposure on D trapping in the damaged layers (see Ch. 7), a self-implanted W specimen was exposed to D_2 gas at a pressure of about $0.8\,\mathrm{Pa}$. For this purpose, the self-implanted W specimen was covered with a pure W foil, and the resulting sandwich configuration was exposed to a D plasma. As a consequence of the exposure device configuration (shown in Fig. 4.4), the self-implanted W specimen was thus only exposed to D_2 gas at $550\,\mathrm{K}$ for $8\,\mathrm{h}\,20\,\mathrm{min}$ (i.e., for the time required to reach an ion fluence of $3 \times 10^{26}\,\mathrm{D/m^2}$). The damaged side of the sample was facing the back side of the sample holder (thermocouple).

4.4   Scanning Electron Microscope and Focused Ion Beam

The surface topography and three dimensional sub-surface morphology of the W samples were examined by a field emission scanning electron microscope (SEM) combined with a focused ion beam (FIB) (HELIOS NanoLab 600, FEI), as shown in Fig. 4.5. The main components of this system are the electron gun (for the SEM), gallium ion column (for
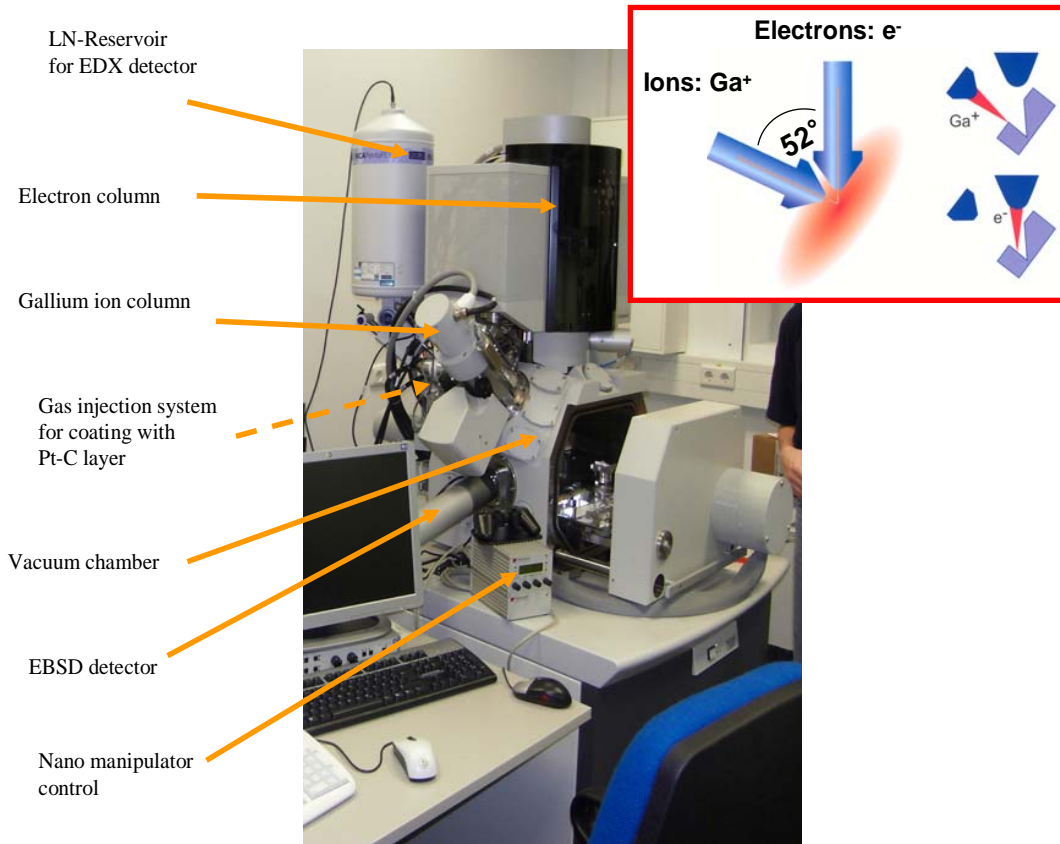
Figure 4.5: Picture of the SEM (Helios, NanoLab 600 FEI) located at IPP Garching. In the insert, the mutual position of the gallium and the electron gun is illustrated schematically (kindly provided by Dr. M. Balden).

the FIB), a secondary electron (SE) detector (Everhard Thornley), and a gas injection system used for coating. High resolution images were created by detecting SEs emitted during e^- or Ga^+ ion interactions with the surface. Images can also be obtained from backscattered e^- and secondary ions (SI) [108].

The FIB system produces a beam of highly energetic Ga^+ ions and focuses them on the sample. A such-prepared beam may be used for deposition, milling, and imaging. The Ga ion beam allowed surface cross-sectioning after selecting a certain, micrometer-sized feature on a material, investigating its surface topography and analyzing its morphology beneath the surface. For cross-sectioning, the surface normal was aligned to the ion beam. Prior to cutting, the investigated surface was coated in situ with a Pt-C film (see Fig. 4.6A). For this purpose, gaseous $C_9H_{16}Pt$ was injected and decomposed by
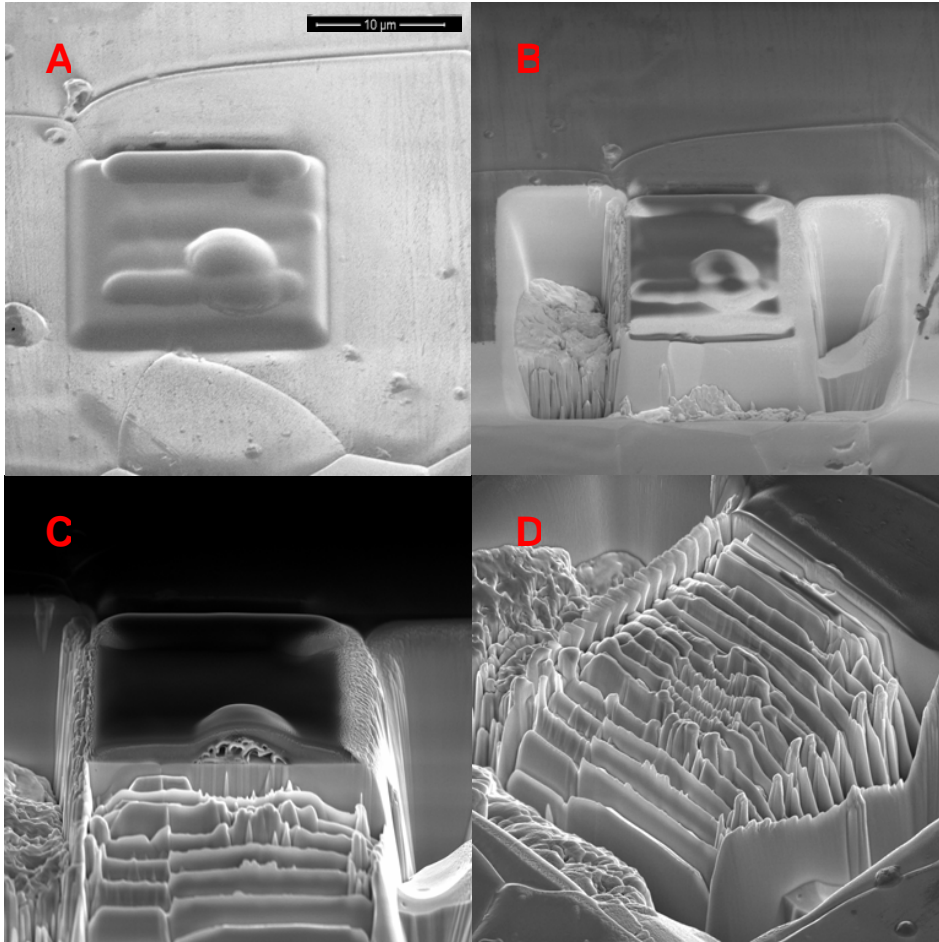
Figure 4.6: Steps required for sample cross-sectioning: (A) deposition of Pt-C on the region of interest; (B) digging a mould around the deposited area; (C) cross-sectioning every $1\,\mu$m; and (D) the final stage when cross-sectioning is finished.
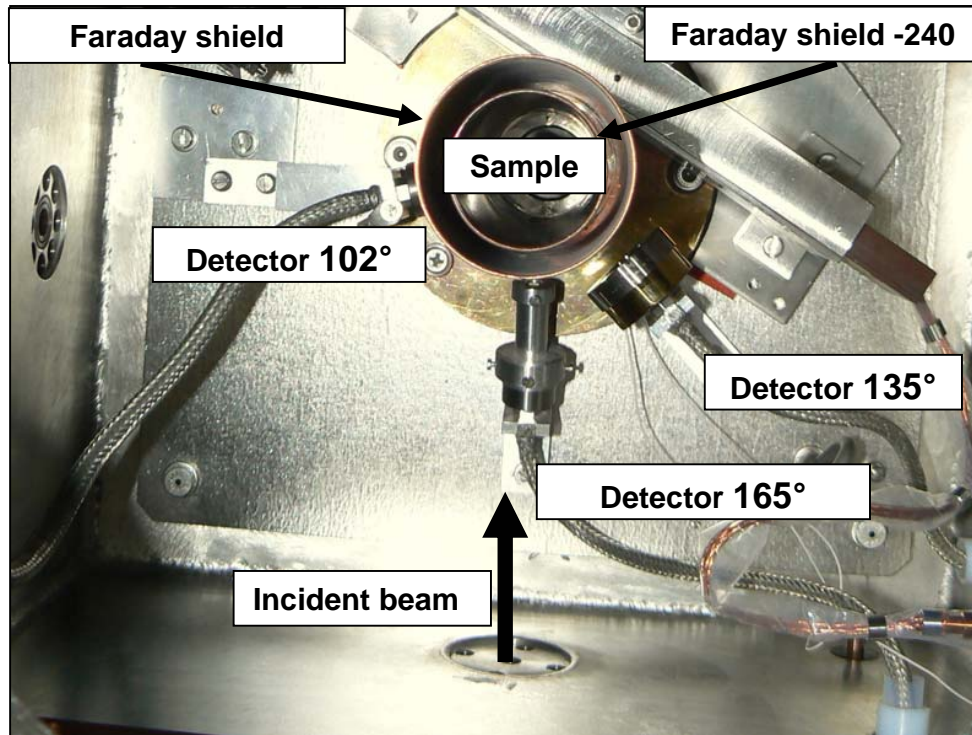
Figure 4.7: Top view of the Ion Beam Analysis (IBA) experimental setup in the RKS chamber (the ERD detector is not included). Source: [109]

the scanning ion beam forming a solid layer on the selected surface. This levels the surface, which reduces artifact creation caused by the cross-sectioning, e.g., striations in the face of a cross-section due to changes in the sputter yield, the so-called curtain effect. Later, the material around the deposited area was dug out (see Fig. 4.6B), and the sample was cut every $1\,\mu$m (see Fig. 4.6C). SEM pictures were taken after each cut.

4.5 Nuclear Reaction Analysis

Nuclear Reaction Analysis (NRA) is a very useful technique which offers a non-destructive compositional analysis of light elements situated in a heavy matrix. RBS is of no use in this case, as the Rutherford cross-section increases with the square root of the atomic number, and therefore the background from the heavy matrix overlaps with the signal from the light element [110]. In NRA, accelerated particles initiate a nuclear reaction with nuclei of a low-Z element present in a film, and then the product particles are detected. The intensity of the emitted radiation is a measure for the concentration

backscattering angle θ [°]	102.0 ± 0.5	135.0 ± 0.5 (proton detector)	165.0 ± 0.5
solid angle [msr]	9.16 ± 0.07	29.94 ± 0.20	1.159 ± 0.01
foils	—	$5\,\mu m$ Ni $12\,\mu m$ Mylar	$10\,\mu m$ Mylar
geometry	IBM	IBM	Cornell
thickness [μm]	700	2000	500
resolution [keV]	11	17	11
other parameters	rectangular slit: width – 1 mm height – 7 mm	parabolic slit: width – 3 mm height – 17 mm distance – 40 mm	—

Table 4.2: Parameters of the detectors located in the RKS chamber. Source: [109]

of the light element. In order to reduce the signal coming from backscattered particles, the installation of an absorption foil in front of used detector and low current measurements are required, which increases the time necessary to obtain good statistics. The high-energy protons are the products of the nuclear reaction. A thick detector should be used to detect them. All NRA measurements were carried out ex situ in the RKS (Rueckstreutopf) chamber in Garching. The latter is a multi-purpose scattering chamber equipped with four detectors (see Fig. 4.7). Parameters for the three of them (without the ERD detector) which were used for experimental spectra simulations, are collected in Tab. 4.2.

4.5.1   Carbon Depth Profiling

There are two main non-resonant nuclear reactions which can be used for carbon depth profiling and quantitative analysis, namely the (d,p) and (^{3}He,p) reactions. In comparison to the (d,p) nuclear reaction, when using ^{3}He as incident particles, one has a smaller cross-section but better depth resolution, which stems from the higher stopping power for ^{3}He than for D, and a significantly lower neutron production. The problem with these two reactions is an inability to distinguish between carbon implantation and carbon surface contamination. This problem can be circumvented by ^{13}C irradiation, but that way, other difficulties appear, e.g.: an impossibility to measure a depth profile due to a very small cross-section.
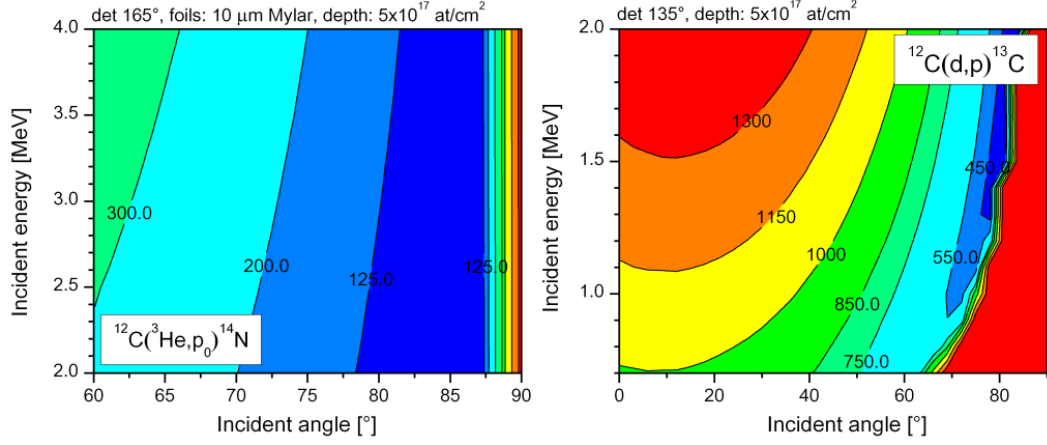
Figure 4.8: Depth resolution (in 10^{15} atoms/cm^2) for the ^{12}C(^{3}He, p$_0$)^{14}N and the ^{12}C(d,p)^{13}C nuclear reactions as a function of the incident energy and angle.

In order to obtain the best depth resolution, the RESOLNRA program [111] was used to find the optimum incident energy and incident angle at a certain depth. The final choice of the incident energy was determined by the maxima in the cross-section of that specific reaction. Fig. 4.8 shows the results of the respective calculations performed for carbon implanted tungsten in a depth of 5×10^{17} atoms/cm^2 for the ^{12}C(^{3}He, p$_0$)^{14}N ($Q = 4.78$ MeV) reaction at a scattering angle of 165° and for the ^{12}C(d, p)^{13}C ($Q = 2.72$ MeV) reaction at a scattering angle of 135°.

Protons from the ^{12}C(^{3}He, p$_0$)^{14}N nuclear reaction, with the cross-section measured by Kuan et al. [112], were collected by the silicon surface barrier detector with a backscattering angle $\theta = 165^\circ$. A 10 μm Mylar foil was positioned in front of the detector to absorb elastically scattered ^{3}He ions and reduce the pile-up. Based on the depth resolution calculations, 3.6 MeV ^{3}He ions at 70° incident angle were used for the measurements. The signal (shown in Fig. 4.9) was converted to a C depth profile using the SIMNRA program [113].

The protons from the ^{12}C(d, p)^{13}C nuclear reaction, with the cross-section measured by Jarjis [114], were counted using a wide-angle (29.94 msr) proton detector placed at a scattering angle of 135°. Due to the low energy of the backscattered deuterium, there was no need to install an absorbing foil in front of this detector, which increased the depth resolution by a factor of two. 1.05 MeV D ions and an incident angle of 60° were chosen for carbon depth profiling. The protons from this reaction were only used to confirm the concentration of carbon measured previously by the ^{12}C(^{3}He, p$_0$)^{14}N reaction.
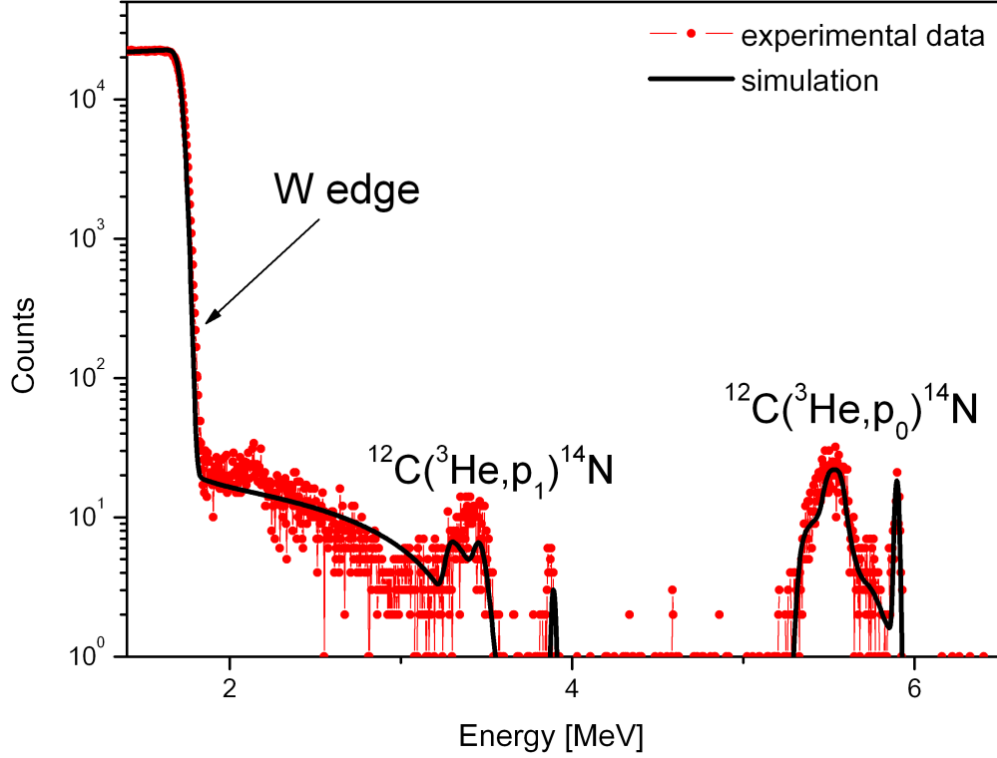
Figure 4.9: NRA spectrum of a tungsten sample implanted by C ions up to a fluence of $\Phi_C = 2.5 \times 10^{17} \, C^+/cm^2$. Protons from the ^{14}N ground and first excited state were detected at $\theta = 165°$.

4.5.2 Deuterium Depth Profiling

$^3He + D \rightarrow p + \alpha$ is a nuclear reaction whose cross-section shows a broad resonance (see Fig. 4.10), allowing deuterium resonant depth profiling and local concentration measurements. For backward scattering angles, this reaction has inverse kinematics, i.e.: the lower the energy of the incident ^3He, the higher the energy of the emerging protons.

The D concentration within the near-surface layer (at depths up to about $0.5 \, \mu m$) was measured by means of the $D(^3He, \alpha)p$ reaction at a ^3He energy of $0.69 \, MeV$. The α particles were energy-analyzed with a small-angle surface barrier detector at a laboratory scattering angle of $102°$. The α spectrum was transformed into a D depth profile using SIMNRA with the depth resolution computed by RESOLNRA as shown in Fig. 4.11.

To determine the D concentration at larger depths, an analyzing beam of ^3He ions (beam spot $\varnothing 1 \, mm$) with energies varied from 0.69 to $4.0 \, MeV$ (in energy steps $>$
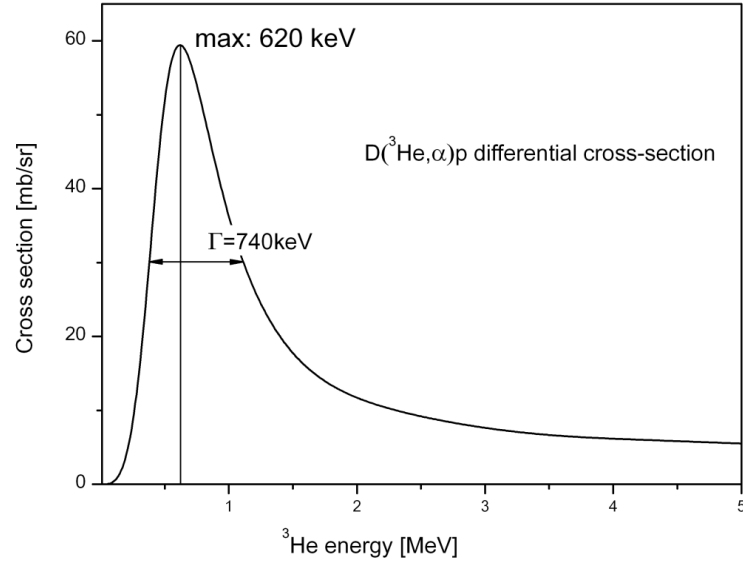
Figure 4.10: D(^{3}He, α)p differential cross-section measured by Alimov et al. [115] with the maximum at 620 keV and the width of the resonance indicated in the graph.
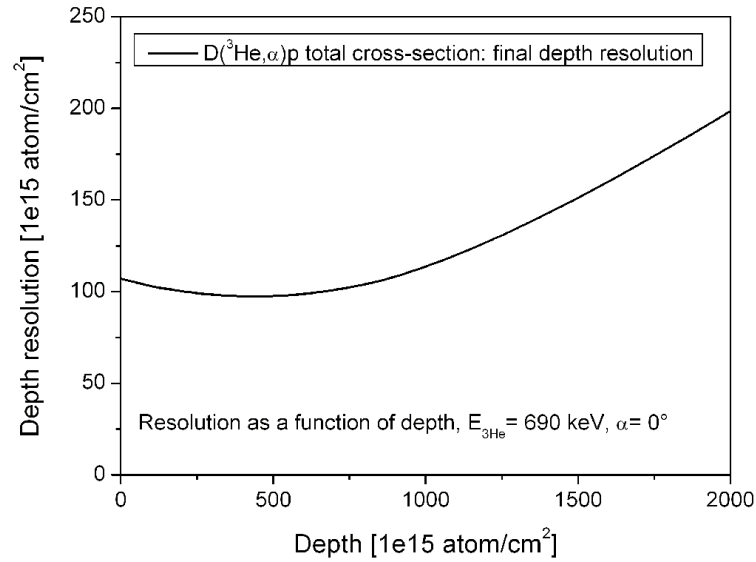

Figure 4.11: Deuterium depth resolution as a function of the depth calculated for ^{3}He with an incident energy of 690 keV and an incident angle of 0°.
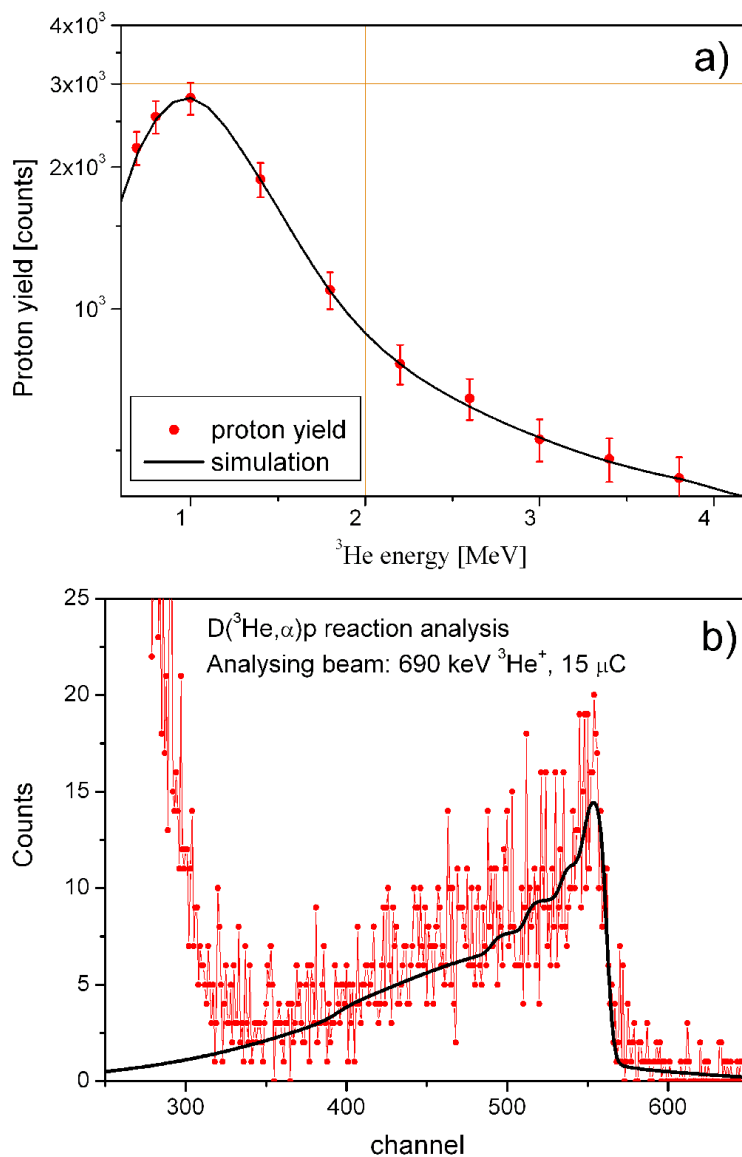
Figure 4.12: Proton yields (a) and a spectrum (b) measured for PCW damaged to the level of $0.4\,\mathrm{dpa}$ and then exposed to a $38\,\mathrm{eV/D}$ plasma at $470\,\mathrm{K}$ to a fluence of $1\times10^{26}\,\mathrm{D/m^2}$. Red dots represent experimental data, black lines are simulations.
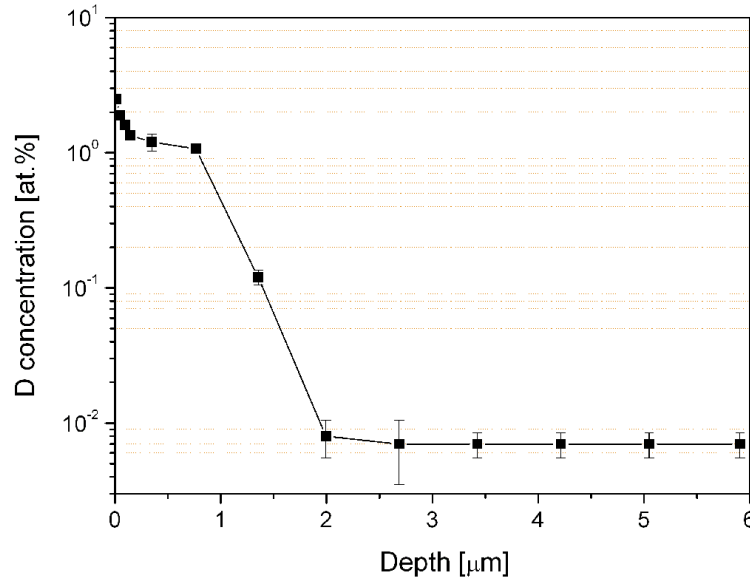
Figure 4.13: Deuterium depth profile in PCW damaged to a level of 0.4 dpa and then exposed to a 38 eV/D plasma at 470 K to a fluence of 1×10^{26} D/m^2. The depth profile was derived from data shown in Fig. 4.12.

$\Gamma/2$, see Fig. 4.10) was used. The protons from the D(^{3}He, p)α nuclear reaction were counted using a wide-angle (29.94 msr) proton detector placed at a scattering angle of 135°. A Ni foil with a thickness of 5 μm and a 12 μm Mylar foil were positioned in front of the detector to absorb elastically scattered ^{3}He ions and α particles from the D(^{3}He, p)α nuclear reaction. In order to extend the analysis of the D concentration to depths of several micrometers, the program NRAUTIL was used for the deconvolution of the proton yields measured at different ^{3}He ion energies (see Fig. 4.12a). NRAUTIL remotely controls SIMNRA via its *ole* interface and uses it to calculate the proton peak counts resulting from a given D depth profile (see Fig. 4.13) for the different ^{3}He ion energies. By iteratively adjusting the input D depth profile, the calculated proton peak integrals can be matched to the experimentally determined profile [115, 116]. The initial input D depth distribution was based on the near-surface depth profile obtained from the α particles (see Fig. 4.12b). Finally, the quality of the obtained depth profile is once more proven by fitting it to all experimentally measured proton peaks (see Fig. 4.14). Since the protons originating from the near-surface deuterium contribute to the protons collected at higher depth (superposition of all contributions), this method is more accurate for flat depth profiles. A major problem of the energy scanning technique is an ion-induced loss of deuterium. This can be seen especially in C-implanted samples,
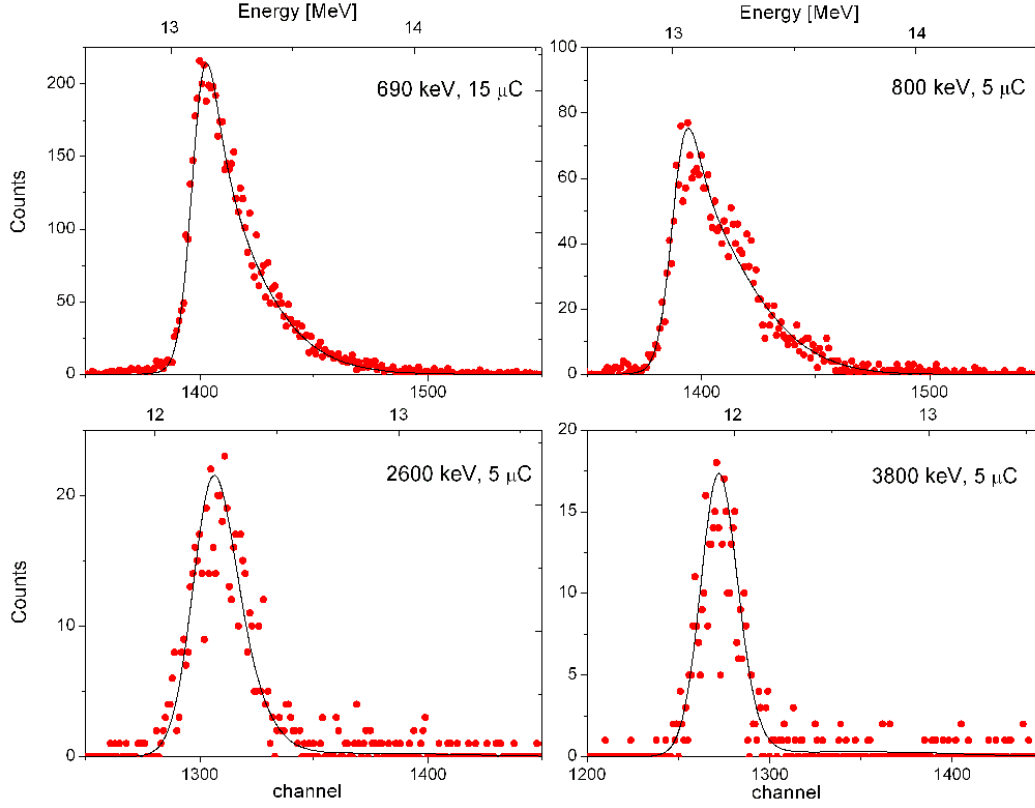
Figure 4.14: Proton energy spectra from the $D(^3He, p)\alpha$ nuclear reaction at four different energies measured for W damaged to the level of 0.4 dpa and then exposed to a 38 eV/D plasma at 470 K to a fluence of 1×10^{26} D/m^2. Red dots denote experimental data, black lines are SIMNRA simulations based on the D depth profile shown in Fig. 4.13.

while the effect is negligible in pure W targets. To account for this, the same spot was measured at 0.69 MeV at the beginning, and again after 1.4, 2.2, and 4.0 MeV. The decrease of D was used to correct the proton yield. The NRA measurements at higher energies reveal the presence of impurities some on the surface like detecting carbon by using the $^{12}C(^3He, p_{0,1,2})^{14}N$ reaction.

4.5.3   Error Bars

The total number of detected protons from the $D(^3He, p)\alpha$ nuclear reaction is given by:

$$Y_p(E_0) = \frac{Q}{\cos\alpha} \int_\Omega d\Omega \int_0^{x(E_0)} C_D(x) \frac{d\sigma(E(E_0, x))}{d\Omega} dx \qquad (4.9)$$

Here, E_0 is the incident energy of the ^{3}He ions, Q is the analyzing beam dose, α is the incident angle, $C_D(x)$ is the deuterium concentration at depth x, $d\sigma(E(E_0, x))/d\Omega$ is the differential cross-section, and Ω is the detector solid angle.

The number of collected protons fluctuates about its mean $Y_p(E_0)$ with a standard deviation $\sigma_k = (Y_p(E_0))^{1/2}$. These fluctuations are due to the Poisson noise of a counting experiment. Therefore, if the proton count statistics are very low, this quantity has the highest contribution to the final error. Further, an additional systematic error of 7% has to be added due to the below-mentioned contributions: (i) the relative accuracy of the employed differential cross-section is $\pm 3.5\%$ [115], (ii) $\pm 3\%$ is the error of the beam current measurements, (iii) the uncertainty of the solid angle of the detector at 135° is ± 0.2 msr (see Tab. 4.2). The uncertainty of the incident angle is $\pm 2°$, which means that it can be neglected.

The calculation of $C_D(x)$ requires the solution of a Fredholm integral equation of first kind. It is a linear equation as long as $C_D(x)$ does not influence the stopping power. The contributions from the integral equation can be approximated by a linear matrix equation $Y = MC$:

$$
\underbrace{\begin{vmatrix} Y_p(E_0^1) \\ Y_p(E_0^2) \\ \vdots \\ Y_p(E_0^j) \end{vmatrix}}_{Y} = \underbrace{\begin{vmatrix} m_{11} & m_{12} & \cdots & m_{1i} \\ m_{21} & m_{22} & \cdots & m_{2i} \\ \vdots & \vdots & \ddots & \vdots \\ m_{j1} & m_{j2} & \cdots & m_{ji} \end{vmatrix}}_{M} \cdot \underbrace{\begin{vmatrix} C_D(x_1) \\ C_D(x_2) \\ \vdots \\ C_D(x_i) \end{vmatrix}}_{C} \tag{4.10}
$$

where m_{ji} is the effective contribution due to the deuterium in the ith layer for the jth energy. Then, the formal solution is given by:

$$
C = M^{-1}Y \tag{4.11}
$$

However, since the measured data Y is distorted by a noise ϵ, the actual computation of C by $M^{-1}(Y + \epsilon)$ leads to unphysical results like negative concentrations due to the bad condition number of M [117]. Several approaches to handle this problem have been put forward in the literature [117–119]—the numerical efforts are considerable for those techniques, however. For this reason, a different approach is chosen here, based on (iterative) forward modeling. Using background information from physics like smoothness, the assumed D depth profiles were fitted to $Y_p(E_0)$ and to $Y_p(E_0) \pm ((Y_p(E_0)^{1/2} + 7\% Y_p(E_0)))$, giving the average D depth profile with its upper and lower error.

4.6   Thermodesorption spectroscopy

If energy is delivered to the substrate by, e.g., increasing the material temperature, then the trapped deuterium can escape the adsorption potential due to the increase of thermal vibrations. Many processes have to happen before the released D can be registered. First it has to dissociate from the trap and then diffuse toward the surface. On its way there, it can be trapped again in defects with higher energies. Lastly, recombination takes place on the surface. During thermodesorption spectroscopy (TDS), the temperature increases linearly, and the partial pressure change is monitored. The latter is proportional to the desorption rate. From the TDS measurements, one can obtain information about the desorption temperatures, the desorption order, and the different desorption states. Desorption at low temperatures corresponds to low-energy traps, and at high temperatures to high-energy traps. Additionally, desorption of gas from the bulk contributes to the high temperature desorption peaks as the gas needs some time to diffuse from the bulk to the surface and then be released.

Two different TDS setups were used. Some TDS measurements were performed at TESS (Thermal Effusion Spectroscopy Setup), located at IPP Garching. The samples were placed in a quartz tube and then heated up to $1100\,\mathrm{K}$ with a ramping rate of $\alpha = 0.5\,\mathrm{K/s}$ by means of infrared radiation. The temperature of the reference W sample was measured multiple times using a thermocouple, and then the sample temperature function versus the (linearly increasing) oven temperature was derived. The temperature of the samples was evaluated using this function. During heating, the HD (mass 3) and D_2 (mass 4) molecules were recorded by a quadruple mass spectrometer (QMS, Pfeiffer DMM 422) which was calibrated using a bottle filled with gas (H_2 or D_2). An average value of H_2 and D_2 sensitivities was accepted for the sensitivity for the HD molecules. The amount of released deuterium was determined by integrating the D_2 and HD QMS signals.

The second TDS was located in a second vacuum chamber connected to the high current ion source at IPP Garching. The temperature of the sample was measured by a K-type thermocouple attached to the target. By means of electron bombardment, the sample was heated up to $1100\,\mathrm{K}$ with a ramping rate of $\alpha = 1.4\,\mathrm{K/s}$. During heating, the HD (mass 3), D_2 (mass 4), HDO (mass 19), and D_2O/CD_4 (mass 20) molecules were recorded by a quadruple mass spectrometer (Pfeiffer QMG700). The QMS signal was not calibrated absolutely.

Chapter 5

Self-Damaged Tungsten

In this chapter, experimental results on D retention in self-implanted tungsten are presented. Due to the large amount of data obtained from the roughly 50 samples (see Tab. 5.1), only a representative selection of the results is shown.

5.1 Samples

The samples were prepared from a polycrystalline W (PCW) plate (99.95 wt.% purity) delivered by Goodfellow Cambridge Limited. The standard impurity analysis gives their concentrations in ppm by weight: Ca < 20, Cu < 20, Fe $\sim$ 20, Mg < 10, Mo $\sim$ 150, Ni < 20, Pb < 50, Si < 50, Sn < 30, Ti < 20, C < 30, H < 6, N < 10, and O < 30. A $500\,\mu$m thick W plate was cut into $10\times10\,\text{mm}^2$ and $12\times15\,\text{mm}^2$ size targets and then mechanically polished to mirror-like finish. Subsequently, the samples were outgassed at $1200\,$K for $2\,$h in vacuum with a background pressure of $2\times10^{-6}\,$Pa. This temperature is high enough to remove any polishing residue as well as decrease the amount of impurities and intrinsic defects.

The W samples were irradiated initially with W ions and then with D ions. Their treatment is shown in Tab. 5.1. The implantation with $5.5\,$MeV W^{2+} ions with a projected range $R_\text{p} \sim 400\,$nm was done at an ion flux of $(0.9 - 9)\times10^{14}\,\text{W}^{2+}/(\text{m}^2\text{s})$ to fluences of 3.5×10^{16}, 3.5×10^{17}, and $1\times10^{18}\,\text{W}^{2+}/\text{m}^2$, which correspond to damage levels of 0.04, 0.4, and 1.2 dpa in the maximum of the damage profile or equivalent neutron fluences of 2.5×10^{23}, 2.5×10^{24}, and $7\times10^{24}\,\text{n}/\text{m}^2$, respectively. The rate of implantation was adjusted to the implanted fluence, resulting in final dpa rates from $1\times10^{-4}\,$dpa/s at the lowest fluence to $1\times10^{-3}\,$dpa/s at the highest fluence which is more than 10^4 times higher than the expectations for Iter. These dpa levels are reached at the maximum of the damage profile and were calculated according to Eq. (3.6). The SRIM calculation

500 μm PCW, mirror-like polish, outgassing 1200 K, 2 h				
STEP 1: 5.5 MeV tungsten self-implantation, RT		0 dpa (undamaged)	0.04 dpa 0.4 dpa 1.2 dpa	
STEP 2: heat treatment		no annealing (batch A) or 1200 K, 2 h (batch B)		
STEP 3: deuterium irradiation	two energies	200 eV/D$^+$ 200 eV/D$^+$ ion irradiation	38 eV/D 38 eV/D plasma exposure	
	two T_{irr}	320 K 470 K	350 K 470 K	
	three fluences	5×10^{23} D$^+$/m^2 3×10^{24} D$^+$/m^2	1×10^{26} D/m^2	

Table 5.1: Sequence of sample preparation. All samples except one (not included in the table) were annealed at 1200 K for 2 h. Some of the damaged samples were annealed twice—before and after self-implantation.

shows that the maximum damage concentration is located at depths of $0.2-0.4\,\mu$m (see Fig. 5.1).

After the W pre-implantation, half of the samples were annealed at 1200 K for 2 h in vacuum at a background pressure of 2×10^{-6} Pa in order to remove radiation-induced defects. The damaged W samples were divided into two batches: the batch labeled A contains damaged W samples without post-implantation annealing, whereas the self-implanted samples annealed at 1200 K for 2 h comprise batch B. Additionally, undamaged W targets were used for comparison. The undamaged (0 dpa) and damaged W samples were subjected to D ion irradiation at the HCS to fluences of 5×10^{23} and 3×10^{24} D/m^2, as well as to D plasma exposure to an ion fluence of 1×10^{26} D/m^2 (see Secs. 4.2 and 4.3). The energy of the D irradiation (38 eV/D for plasma or 200 eV/D for ions) was too low to induce any kinetic atom displacement. The resulting sample temperatures during the implantation were 320/350 and 470 K (see Secs. 4.2 and 4.3). It should be noted that in both implantation setups, the D ion implantation range (several nanometers) was much smaller than the depth of the radiation defects generated by the W ions (several hundred nanometers).
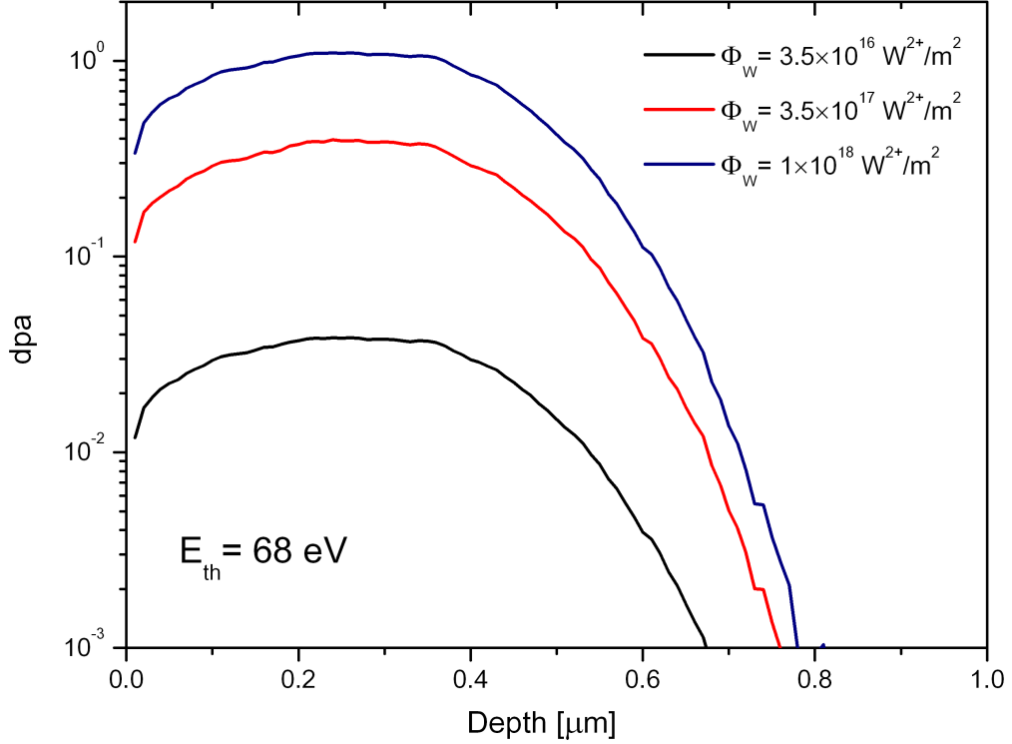
Figure 5.1: Damage distributions in W irradiated with $5.5\,\text{MeV}$ W^{2+} ions to three different damage levels ($E_{\text{th}} = 68\,\text{eV}$).

5.2   Deuterium Depth Profiles

The D inventory and the depth profiles up to $\sim 6\,\mu\text{m}$ were measured ex situ by means of NRA. The effect of D trapping by radiation-induced defects was studied by comparison of D depth profiles measured on damaged and undamaged samples at different irradiation temperatures. Exemplary D depth profiles obtained for W samples exposed to D plasma are shown in Figs. 5.2 and 5.3.

Four different zones can be distinguished in the D depth profiles: (i) the near-surface layer up to $0.2\,\mu\text{m}$, (ii) the damaged zone at $0.2 - 0.7\,\mu\text{m}$, (iii) the sub-surface zone at $0.7 - 1.5\,\mu\text{m}$, and (iv) the bulk. The near-surface layer of all investigated targets is characterized by a sharp increase in concentration which can appear due to sudden structural changes caused by low-energy D irradiation to a fluence above $5\times10^{23}\,\text{D/m}^2$. These changes are, e.g., precipitates [16] or bubbles formed in the stopping zone even by low-energy irradiation [22, 46]. Also, some impurities initially present on the surface may enhance the local concentration.
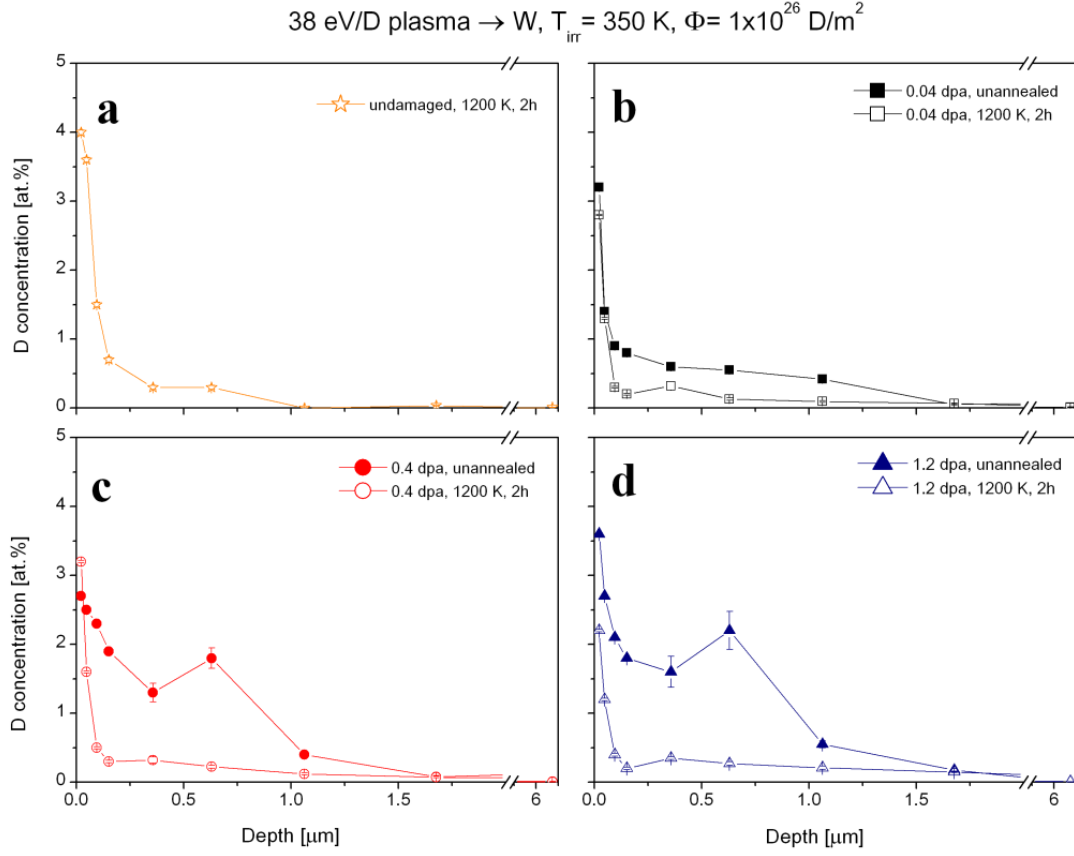
Figure 5.2: Depth profiles of deuterium trapped in PCW, undamaged and pre-damaged with $5.5\,\mathrm{MeV}$ W^{2+} ions to damage levels of 0.04, 0.4, and $1.2\,\mathrm{dpa}$ with and without subsequent annealing at $1200\,\mathrm{K}$ for $2\,\mathrm{h}$, after irradiation with $38\,\mathrm{eV}$ D plasma to a fluence of $1\times10^{26}\,\mathrm{D/m^2}$ at $350\,\mathrm{K}$.

For both irradiation temperatures, the concentration quickly decreases with depth for the undamaged samples. For the damaged W samples (batch A), the D concentration at depths up to $1.5\,\mu\mathrm{m}$ is higher than for the undamaged ones and approaches a plateau at around 0.016 D/W at $0.4\,\mathrm{dpa}$. The higher D retention extending beyond the damaged zone (sub-surface) may be explained by the appearance of stress fields (see Refs. [22, 49], as well as Sec. 2.4) induced by W pre-implantation and/or by exposure to D ions/plasma. In the bulk, the D concentration is at a level of $\sim 5\times10^{-4}\,\mathrm{at.\%}$ and is similar for all samples. This low level of D concentration is a result of D diffusion and trapping in intrinsic defects [45].

Apparently, the radiation-induced defects serve as trap sites for deuterium atoms dif-
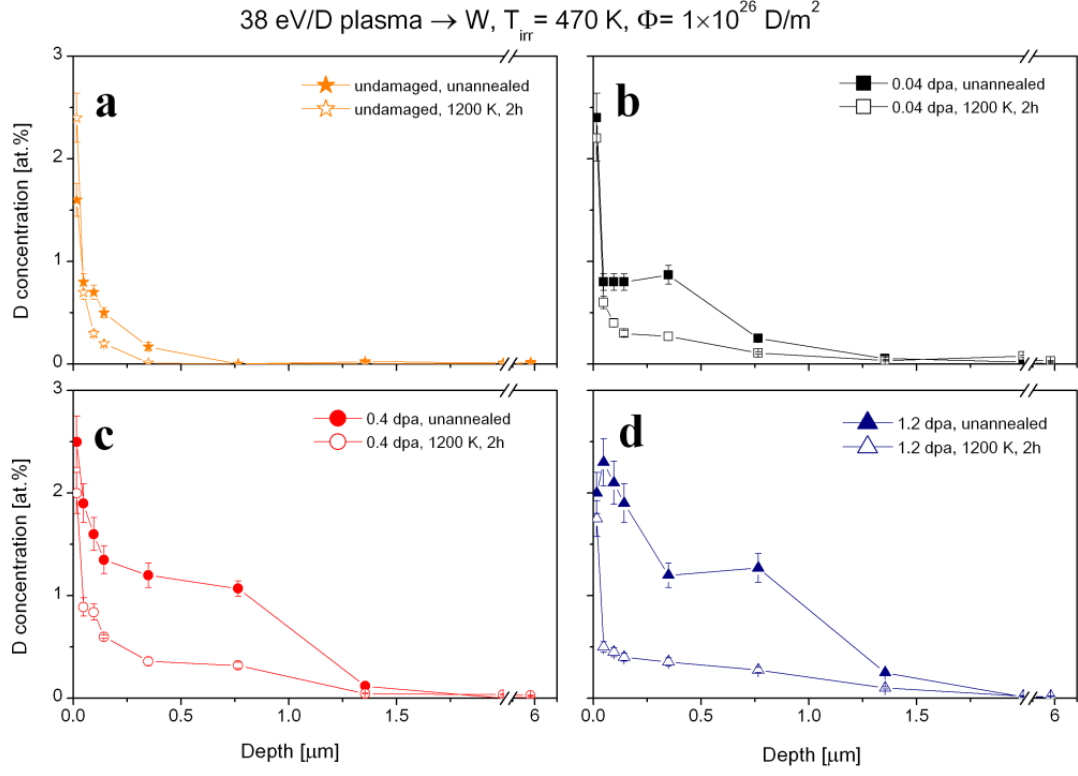
Figure 5.3: Depth profiles of deuterium trapped in PCW, undamaged and pre-damaged with $5.5\,\mathrm{MeV}$ W^{2+} ions to damage levels of 0.04, 0.4, and $1.2\,\mathrm{dpa}$ with and without subsequent annealing at $1200\,\mathrm{K}$ for $2\,\mathrm{h}$, after irradiation with $38\,\mathrm{eV}$ D plasma to a fluence of $1{\times}10^{26}\,\mathrm{D/m^2}$ at $470\,\mathrm{K}$.

fusing from the near-surface layer. Independently of the irradiation temperature, some small changes in the D retention are seen at $0.04\,\mathrm{dpa}$. However, they are definitively more pronounced for 0.4 and $1.2\,\mathrm{dpa}$. At these two higher damage levels, the D depth profiles are similar in shape – comparing identical irradiation temperatures – which suggests trap density saturation. To investigate the general influence of annealing, the D concentration and the depth profiles in the undamaged samples were compared before and after annealing at $1200\,\mathrm{K}$ for $2\,\mathrm{h}$ (see Fig. 5.3a). This reveals that heating at the aforementioned temperature reduces the amount of intrinsic defects like dislocations and grain boundaries (due to partial re-crystallization). This effect was already observed by Ogorodnikova et al. [48]. The D concentration in the damaged and annealed samples is significantly lower than in the un-annealed samples damaged to the same dpa level. For samples from batch B irradiated at $320/350\,\mathrm{K}$, the D depth profiles are

comparable in shape and height with those of the undamaged sample. This also applies to the low-flux irradiation at 470 K. In the case of samples irradiated at a high flux at 470 K (see Fig. 5.3), the D concentration is somewhat higher than for the undamaged samples irradiated at this temperature.

The significant drop of the D concentration upon annealing in the damaged and annealed samples almost to the level which is seen in the undamaged samples suggests major but not complete radiation-induced defect removal by heating at 1200 K for 2 h. These observations are also representative for the implantations at 200 eV in the HCS samples.

5.3   TDS Spectra

This section describes the outcome of the TDS investigations. It is to be noted that the D irradiation at the HCS resulted in an implantation spot of $45\,\mathrm{mm^2}$, whereas the implantation spot size at the Linear Plasma Generator was $50\,\mathrm{mm^2}$. In both cases, the damaged area after W pre-implantation ($40\,\mathrm{mm^2}$) was fully covered by the D irradiation. The difference does not affect the NRA data but may have a small influence on the TDS data. Nevertheless, the results shown below are not normalized to the same area and are left in their original form, instead. Multi-peak Gaussians were fitted to the measured TDS spectra. At most, four peaks were found at different desorption temperatures T_D. They are labeled Peak1 ($< 450\,\mathrm{K}$), Peak2 ($480 - 530\,\mathrm{K}$), Peak3 ($600 - 680\,\mathrm{K}$), and Peak4 ($\sim 820\,\mathrm{K}$). Irradiation at 470 K shifts T_D toward higher values (see Fig. 5.6). The reason for that is a higher D diffusivity for 470 K than for 320/350 K which means that D can penetrate more deeply into the bulk and also, in consequence, needs more time to be released during the TDS measurements. Thus, if one groups the temperatures T_D, this corresponds to the results obtained from the 320/350 K irradiation.

5.3.1   Low-Flux Irradiation

Here, the TDS results obtained from samples irradiated at low flux at the HCS are presented. When showing some general tendencies, data from high-flux irradiation is also used.

Undamaged tungsten

Thermal desorption spectra for undamaged and damaged W samples irradiated with D ions to a fluence of $3\times10^{24}\,\mathrm{D/m^2}$ at 320 K are shown in Fig. 5.4. The spectrum measured for the undamaged target (orange stars) reveals two peaks at $T_\mathrm{D} \sim 450$ and $\sim 630\,\mathrm{K}$. These peaks were already observed by Ogorodnikova et al. [45] in the PCW samples
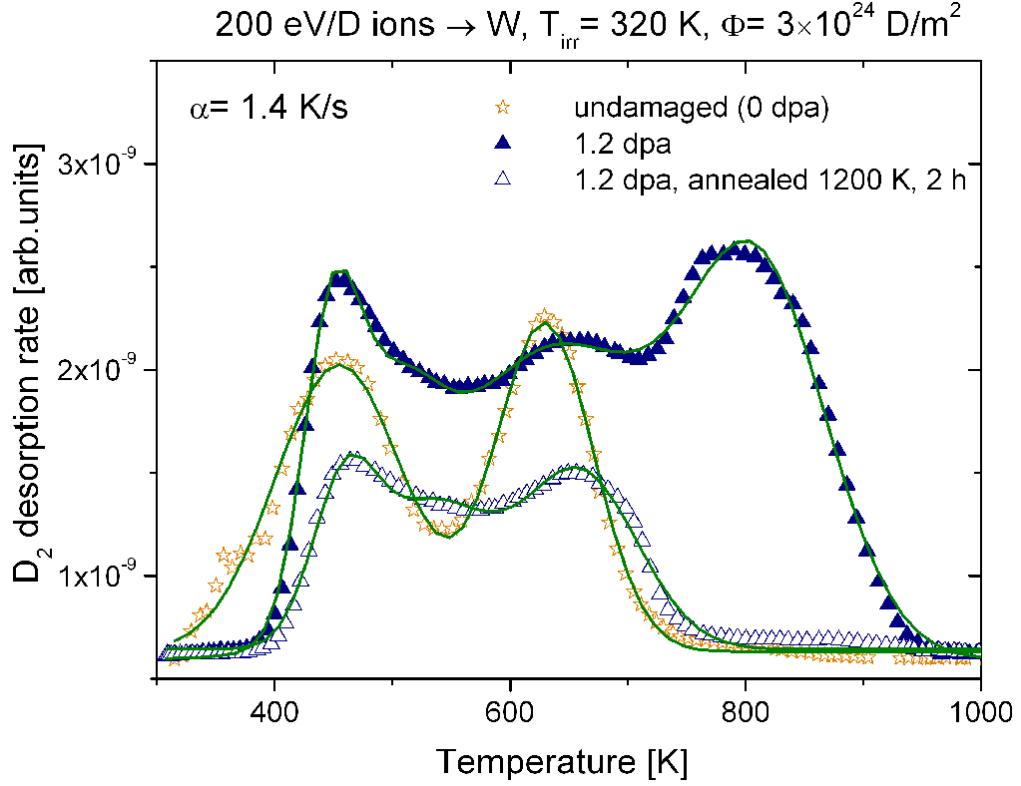
Figure 5.4: Experimental TDS spectra of undamaged (outgassed), damaged up to 1.2 dpa, and damaged up to 1.2 dpa and post-annealed PCW samples irradiated with 200 eV D ions at 320 K to a fluence of 3×10^{24} D/m^2. Green lines show multi-peak Gaussian fits. The heating ramp was $\alpha = 1.4$ K/s.

produced for Iter by Plansee. Based on modeling, the low-temperature Peak1 with $T_D \sim 450$ K was associated with the natural traps present in the material (dislocations, grain boundaries), while the intermediate-temperature Peak3 with $T_D = 600 - 650$ K was attributed to D agglomeration in molecules in bubbles near the implanted surface, as well as to D trapping in vacancies.

Damaged tungsten

The TDS spectra measured from the un-annealed, damaged W (see Fig. 5.4: solid, blue triangles) clearly shows that high-energy trap sites are present in the sample. Peak4 at T_D around 820 K is observed only in the present case of the damaged un-annealed samples (see Figs. 5.4 and 5.5). Additionally, desorption at $T_D = 480 - 530$ K is present (see Fig. 5.6). This means that pre-implantation produces not only high-
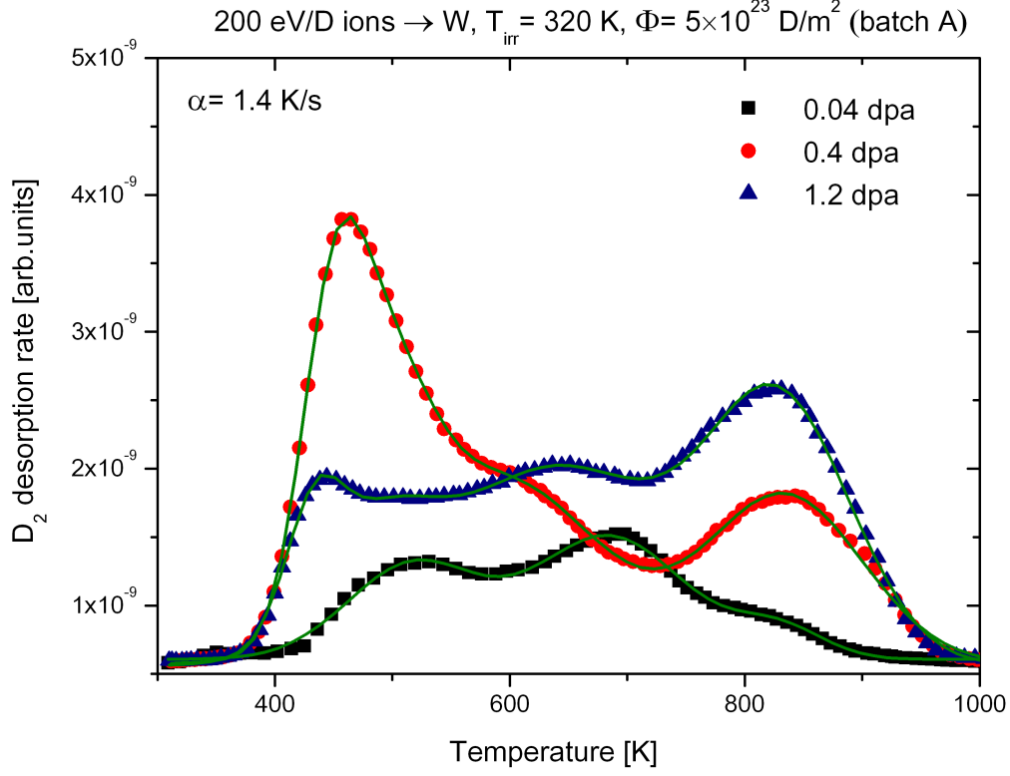
Figure 5.5: Experimental TDS spectra of PCW samples damaged to 0.04, 0.4, and 1.2 dpa, irradiated with $200\,\text{eV}$ D^+ ions at $320\,\text{K}$ to a fluence of $5{\times}10^{23}\,\text{D/m}^2$. Green lines show the final results of multi-peak Gaussian fits. The heating ramp was $\alpha = 1.4\,\text{K/s}$.

energy traps but also lower-energy ones. D_2 desorption at ~ 450 and $600 - 680\,\text{K}$ like in the undamaged W takes place in the damaged samples. Fig. 5.5 shows TDS spectra obtained for W samples damaged at three different levels and irradiated with D ions to a fluence of $5 \times 10^{23}\,\text{D/m}^2$ at $320\,\text{K}$. This figure also illustrates the high-temperature peak amplitude dependence on the damage level. For samples damaged to $0.04\,\text{dpa}$ (black squares), only a broad shoulder is observed, suggesting that W self-implantation at this damage level did not introduce many defects. With increasing dpa the height of the high-temperature peak is growing. In order to clarify whether saturation in this peak takes place, D retention at higher than $1.2\,\text{dpa}$ was studied in the context of a different investigation (see Ch. 6). The peak at around $820\,\text{K}$ had already been observed by Fukumoto et al. [12, 13], by Arkhipov et al. [14], and by Oliver et al. [11]. Fukumoto attributed it to D desorption from vacancy clusters. Oliver, in contrast, claims that D release at this temperature cannot be ascribed to ion-induced defects but to natural

traps present in W, instead, which does not agree with the present data.

Some TDS spectra measured on damaged tungsten samples revealed an interesting behavior of D de-trapping from the low-energy traps (see Figs. 5.5 (red circles)). In some cases, the amount of D desorbed at $\sim 450\,\mathrm{K}$ is very high in comparison with other samples, an observation which is independent of the irradiation temperature and flux. The origin of this behavior is explained by Wright et al. [120] as a result of exposure temperature fluctuations, but in this case, it could be a result of an inaccurate positioning of the sample in the D irradiation device. Small shifts in the sample position can lead to a situation where the damage area is not completely covered by the D irradiation spot, and thus, a higher D desorption from the intrinsic defects is registered.

5.3.2   High-Flux Irradiation

Instead of showing TDS spectra from samples implanted at a high-flux to a fluence of $1 \times 10^{26}\,\mathrm{D/m^2}$, results from Gaussian fits are plotted in Fig. 5.6. This hides any information about relative contributions to each of the desorption peaks but highlights its remarkable reproducibility. In general, the results are comparable with those obtained for samples irradiated at low flux, but there are some small differences. Only one undamaged sample, irradiated at $350\,\mathrm{K}$, displays a desorption peak at $\sim 450\,\mathrm{K}$. In the case of the low-flux implantations at $320\,\mathrm{K}$, all samples displayed this peak. This may be because of the slightly higher irradiation temperature of $350\,\mathrm{K}$.

Damaged, un-annealed targets irradiated at $350\,\mathrm{K}$ have three peak temperatures T_D at $\sim 520\,\mathrm{K}$, $\sim 640\,\mathrm{K}$, and $\sim 770\,\mathrm{K}$. Surprisingly, no peak was seen at $\sim 820\,\mathrm{K}$. Annealing at $1200\,\mathrm{K}$ for $2\,\mathrm{h}$ results in a reduction of the desorption peaks to only two at $T_\mathrm{D} \sim 530\,\mathrm{K}$ and $\sim 680\,\mathrm{K}$. Thus, one can conclude that the post-annealing removes high-energy traps with T_D around $770\,\mathrm{K}$, which is quite similar to the aforementioned observations made for the low-flux irradiation case.

As already mentioned, irradiation at $470\,\mathrm{K}$ results in shifting T_D towards higher values. Therefore, the observed T_D for samples from batch A are $\sim 560\,\mathrm{K}$, $\sim 660\,\mathrm{K}$, and $\sim 820\,\mathrm{K}$; and very similar for batch B: $\sim 580\,\mathrm{K}$, $\sim 660\,\mathrm{K}$, and $\sim 820\,\mathrm{K}$. It is astonishing that there is a peak – or rather, a broad shoulder – present at $\sim 820\,\mathrm{K}$ (Peak4) in the post-annealed samples (also in the case of the low-flux samples). Its relative contribution to the total D retention is smaller ($\sim 10\%$) than in the case of the damaged, un-annealed samples ($\sim 35\%$). The presence of these traps can explain the slightly higher D concentration which was seen in the damaged, annealed samples in comparison with the undamaged targets (see Fig. 5.3).
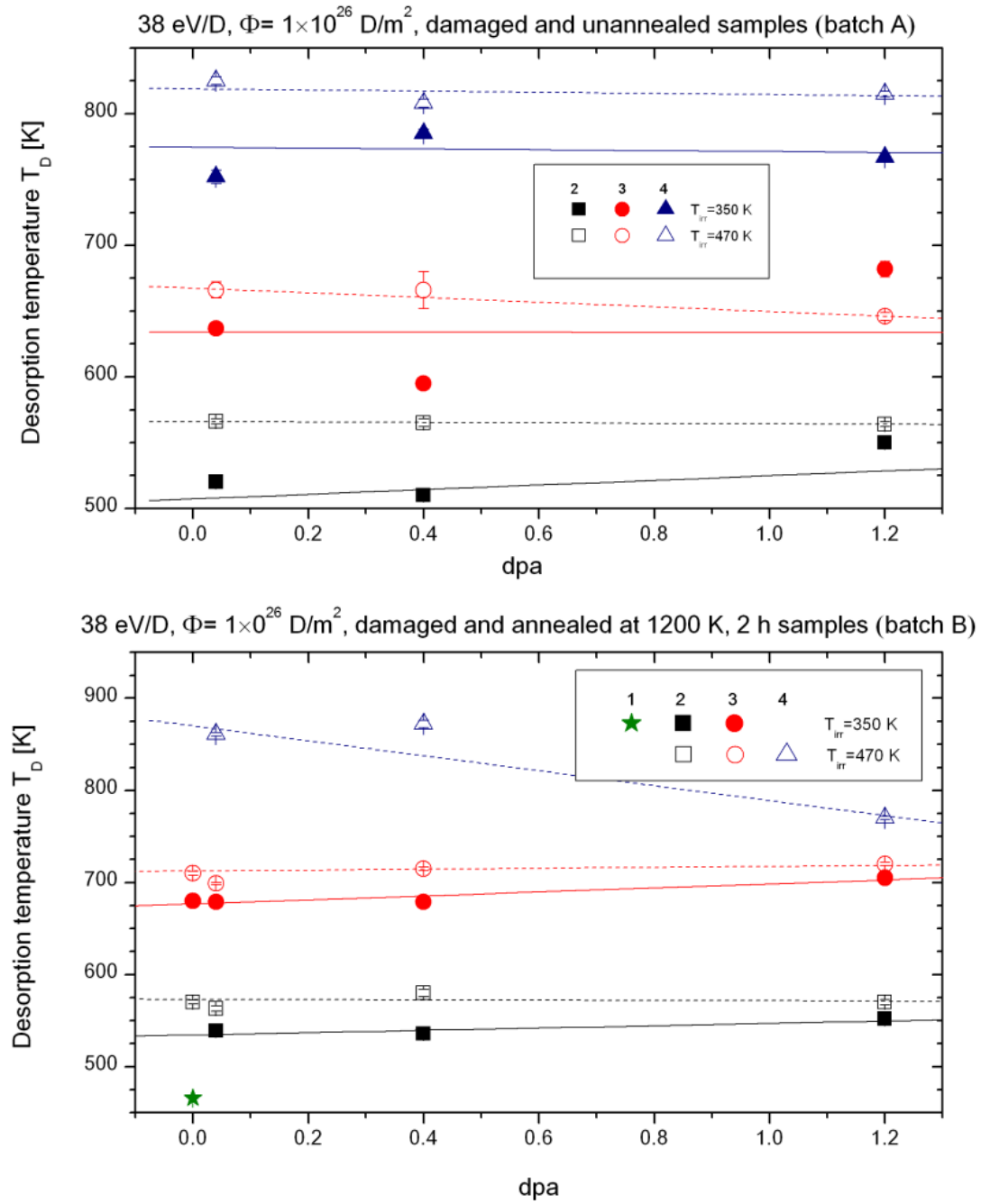
Figure 5.6: Desorption temperatures obtained by fitting Gaussians to the TDS spectra measured on samples irradiated to a fluence of $1 \times 10^{26}\,\mathrm{D/m^2}$ either at $T_{\mathrm{irr}} = 350\,\mathrm{K}$ (solid symbols) or at $T_{\mathrm{irr}} = 470\,\mathrm{K}$ (empty symbols). The upper plot shows data for the samples from batch A, and the lower for those from batch B. The numbers 1 to 4 correspond to Peak1 to Peak4, respectively. Solid lines represent linear fits to the $T_{\mathrm{irr}} = 320/350\,\mathrm{K}$ data, dashed lines to the $T_{\mathrm{irr}} = 470\,\mathrm{K}$ data.

5.3.3 Annealing

D_2 desorption at ~ 450, $480 - 530$, and $600 - 680\,\mathrm{K}$ (see Fig. 5.4: empty, blue triangles) takes place in the damaged, post-annealed samples, much like in the undamaged W. Depending on the sample, Peak4 was either not observed $(320/350\,\mathrm{K})$, or sometimes only a broad shoulder at low levels was registered $(470\,\mathrm{K})$. This means that heating at $1200\,\mathrm{K}$ for $2\,\mathrm{h}$ almost completely removes defects with $T_\mathrm{D} \sim 820\,\mathrm{K}$ while it decreases the amount of intermediate-temperature traps with $T_\mathrm{D} = 480 - 530\,\mathrm{K}$.

In their work, Oliver et al. [11] observed full trap removal after annealing at $1200\,\mathrm{K}$ for $6\,\mathrm{h}$. This is in good agreement with the result shown here. Because of this, it is believed that the traps introduced by self-implantation are vacancy clusters and not voids as suggested by van Veen et al. [15]—the temperature of $1200\,\mathrm{K}$ is too low to anneal voids [56]. Eleveld and van Veen [121] suggest that the combination of a D desorption temperature of $800\,\mathrm{K}$ and a defect removal temperature of $1150 - 1350\,\mathrm{K}$ can be attributed to the presence of VCs composed from 11 to 16 vacancies. The assumption that deuterium is being trapped by vacancy clusters is supported by FIM studies where no voids but interstitials, vacancies, and vacancy clusters were observed in W irradiated with neutrons [96–98]. Additionally, Keys et al. [99] and Keys and Moteff [87] report the recovery of n-induced defects mainly at $\sim 0.15\,T_\mathrm{m}$ and $\sim 0.31\,T_\mathrm{m}$, where T_m is the W melting temperature. $0.15\,T_\mathrm{m}$ corresponds to Stage III and is attributed to interstitial annihilation in immobile vacancies. Stage IV at $0.31\,T_\mathrm{m}$ is attributed to vacancy and vacancy cluster recovery. According to these studies, full defect removal takes place at around $1350\,\mathrm{K}$. The de-trapping temperature of deuterium from vacancy clusters at $800\,\mathrm{K}$ and the almost complete ion-induced defect removal at $1200\,\mathrm{K}$ are in good agreement with the aforementioned studies.

5.3.4 Fluence Dependence

Fig. 5.7 shows D depth profiles measured up to $6\,\mu\mathrm{m}$ and TDS spectra obtained from W damaged to $1.2\,\mathrm{dpa}$ and then irradiated at $320/350\,\mathrm{K}$ to three different D fluences. Both figures show the D retention to be independent of the D irradiation fluence. Although between the lowest and the highest fluence, the difference is a factor of 200, there is not much increase of the D inventory. This is a surprising result when considering the lack of saturation and the increase of the D retention in the undamaged W with an ion fluence at RT as $\sim \Phi^{0.5-0.7}$ up to a fluence above $5 \times 10^{24}\,\mathrm{D/m^2}$ [49]. Theoretically, when there are more defects to populate, D saturation should appear at higher fluences. The analysis of the relative D content (see Fig. 5.8) in each of the four desorption peaks (three peaks for the highest fluence irradiation due to the higher T_irr) shows constant
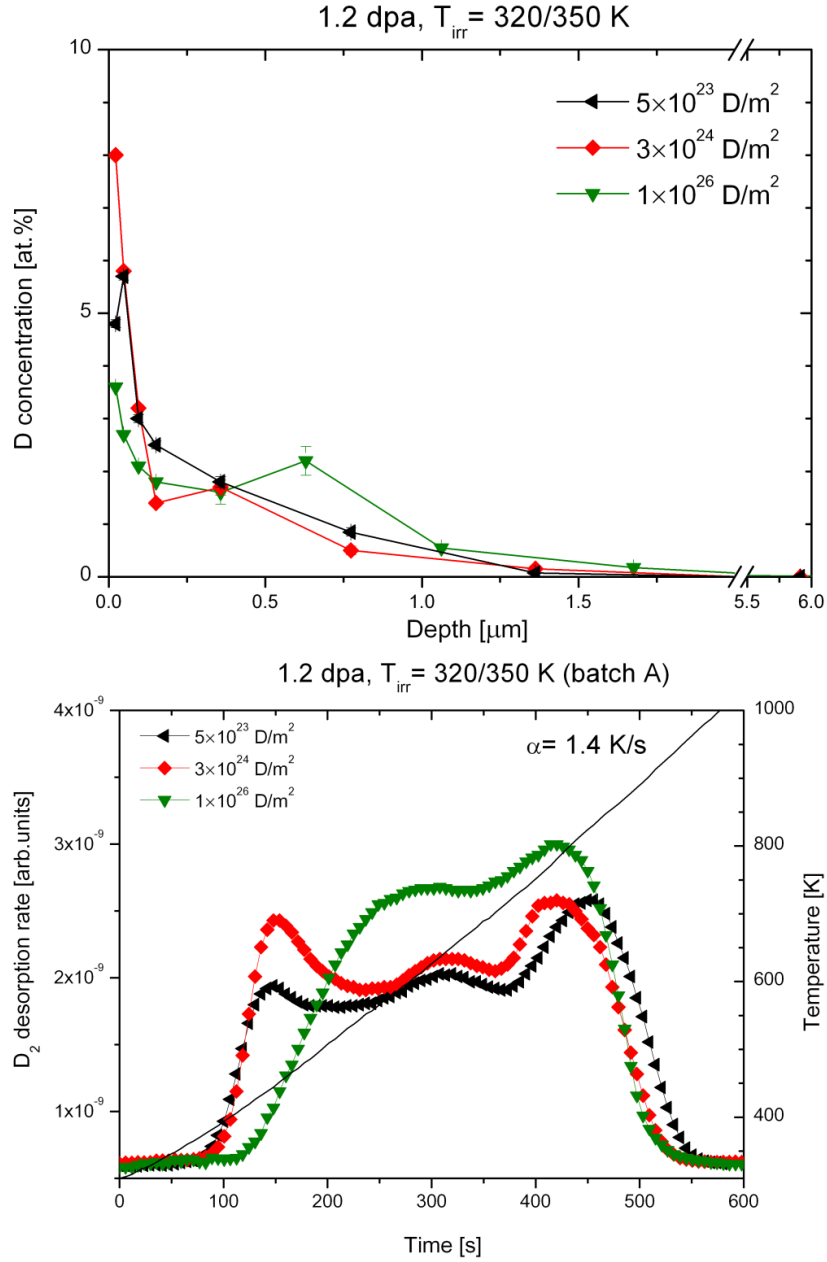
Figure 5.7: Depth profiles and TDS spectra of deuterium trapped in PCW samples damaged to 1.2 dpa and then either irradiated with 200 eV D ions to fluences of 5×10^{23} D/m^2 and 3×10^{24} D/m^2 at 320 K or exposed to D plasma to a fluence of 1×10^{26} D/m^2 at 350 K. The black line shows the temperature ramp.
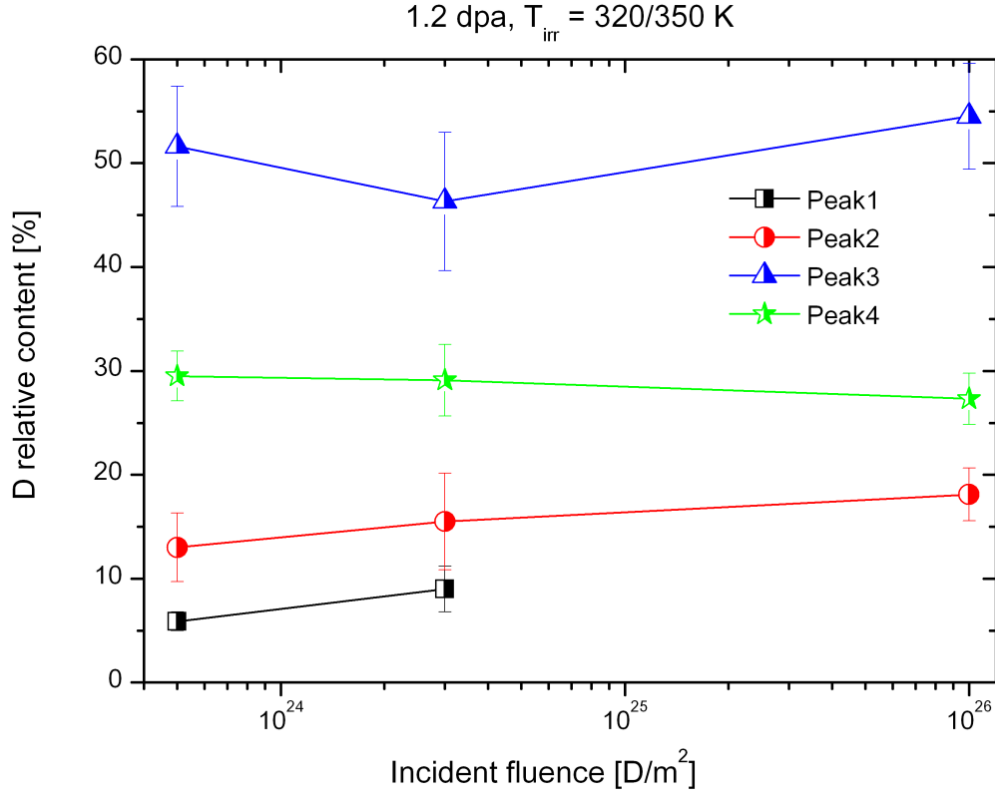
Figure 5.8: Relative D content in each desorption peak as a function of the incident fluence, obtained from the PCW samples damaged to $1.2\,\mathrm{dpa}$ and then either irradiated with $200\,\mathrm{eV}$ D ions to fluences of $5\times10^{23}\,\mathrm{D/m^2}$ and $3\times10^{24}\,\mathrm{D/m^2}$ at $320\,\mathrm{K}$ or exposed to D plasma to a fluence of $1\times10^{26}\,\mathrm{D/m^2}$ at $350\,\mathrm{K}$.

levels which suggests saturation already at the D irradiation to the lowest fluence of $5\times10^{23}\,\mathrm{D/m^2}$. The relative deuterium content in Peak1 to Peak4 is approximately 7%, 15%, 51%, and 29%, respectively.

5.4 Retention

Fig. 5.9 shows the damage level dependence of D retention up to $6\,\mu\mathrm{m}$ in undamaged, pre-implanted, as well as in pre-implanted and post-annealed W irradiated at 320/350 and $470\,\mathrm{K}$. In the samples from batch A, a nonlinear increment of the D retention with dpa was observed which approaches saturation at around $0.4\,\mathrm{dpa}$. Furthermore, only a small influence of the D implantation fluence on the onset of the saturation is visible. This means that a linear increase of the dpa does not lead to a linear increase of the trap
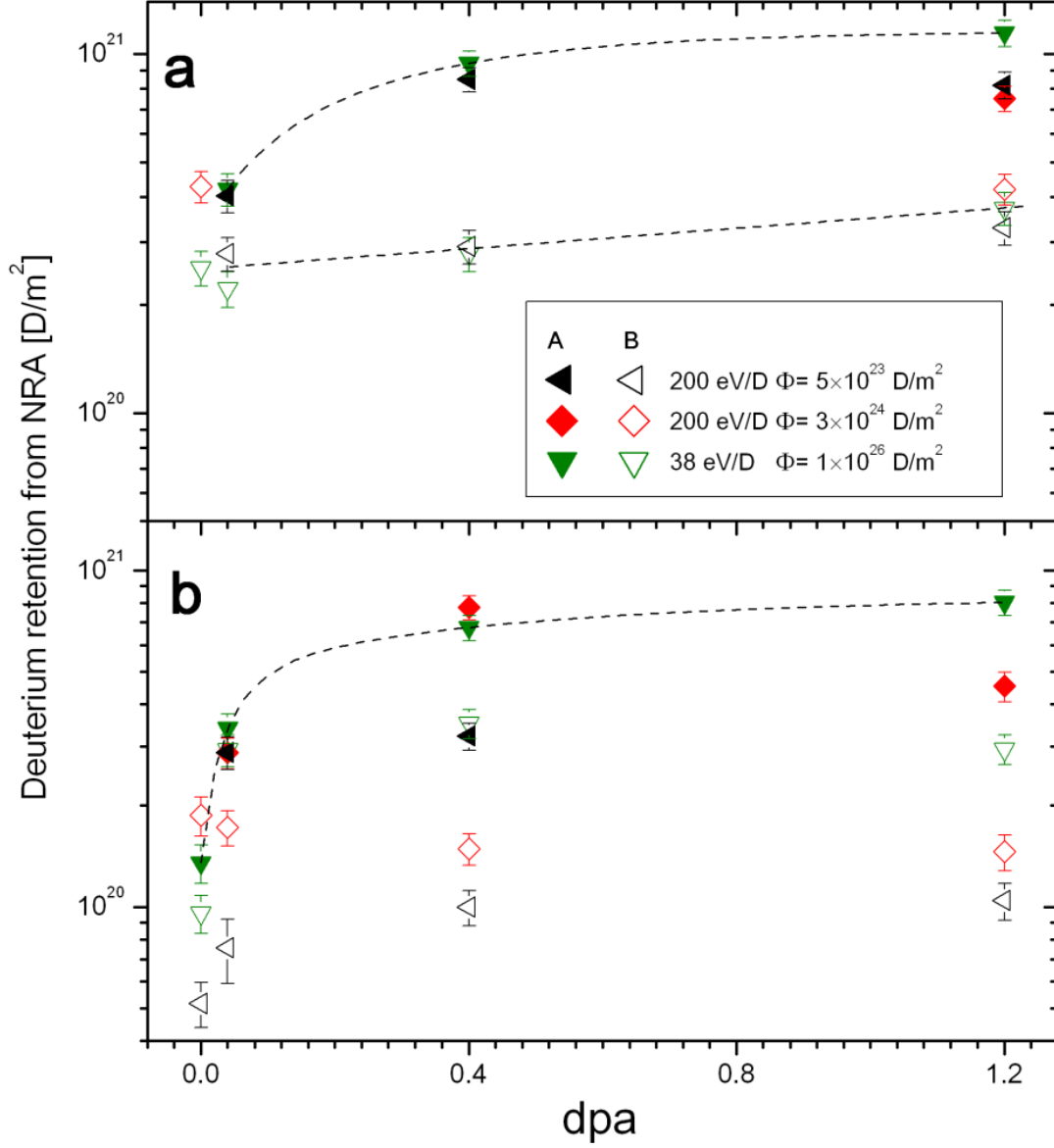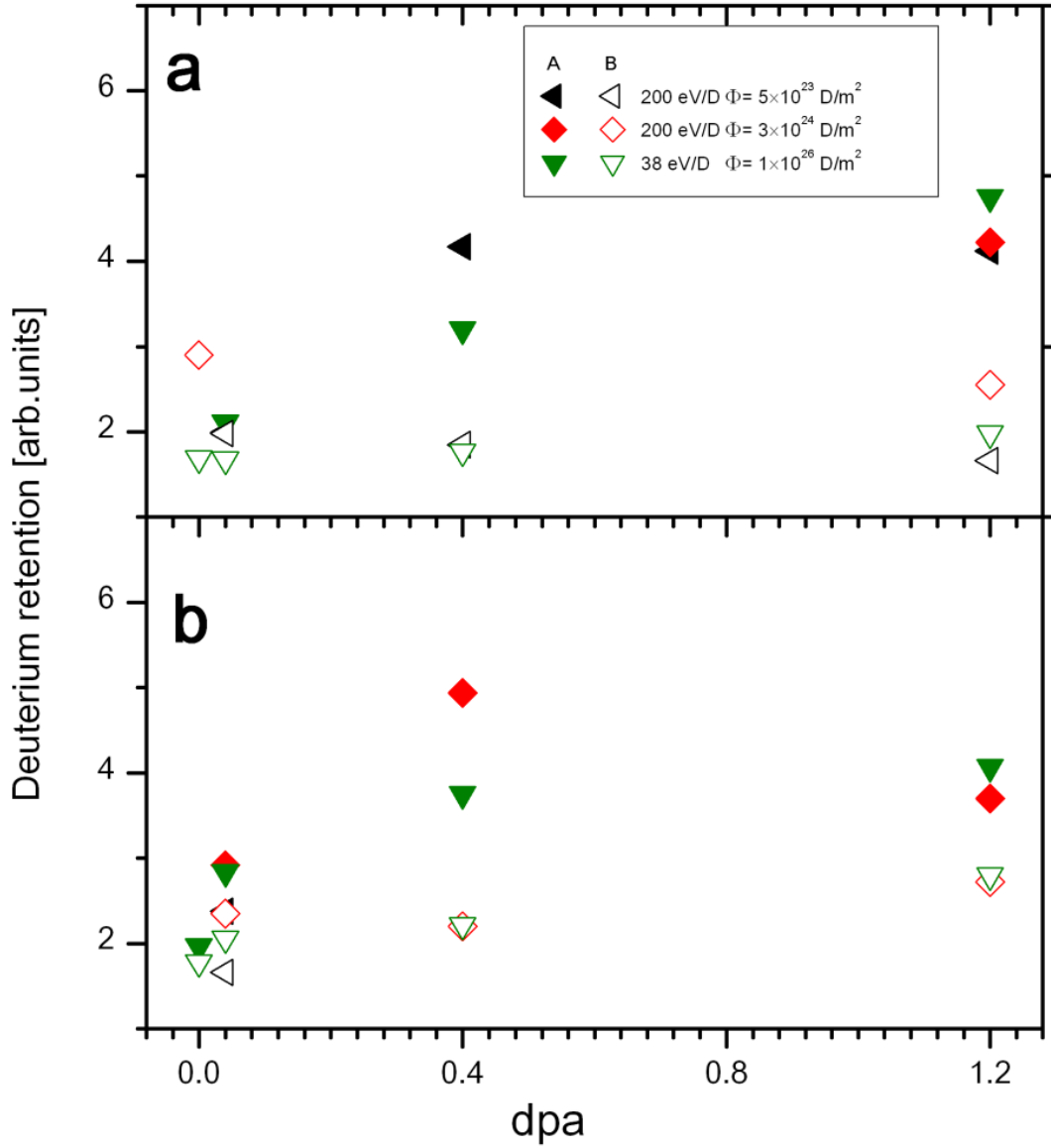
Figure 5.9: Deuterium retention up to $6\,\mu$m (taken from NRA) vs. the number of displacements per atom for W, undamaged and pre-damaged with $5.5\,$MeV W^{2+} ions to damage levels of 0.04, 0.4, and 1.2 dpa with and without subsequent annealing at 1200 K for 2 h, after irradiation with 38 and 200 eV D at 320/350 K (a) and 470 K (b), to ion fluences of 5×10^{23}, 3×10^{24}, and $1 \times 10^{26}\,$D/m^2. Data for the samples without (batch A) and with annealing (batch B) are indicated by solid and empty symbols, respectively. Dashed lines are included to provide a visual aid.

Figure 5.10: Deuterium total retention (taken from TDS) vs. the number of displacements per atom for W, undamaged and pre-damaged with $5.5\,\mathrm{MeV}$ W^{2+} ions to damage levels of 0.04, 0.4, and 1.2 dpa with and without subsequent annealing at $1200\,\mathrm{K}$ for $2\,\mathrm{h}$, after irradiation with 38 and $200\,\mathrm{eV}$ D at $320/350\,\mathrm{K}$ (a) and $470\,\mathrm{K}$ (b), to the ion fluences of 5×10^{23}, 3×10^{24}, and $1\times10^{26}\,\mathrm{D/m^2}$. Data for the samples without (batch A) and with annealing (batch B) are indicated by solid and empty symbols, respectively.

density (see Fig. 5.11). Retention in all samples with post-annealed defects is similar
for the low-temperature implantations and comparable to the retention in undamaged
targets (see Fig. 5.9a). In the case of the samples from batch B which were irradiated
at 470 K (see Fig. 5.9b), the dependence of the D retention on the implantation fluence
is fairly pronounced. The D diffusion at 470 K is higher and can therefore reach traps
which are located deeper in the sample. For all samples, the D concentration at up to
$6\,\mu$m is higher for 320/350 K irradiation than for 470 K. When looking at un-calibrated
TDS data (see Fig. 5.10), this tendency is slightly reversed, suggesting higher bulk D
retention for samples implanted at 470 K, an effect which is not unexpected due to the
higher diffusion of D at this temperature.

The total D retention depends on the width of the damage zone. In the region at
$0.2-0.7\,\mu$m, the maximum D retention enhancement between damaged and undamaged
targets was measured to be around 5 and up to 8 times higher for the samples irradiated
at 320/350 K and 470 K, respectively.

5.4.1 Trap Density

Information about the trap density ρ_{tr} introduced by ion irradiation can be obtained
directly from NRA measurements while making the assumption that all traps are pop-
ulated and one trap corresponds to one D atom [16, 18]. This does not always hold
true, and since both conditions overestimate the trap density, this means that these as-
sumptions give an upper limit for the number of traps present in the material. Only the
data obtained at RT provides the initial level of traps (see Fig. 5.11: violet stars), but
the data obtained at 470 K (see Fig. 5.11: pink stars) is also important since tokamaks
are operated at elevated temperatures. Irradiation at higher temperatures prevents D
from being trapped in weaker traps. Nonetheless, the D retention information can still
be extracted. The trap density shown in Fig. 5.11 was obtained from the $0.2-0.7\,\mu$m
damaged region (excluding the near-surface concentration from the $0-0.2\,\mu$m region)
by taking the average of all three D irradiation fluences (based on the D retention inde-
pendence of the D irradiation fluence, see Sec. 5.3.4). With increasing dpa, ρ_{tr} increases
and then approaches saturation at 0.4 dpa which corresponds to Iter's dpa at the end
of its lifetime (recalculated for $E_{\text{th}} = 68\,$eV). The observed plateau at $\rho_{\text{tr}} \sim 1.6\%$ is a
few orders of magnitude higher than the typical amount of intrinsic defects present in
tungsten (i.e., $\sim 5\times10^{-4}\,$at.%). The difference in ρ_{tr} between RT and 470 K is roughly
20%, which corresponds to the D amount trapped in Peak1 and Peak2 (see Sec. 5.3.4).
Assuming total trap saturation at all temperatures, one can calculate the fraction of
traps in each peak by comparing the contribution of each peak to the total retained
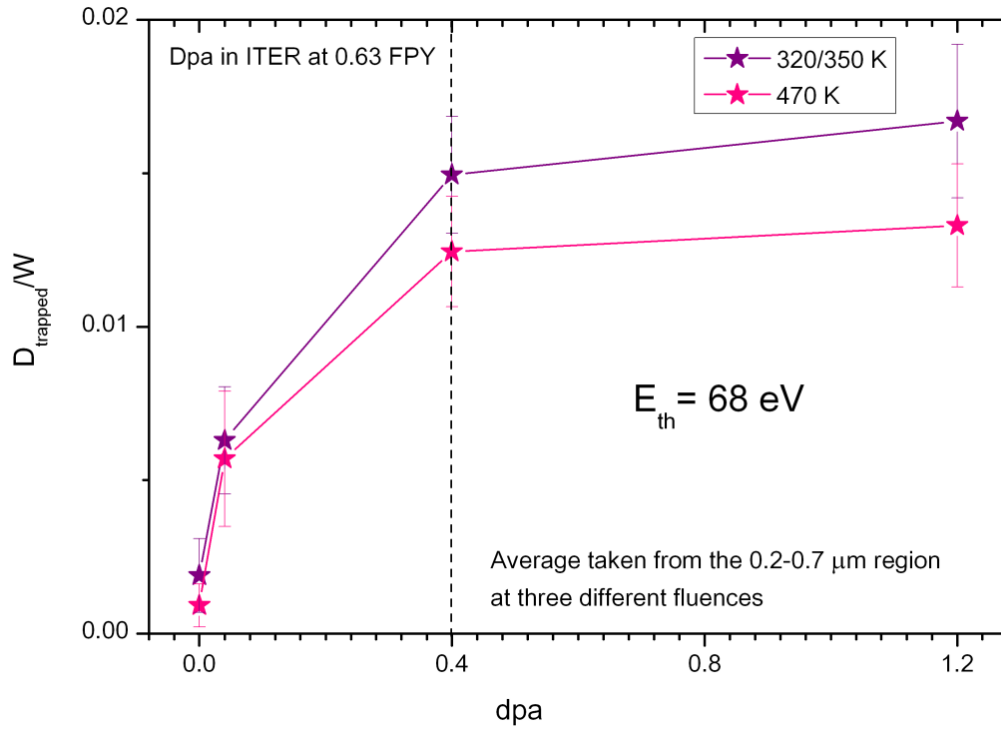
Figure 5.11: Trapped D-to-W ratio (trap density) in the region at $0.2 - 0.7\,\mu$m vs. the number of displacements per atom for PCW irradiated at $320/350$ and 470 K. The damage levels were calculated with SRIM-2008.03 using a threshold energy of 68 eV. The vertical dashed line indicates the estimated end-of-lifetime damage in Iter.

amount at different temperatures. Following this observation, one can conclude that the $\rho_{\rm tr}$ present during irradiation above 700 K should be less than a third of the initial assessment, meaning 0.45% (see Fig. 5.8). This value is of great importance for any estimation of the T inventory in Iter.

5.5   Surface Morphology

The low energies, high fluxes, and relatively low irradiation temperatures used in this work are perfect conditions for W blistering. The influence of damage and deuterium flux on the W surface and the sub-surface region was investigated by means of SEM and FIB (see Sec. 4.4). To examine the effect of W pre-implantation, the pictures taken from the undamaged W and the samples damaged to 0.04 and 1.2 dpa were compared, revealing no differences and showing no signs of erosion which is in good agreement with
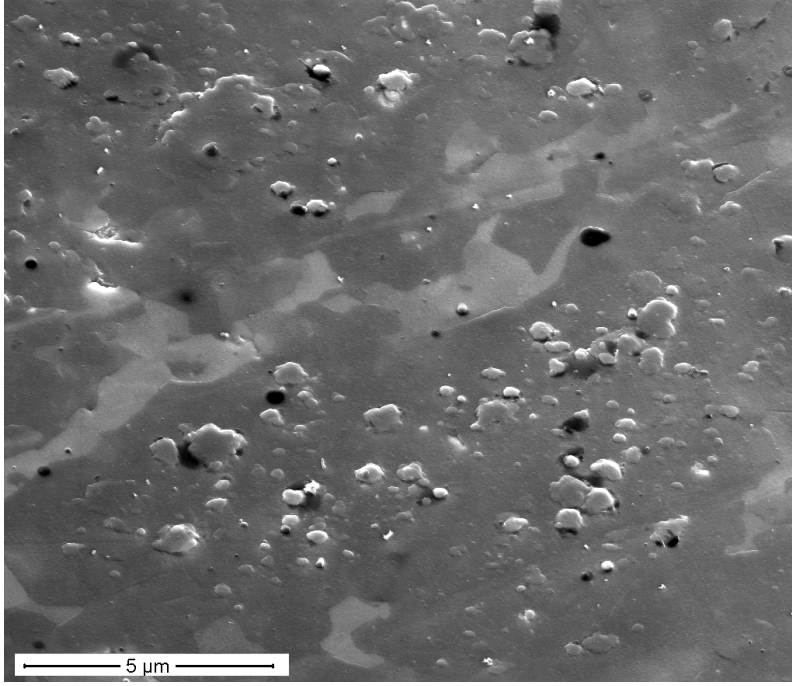
Figure 5.12: SEM image of an undamaged PCW irradiated by $200\,\mathrm{eV}$ D to a fluence of $3{\times}10^{24}\,\mathrm{D/m^2}$ at $320\,\mathrm{K}$.

TRIM code calculations (note that a fluence of $10^{18}\,\mathrm{W/m^2}$ corresponds to an eroded depth of $0.06\,\mathrm{nm}$).

5.5.1   Low-Flux

The surface of an undamaged W sample exposed to a fluence of $3{\times}10^{24}\,\mathrm{D/m^2}$ displayed blisters with diameters $<\ 1\,\mu\mathrm{m}$ (see Fig. 5.12). No cracks had formed underneath these blisters. These results are not surprising because – as discussed in Sec. 2.5 – D irradiation is capable of creating blisters even if the irradiation energy is well below the displacement threshold. The kind of blisters like those shown in Fig. 5.12 were already observed by Wang et al. [68] ($1\,\mathrm{keV/D}$, flux $5{\times}10^{19}\,\mathrm{D/(m^2s)}$, $\Phi = 1{\times}10^{24}\,\mathrm{D/m^2}$, RT) and Alimov et al. [122] (PCW, $200\,\mathrm{eV/D}$, flux $3.6{\times}10^{19}\,\mathrm{D/(m^2s)}$, $\Phi = 1{\times}10^{24}\,\mathrm{D/m^2}$, $T_{\mathrm{irr}} = 323\,\mathrm{K}$). In the case of low-flux irradiation of damaged samples, neither blister nor crack production were observed. Instead, all investigated samples had some erosion-like structures present on the surface (see Fig. 5.13). Their density was changing for different grains, suggesting a dependence on the grain orientation. As previously mentioned, such structures cannot be the result of erosion due to W self-implantation.
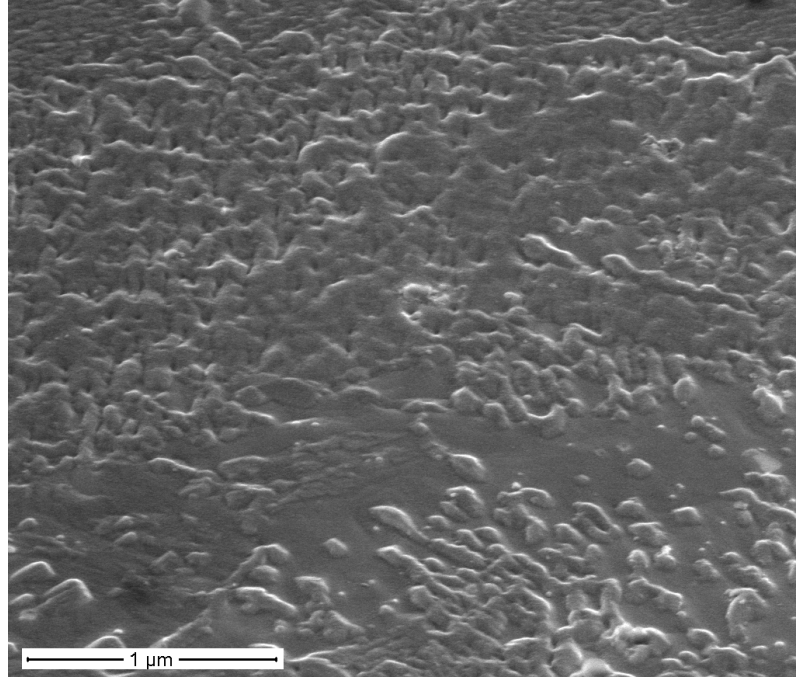
Figure 5.13: SEM image of a PCW pre-damaged with $5.5\,\mathrm{MeV}\,\mathrm{W}^{2+}$ ions to $0.04\,\mathrm{dpa}$ and then exposed to low-energy $(200\,\mathrm{eV})$ D ions at $320\,\mathrm{K}$ to an ion fluence of $5\times10^{23}\,\mathrm{D/m}^2$.

5.5.2 High-Flux

High-flux irradiations are more important as the they are relevant to Iter. In the case of undamaged W exposed to D plasma, either cracks formed just below the surface (not shown), and the surface morphology was characterized by small dense blisters ($< 1\,\mu$m in size), or peculiar patterns appeared on the surface (see Fig 5.14). A slightly different pattern was already observed by Shu [72] on the surface of tungsten targets irradiated under exactly the same conditions (re-crystallized W, $99.99\,\mathrm{wt.\%}$, $38\,\mathrm{eV/D}$, flux $1\times10^{22}\,\mathrm{D/(m}^2\mathrm{s)}$, $\Phi = 1\times10^{26}\,\mathrm{D/m}^2$, $T_{\mathrm{irr}} = 315\,\mathrm{K}$) as in the present work. He suggested that these structures are nuclei for blister and dome growth. A presence of only small blisters not only agrees with the observations of Shu [72] but also with Luo et al. [73] (powder metallurgy W, $99.99\,\mathrm{wt.\%}$, $38\,\mathrm{eV/D}$, flux $1\times10^{22}\,\mathrm{D/(m}^2\mathrm{s)}$, $T_{\mathrm{irr}} = 293\,\mathrm{K}$) who, at $\Phi = 1\times10^{25}\,\mathrm{D/m}^2$, observed blisters with a maximum size of $2\,\mu$m, and Tokunaga et al. [59] (powder metallurgy W, $100\,\mathrm{eV/D}$, flux $1\times10^{22}\,\mathrm{D/(m}^2\mathrm{s)}$, $\Phi = 1\times10^{26}\,\mathrm{D/m}^2$, $T_{\mathrm{irr}} = 333\,\mathrm{K}$) who saw blisters in the size range between 0.2 and $2\,\mu$m.

The exposure of W samples from batches A and B to a low-energy $(38\,\mathrm{eV/D})$, high-flux
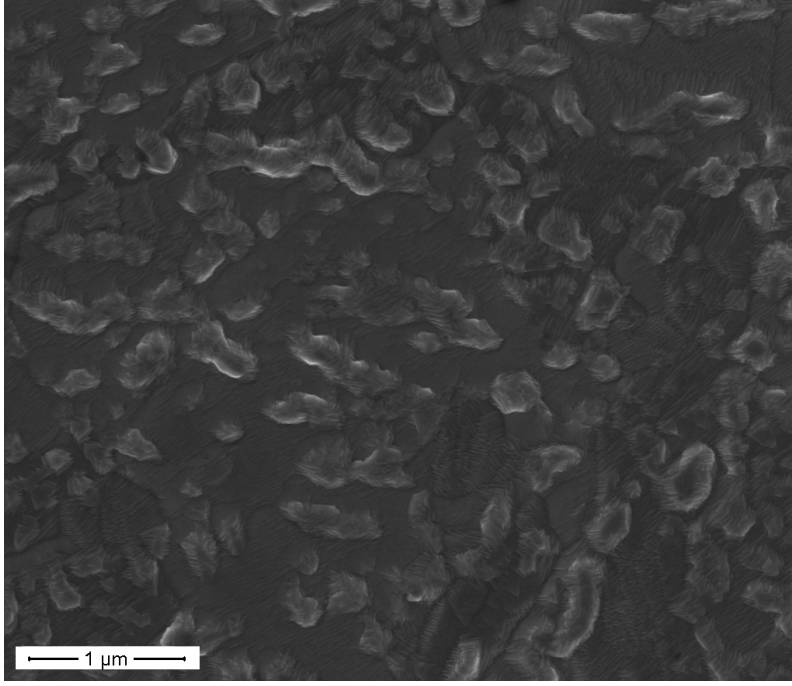
Figure 5.14: SEM image of an undamaged PCW exposed to low-energy $(38\,\text{eV})$ D plasma at $470\,\text{K}$ to an ion fluence of $1 \times 10^{26}\,\text{D/m}^2$.

D plasma to a fluence of $1 \times 10^{26}\,\text{D/m}^2$ led to the appearance of sparse blisters with sizes of $5 - 17\,\mu\text{m}$ on the exposed surface and to the formation of cracks along the grain boundaries far beyond the implantation zone (see Figs. 5.15 and 5.16). The deeper the crack formation took place, the larger was the blister's diameter. This was already seen by Fukumoto et al. [123] who also noted that in damaged samples, cracks are formed beyond the implantation zone. Additionally, on samples irradiated at $470\,\text{K}$, a few plastic dome-shaped buildings – mostly with circular circumference – were found (see Fig. 5.17). Cross-sectioning revealed that a cavity along the grain boundary was always present beneath the dome (see Fig. 5.18). This shows again that grain boundaries play an important role for the growth of cracks and cavities. Nevertheless, both the number of observed domes and the size of the cavities underneath was much smaller than that of those studied by Shu [72], and Shu et al. [74, 75, 76].

The overall crack and blister observations are summarized in Tab. 5.2.
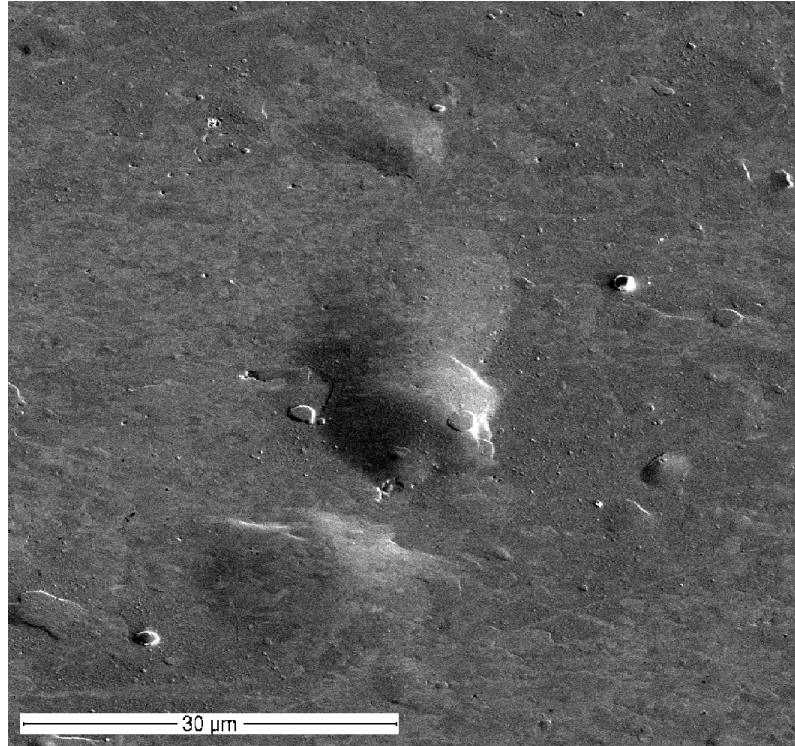
Figure 5.15: SEM image of blister which occurred on the surface of a PCW pre-damaged with $5.5\,\text{MeV}\ W^{2+}$ ions to $1.2\,\text{dpa}$ and then exposed to low-energy ($38\,\text{eV}$) D plasma at $350\,\text{K}$ to an ion fluence of $1\times10^{26}\,\text{D/m}^2$.
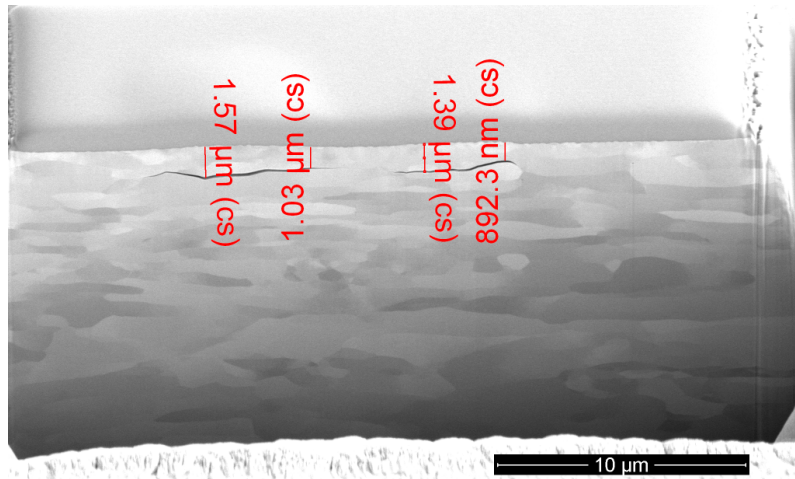

Figure 5.16: Cross-section of the blisters shown in Fig. 5.15. Note that prior to the cross-sectioning the surface had been coated with a Pt-C film. The depth at which cracks appear below the surface is indicated.
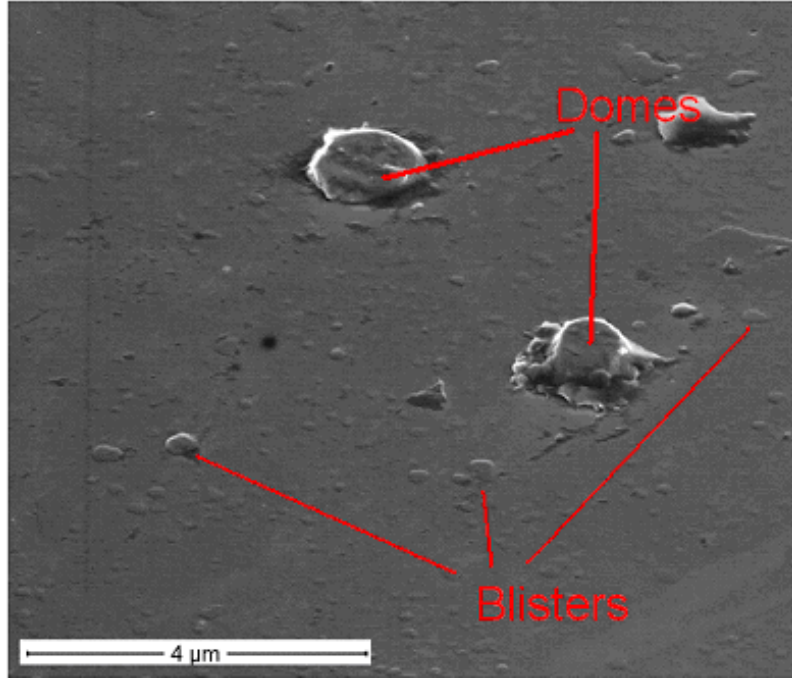
Figure 5.17: SEM image of domes and blisters which occurred on the surface of a PCW pre-damaged with $5.5\,\mathrm{MeV}\;\mathrm{W}^{2+}$ ions to $0.4\,\mathrm{dpa}$ and then exposed to low-energy $(38\,\mathrm{eV})$ D plasma at $470\,\mathrm{K}$ to an ion fluence of $1\times10^{26}\,\mathrm{D/m^2}$.

	low-flux D irradiation $4\times10^{19}\,\mathrm{D/m^2s}$	high-flux D irradiation $1\times10^{22}\,\mathrm{D/m^2s}$
undamaged W	no cracks blisters $< 1\,\mu\mathrm{m}$	cracks at depths $< 0.1\,\mu\mathrm{m}$ blisters $< 1\,\mu\mathrm{m}$
batches A and B	no cracks no blisters	cracks at depth $1-2\,\mu\mathrm{m}$ blisters $5-17\,\mu\mathrm{m}$ sparse domes at $470\,\mathrm{K}$

Table 5.2: Crack and blister sizes as observed by SEM and FIB for undamaged and damaged tungsten irradiated at low and high deuterium flux. The observations are independent of the irradiation temperature.
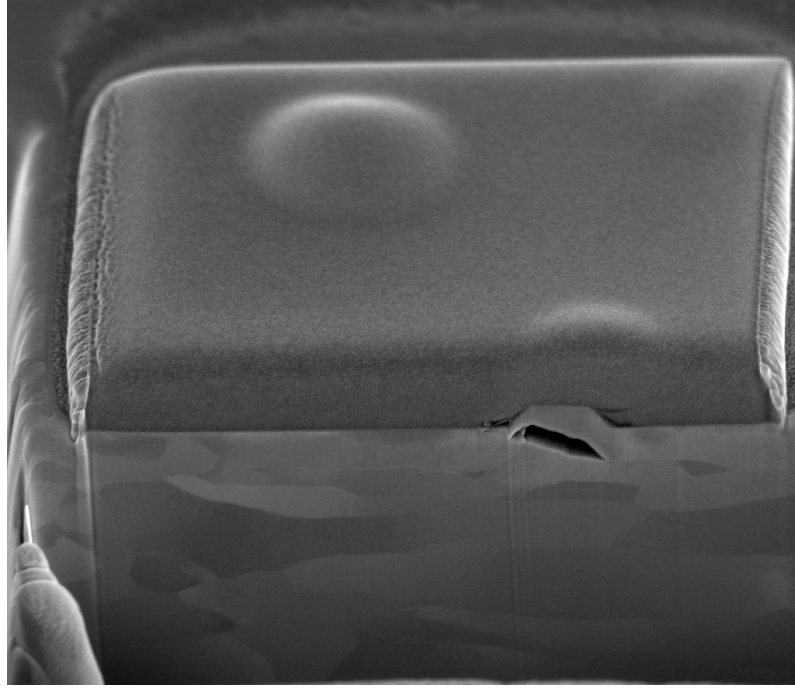
Figure 5.18: Cross-section of one of the dome-shaped structures shown in Fig. 5.17. Note that prior to the cross-sectioning, the surface had been coated with a Pt-C film. A big cavity formed at the grain boundary is revealed under the dome.

5.6 Discussion

5.6.1 Self-Implantation as a Surrogate for Neutrons

There are only a few studies which report defect morphology after tungsten self-implantation [83, 124–129]. All of them use FIM in combination with the field evaporation technique (FET) as a tool for direct defect observation, and thus they are a valuable source of knowledge which can help to answer the basic question whether tungsten self-implantation is a good surrogate for neutrons. Additionally, from the direct FIM investigations, it is known which defects are present or absent in the material. Therefore, these results may be very useful for the interpretation of TDS spectra when describing D desorption at various T_D from different types of defects. Bobkov et al. [83] performed their experiments under conditions similar to those in the present work (see Fig. 5.19). They damaged pure tungsten with $50\,\mathrm{keV}\,W^+$ ions at $300\,\mathrm{K}$ with three different fluences. Depleted zones (i.e., VCs) with a mantel of interstitials lying at a distance of 2.5 nm were registered. These VCs contained from 10 to 30 vacancies and were separated from each
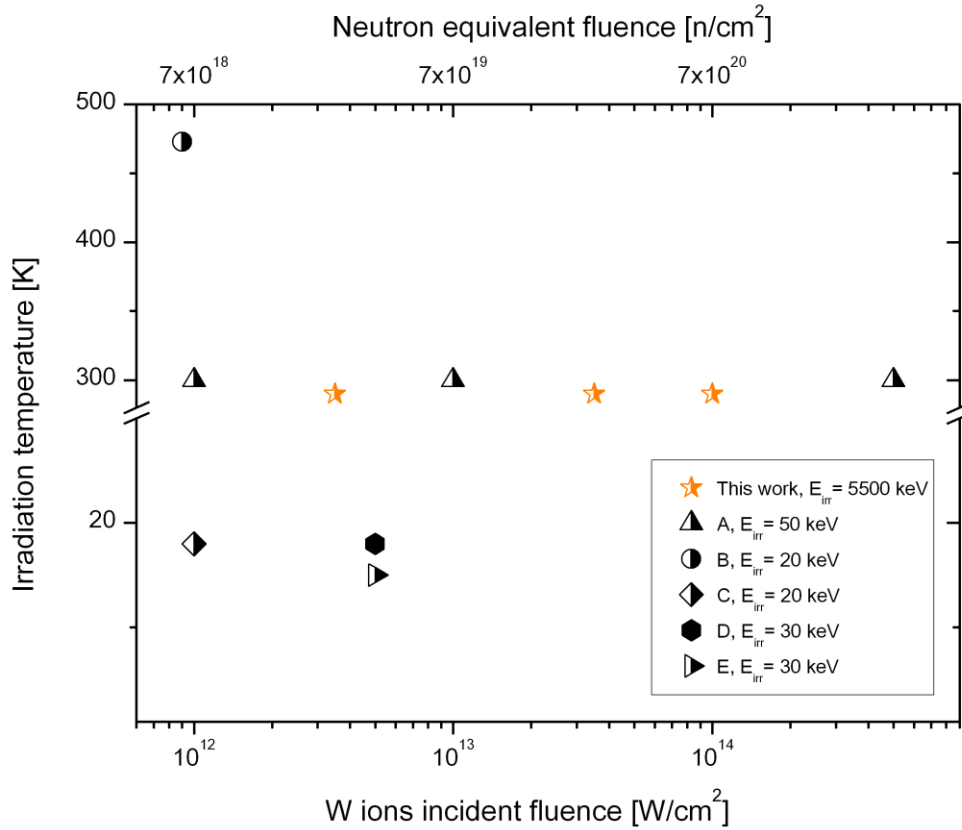
Figure 5.19: Summary of the irradiation conditions: temperatures, incident fluences of W ions/neutron equivalent fluence, and W ion incident energies (in the legend) used in the research on radiation defect formation in self-implanted W taken from (A) Bobkov et al. [83], (B) Wilson and Seidman [124], (C) Beavan et al. [125], (D) Wilson et al. [126], and (E) Wei et al. [127]. For comparison, the parameters from this work are also shown.

other by several nanometers. This already excludes the possibility of void formation, as VCs are immobile at 300 K and cannot transverse such a distance in order to merge. Indeed, at all fluences, microvoids (VCs according to Appendix A) of sizes not greater than 1 nm were detected. Interstitials were also observed, but at numbers two orders of magnitude smaller than those of vacancies. At the lowest implantation fluence of 1×10^{12} W/cm^2, the investigation of separated depleted zones – which were created by single ions – was possible. Further fluence enhancement led to an overlap of these zones which resulted in a decrease of the defect production efficiency, i.e., the intermediate fluence was ten times higher than the lowest one, but this only tripled the number of the created defects.

Wilson and Seidman [124] damaged their tungsten samples at a higher temperature than the one used here, but their temperature of 473 K is the same as the T_{irr} used here for some D irradiations. Wilson observed a depleted zone which consisted of 41 vacant lattice sites clustered in a cubic region of approximately 1.3 nm (in good agreement with Fig. A.2). No interstitials were found, which is in good agreement with the defect recovery studies. Moreover, no voids were detected. Void creation due to damaging was generally not observed after tungsten irradiation by neutrons at RT [87, 96–99, 130, 131] to fluences from 8.5×10^{17} to 1.5×10^{21} W/cm^2 which correspond to the W ions fluences used in the aforementioned self-implantation experiments (see Fig. 5.19). If any voids were identified then only after irradiation at ~ 900 K [100, 132, 133]. Vacancy-type dislocation loops were detected in n-irradiated tungsten, but only after damaged material post-annealing at ~ 1360 K [131, 134]. The aforementioned research lead to the conclusion that tungsten self-implantation is a good substitute for neutrons. Both the depth of the damage zone and the dpa rate are different for neutrons, but the morphology is identical. The damaging results in the formation of vacancies, interstitials, and vacancy clusters. The interstitials are annihilated at 473 K. Damage created by self-implantation at 20 K will be annealed under the conditions present in this work.

5.6.2 Retention

The goal of this investigation was to study the influence of radiation-induced defects on the D retention enhancement, as it is an important factor for future estimates of the tritium inventory in Iter. To account for this effect, the D retention in damaged and undamaged samples was compared. In undamaged W samples irradiated with 200 eV D ions or exposed to the low-energy, high-flux D plasma, the depth of D accumulation (several micrometers) is much larger than the deuterium implantation range (several

nanometers). Moreover, deuterium ions with energies less than $940\,\mathrm{eV}$ are not able to cause displacement damage in tungsten [54]. A review of hydrogen bubbles in metals by Condon and Schober [58] outlines a possible mechanism of void formation—the mechanism of near-surface plastic deformation caused by the deuterium supersaturation within the near-surface layer. During D ion irradiation or D plasma exposure, the D concentration in the implantation zone greatly exceeds the solubility limit and stresses the matrix lattice until plastic deformation – along with the formation of voids and vacancy clusters – occurs to alleviate these tensions [54, 58, 122]. This deformation is assumed to be responsible for the sudden increase in trapping sites for deuterium (vacancies, vacancy complexes, and macroscopic cavities) at depths of several micrometers and the concurrent accumulation of deuterium, both in the form of D_2 molecules and D atoms. The formation of deuterium-filled cavities and D retention are thought to be caused by a combination of stress-induced plastic deformation, D diffusivity, D trapping, and de-trapping processes. It should be pointed out that the stress-induced plasticity of tungsten appears at high concentrations of soluble hydrogen and increases with increasing temperature. For long-term irradiations, the diffusing D atoms recombine on the cavity surfaces, thus increasing the gas pressure inside these cavities. Near room temperature, as more deuterium is deposited, the cooperative fracture between the cavities suddenly becomes an easy way of relieving their excess pressure, thus initiating cracks and allowing internal gas release. At elevated temperatures, a high deuterium pressure inside the cavities leads to the extrusion of metal and the formation of blisters [135]. The presence of radiation-induced defects – vacancies and vacancy clusters – in self-implanted tungsten leads to a D retention enhancement by a factor of five to eight (calculated for the $0.2 - 0.7\,\mu\mathrm{m}$ region) in comparison with undamaged samples. Beyond the damaged zone, the D concentration in both types of targets is similar. At fixed dpa and D irradiation fluence, the enhancement factor is higher at an exposure temperature of $470\,\mathrm{K}$ (see Fig. 5.10). This is a result of the competition between D diffusion, de-trapping, and defect annealing. The D retention increase is also dependent on the dpa level and seems to saturate at around $0.4\,\mathrm{dpa}$, which agrees with the results published in Ref. [18]. The D concentration in the sub-surface region ($0.2 - 0.7\,\mu\mathrm{m}$) is fluence indifferent, and the trap concentration reaches a plateau at 1.6% for samples irradiated at $320/350\,\mathrm{K}$, and around 1.2% for $470\,\mathrm{K}$ irradiation.

5.6.3 Desorption from Defects

Two desorption peaks were observed in both the damaged and the undamaged samples. As previously mentioned, $T_\mathrm{D} < 450\,\mathrm{K}$ is associated with the desorption from natural

defects such as dislocations and grain boundaries which are present throughout the tungsten samples [48, 136]. The release peak ranging from $600 - 680\,\mathrm{K}$ (primary traps) is speculated to stem from D_2 agglomeration in the bubbles which were formed in the near-surface [22, 46], D trapping to impurities atoms, as well as from D detrapping from primary vacancy traps [15, 45, 56, 121] which are present in the entire material. Further, the presence of atomic D on the walls of the vacancy clusters is proof of D_2 being present in the cavity [137]. Self-implantation of W by heavy ions introduces two new kinds of trapping sites at $480 - 530\,\mathrm{K}$ and at $\sim 820\,\mathrm{K}$. The origin of the first is believed to be connected to desorption from the D_2V complex. These traps are considered to be secondary vacancy traps which started to be filled after all primary traps had been populated [137]. On the other hand, these traps appeared only in the damaged W. As reported by Matsui et al. [60] and Sakamoto et al. [61, 62], interstitial-type dislocation loops can be created in tungsten under D irradiation at energies above the threshold for displacement ($\sim 940\,\mathrm{eV}$). Here, the D irradiation energies are far below this value (i.e., 38 and $200\,\mathrm{eV}$). However, what both studies showed is that these dislocation loops require vacancy sites to be formed. After W self-implantation, there are plenty of available vacancies to serve as nucleation sites for interstitial-type dislocation loops to be formed during D irradiation. Therefore, it is likely that these defects are responsible for D de-trapping at temperatures ranging from 480 to $530\,\mathrm{K}$. The desorption temperature $\sim 820\,\mathrm{K}$ corresponds either to the accumulation of atomic D in VCs containing 11 to 16 vacancies [15] or to D decoration of the inner side of vacancy cluster walls. The arguments which speak for this choice and not for desorption from the voids are the recovery temperature of these defects which lies around $\sim 1200\,\mathrm{K}$ [11, 87, 97, 99, 132] – too low to anneal out voids – as well as the lack of void observation after tungsten self-implantation at RT [83, 124].

5.6.4 Blistering

The absence of blisters – and cracks – in the damage zone in batches A and B after exposure to the high-flux plasma is an additional confirmation of the high trap site density. In the presence of radiation-induced defects, the effective solubility of D is increased, and therefore, the stress due to the implanted D decreases and is not high enough for crack production, as would be the case for undamaged W. Once the stress level in the D implanted W leads to mechanical failure at local weak spots like grain boundaries, the D from the surrounding W bulk effuses into the crack until the D_2 pressure inside the crack equilibrates the chemical potentials of D in the bulk [12, 123, 138]. Due to the low solubility of D in W, this pressure can be strong enough to

further widen the crack or push grains out of the surface. The combination of high-flux D irradiation and excess vacancies appears to inhibit crack formation in the near-surface region and shifts the formation of cracks far beyond the implantation zone. The formation of these deep cracks may result in blister formation on the W surface. Since n-induced defects in W will be present in the entire material, this may suppress crack and blister formation. In addition, the extension of the damage zone may hold back blister formation or shift their creation to a higher D flux. The temperature of $800\,\mathrm{K}$ seems to be a good choice for Iter or DEMO operations. Here, all tritium should be de-trapped at this temperature, alleviating concerns about its retention. Additionally, vacancy clusters should still be present in the material which would hinder the blistering. On one hand, during continuous n irradiation at $800\,\mathrm{K}$, voids should be formed [132], but on the other hand, the presence of rhenium and osmium (due to transmutation) as impurity atoms would diminish the collection of vacancies and vacancy clusters in the void [100, 132].

Chapter 6

Carbon-Implanted Tungsten

In current nuclear fusion experiments, different materials are used for the divertor to protect it from the high heat flux. Tungsten is an increasingly popular choice due to its high threshold for physical sputtering, low hydrogen solubility, and high temperature strength. The presence of CFC at the vertical target strike points is motivated by its resilience to high heat fluxes and temperatures. During exposure to the plasma, not only are mixed W/C materials formed, but also, ion-induced defects are created by both fuel and PFC particles. To control the tritium inventory, the hydrogen isotopes' transport and trapping mechanisms must be well understood.

In this chapter, the D ion diffusion and inventory were investigated at room temperature in pure, carbon-, and self-implanted PCW. The combination of self- and C-pre-implantation allows to discriminate between chemical effects and damage-induced changes of the D retention.

$500\,\mu$m PCW, mirror-like polish, outgassed $1200\,$K, $2\,$h	
5.5 MeV **tungsten** implantation, RT 0.5 MeV **carbon** implantation, RT	
$(1-4){\times}10^{19}\,$W^{2+}/m^2 $(0.6-2.5){\times}10^{21}\,C^+$/m^2	
$11-50\,$dpa	
$200\,$eV/D$^+$ ion irradiation, $320\,$K	
$1{\times}10^{24}\,$D/m^2 and later $5{\times}10^{24}\,$D/m^2	

Table 6.1: Sequence of sample preparation.
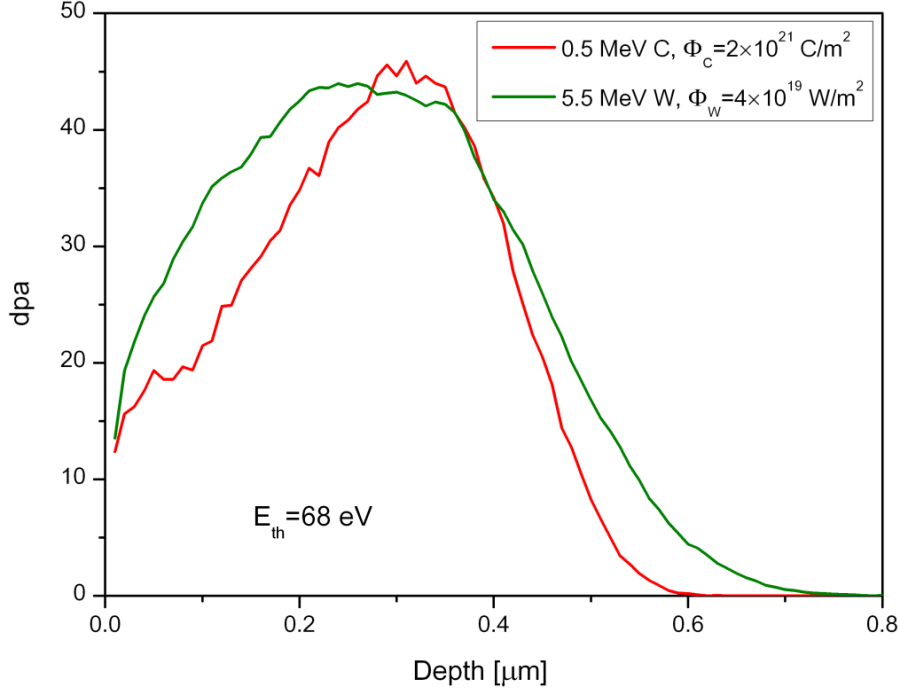
Figure 6.1: Damage distributions in W irradiated with $5.5\,\mathrm{MeV}$ W^{2+} (green line) and $0.5\,\mathrm{MeV}$ C^+ ions (red line) to a damage level of around $45\,\mathrm{dpa}$ ($E_\mathrm{th} = 68\,\mathrm{eV}$).

6.1   Samples

All samples were cut from a PCW plate ($0.5\,\mathrm{mm}$ thick and $99.95\,\mathrm{wt.\%}$ pure from Good-fellow Cambridge Limited), mechanically mirror-like polished and then outgassed at $1200\,\mathrm{K}$ for $2\,\mathrm{h}$ in vacuum at a background pressure of $2\times10^{-6}\,\mathrm{Pa}$. The such-prepared samples were carbon- or self-pre-implanted and then irradiated with D. The sequence of the experimental procedure is shown in Tab. 6.1. To provide reference values, D retention in pure tungsten was investigated.

Carbon pre-implantation and self-implantation makes it possible to create radiation defects and distinguish between damages and D-C-W chemistry. The energies and fluences were chosen in such a way that the damage depth profiles and dpa (at the peak) were similar for all samples (see Fig. 6.1).

For carbon implantation, $0.5\,\mathrm{MeV}$ $^{12}\mathrm{C}^+$ ions to a fluence of $(0.6-2.5)\times10^{21}\,\mathrm{C}^+/\mathrm{m}^2$ were employed (see Tab. 6.1). A typical value for the flux was $6\times10^{16}\,\mathrm{C}^+/(\mathrm{m}^2\mathrm{s})$. For the self-implantation, $5.5\,\mathrm{MeV}$ W^{2+} ions to a fluence of $(1-4)\times10^{19}\,\mathrm{W}^{2+}/\mathrm{m}^2$ and at a flux of $3\times10^{15}\,\mathrm{W}^{2+}/(\mathrm{m}^2\mathrm{s})$ were used. In both cases, the mean ion range was around $0.4\,\mu\mathrm{m}$.
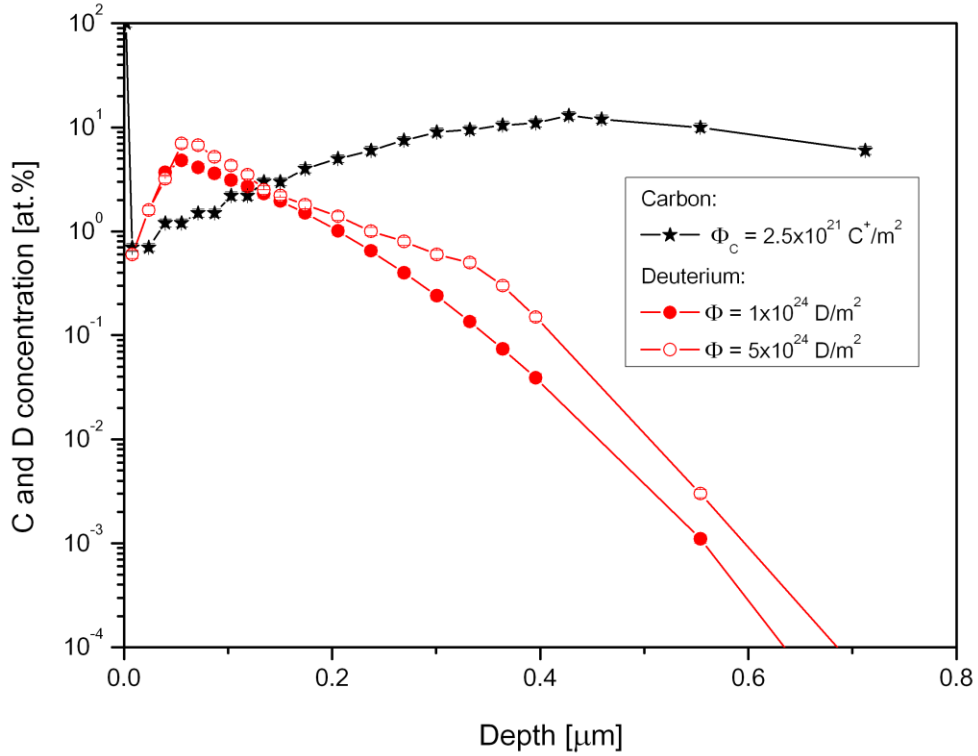
Figure 6.2: Carbon (black stars) and deuterium depth profiles (red circles) in tungsten pre-implanted with $0.5\,\mathrm{MeV}$ C ions up to a fluence of $2.5\times10^{21}\,\mathrm{C/m^2}$. D irradiation was performed with $200\,\mathrm{eV}$ D at RT to fluences of $1\times10^{24}\,\mathrm{D/m^2}$ and $5\times10^{24}\,\mathrm{D/m^2}$.

The use of such high implantation fluences led to high damage levels ranging from 11 to $50\,\mathrm{dpa}$. The such-prepared samples were irradiated at the HCS (see Sec. 4.2), first with $200\,\mathrm{eV}$ D ions at $320\,\mathrm{K}$ to a fluence of $1\times10^{24}\,\mathrm{D/m^2}$ and then – after NRA analysis – up to a fluence of $5\times10^{24}\,\mathrm{D/m^2}$. The D depth profiles and concentrations were measured after each D irradiation, and the total D retention was measured by means of TDS only after irradiation at the higher fluence.

6.2   Depth Profiles

The carbon depth profiles were measured up to a depth of $0.7\,\mu\mathrm{m}$. As in the SRIM simulations, the profile follows a Gaussian distribution with a maximum concentration of 13% at $0.42\,\mu\mathrm{m}$ (see Fig. 6.2). On all samples pre-implanted with C, a thin layer of graphite with a thickness up to $10\,\mathrm{nm}$ was detected.

The deuterium depth profiles in those samples have maximum concentrations of 4.8 and
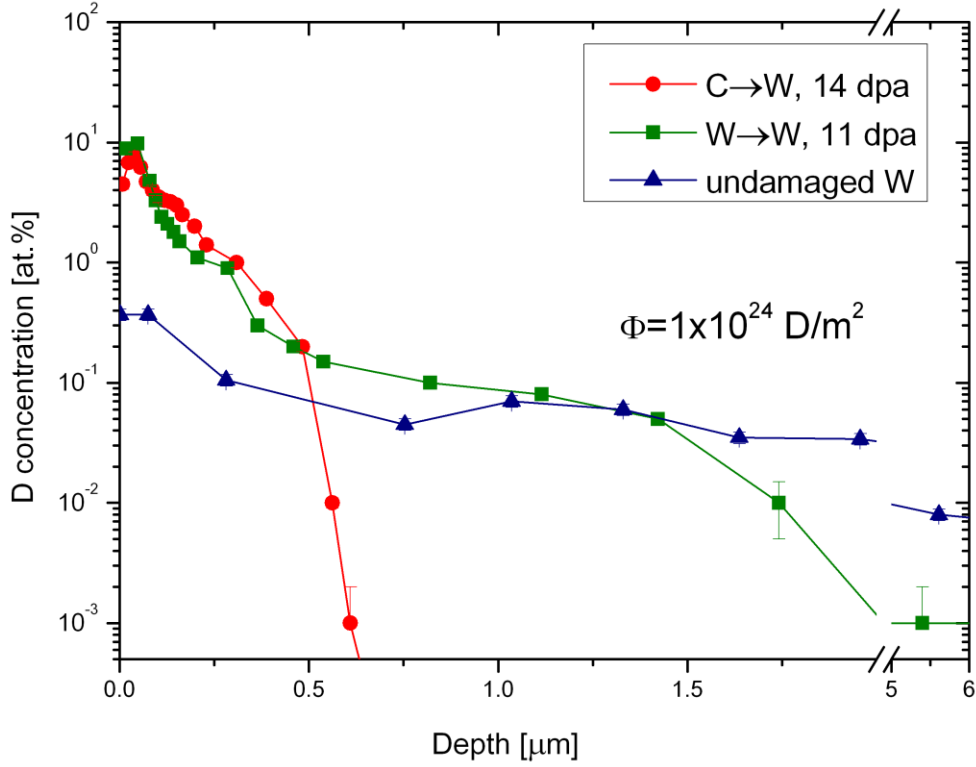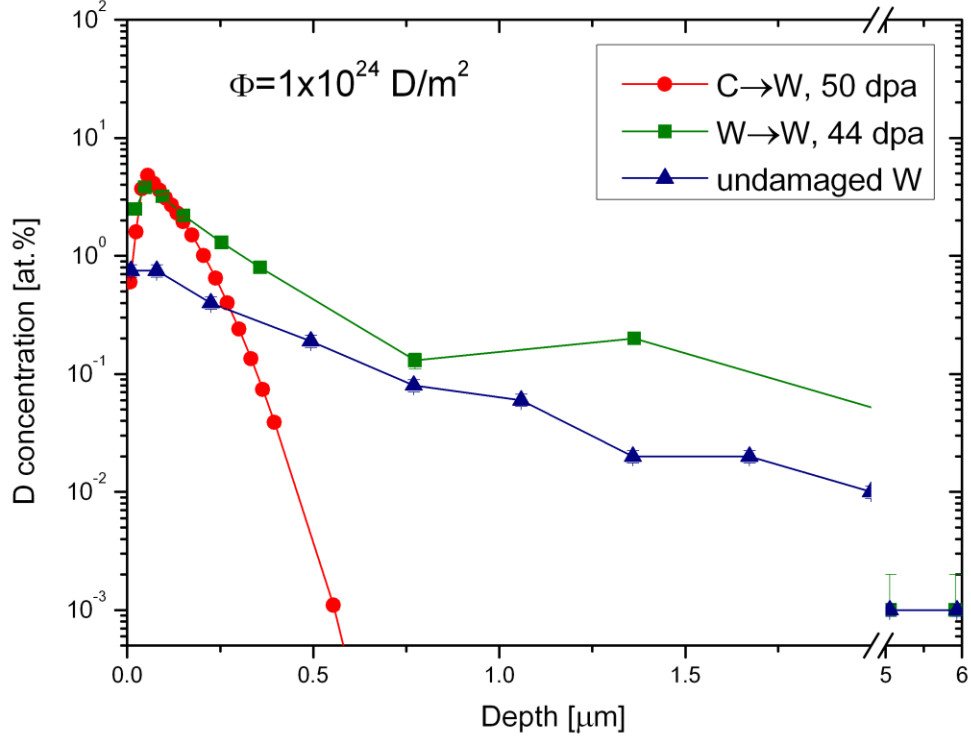
Figure 6.3: Deuterium depth profiles in undamaged tungsten and tungsten pre-implanted with W and C ions up to 11 and 14 dpa, respectively. D irradiation was performed at $200\,\mathrm{eV/D}$ at RT and to a fluence of $1\times10^{24}\,\mathrm{D/m^2}$.

$7\,\mathrm{at.\%}$ for the irradiation fluences $1\times10^{24}\,\mathrm{D/m^2}$ and $5\times10^{24}\,\mathrm{D/m^2}$, respectively. This maximum is located at around $0.1\,\mu\mathrm{m}$ beneath the surface. Then the concentration quickly decreases with depth, and above $\sim 0.7\,\mu\mathrm{m}$, it is below the detection level. Although the irradiation fluences differ by a factor of five, the measured D depth profiles almost overlap, suggesting fluence saturation.

In Figs. 6.3 and 6.4, D depth profiles and concentration in "weakly" damaged W $(11-14\,\mathrm{dpa})$ and in "highly" damaged W $(44-50\,\mathrm{dpa})$ after low-fluence D irradiation (i.e., $1\times10^{24}\,\mathrm{D/m^2}$) are plotted. Results from the undamaged samples are included for reference. In the undamaged target, the D concentration at the near-surface ranges from 0.4 to $1\,\mathrm{at.\%}$, depending on the irradiation fluence, and then decreases gradually with depth down to a level of $10^{-2}\,\mathrm{at.\%}$.

In the presence of ion-induced defects, the D concentration rises even up to $10\,\mathrm{at.\%}$, and its high level is independent of the type of damaging ions, which implies that the defect

Figure 6.4: Deuterium depth profiles in undamaged tungsten and tungsten pre-implanted with W and C ions up to 44 and 50 dpa, respectively. D irradiation was performed at $200\,\text{eV/D}$ at RT and to a fluence of $1\times10^{24}\,\text{D/m}^2$.

morphologies created by carbon and tungsten ions are similar. In the self-implanted specimens, D populates the available traps and then diffuses at least up to $6\,\mu\text{m}$ with a bulk concentration level similar to that for the undamaged samples. In the presence of carbon, no deep diffusion is observed, which suggests that carbon acts as a diffusion barrier for D.

D depth profiles obtained from self-implanted W damaged to $11-44\,\text{dpa}$ (as described in this chapter) and to $1.2\,\text{dpa}$ (see Ch. 5) and irradiated with $200\,\text{eV}$ D at $320\,\text{K}$ to similar fluences are compared in Fig. 6.5. Although the difference between the damage levels is more than one order of magnitude, the profiles practically overlap, suggesting saturation of the traps and the D irradiation fluence. In all cases, one can observe a high D concentration in the damaged region (up to $0.7\,\mu\text{m}$) and in the sub-surface ($0.7-1.5\,\mu\text{m}$), beyond which it gradually decreases with depth.

The retention results taken from the NRA measurements are collected in Fig. 6.6 as a function of the dpa. For comparison, the D retention level for low dpa ($1.2\,\text{dpa}$, see
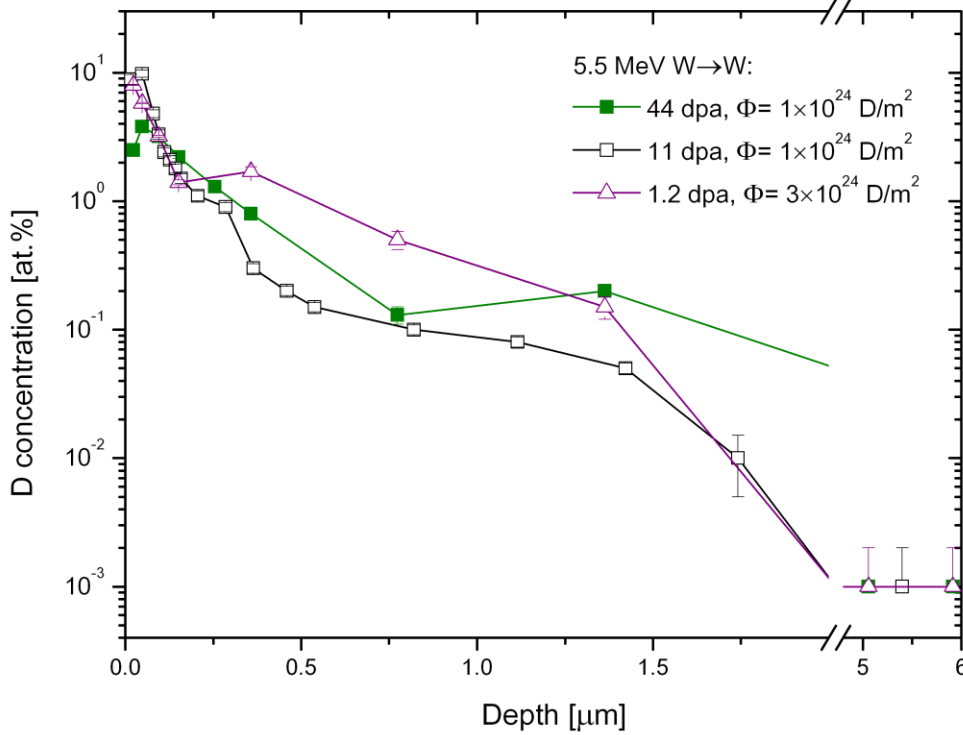
Figure 6.5: Deuterium depth profiles in self-implanted W damaged up to 1.2, 11 and 44 dpa. D irradiation was performed at 200 eV at RT to fluences of either $1{\times}10^{24}\,\mathrm{D/m^2}$ or $3{\times}10^{24}\,\mathrm{D/m^2}$.

Fig. 5.9: solid symbols) is marked by a dashed line. No significant fluence independence is observed. It seems that with increasing dpa, the D retention decreases. FIM observations of depleted zones [83, 133] can provide an explanation for this effect. At low irradiation doses, single ions create separate depleted zones; and when the fluence increases, these zones start to overlap, and the number of introduced defects approaches saturation. With further irradiation, the trap density drops [83].

6.3   TDS Spectra

Thermal desorption spectra for undamaged W samples and samples damaged with C and W ions up to 14 and 11 dpa, respectively, and irradiated with D ions to a fluence of $1\times10^{24}\,\mathrm{D/m^2}$ at 320 K are shown in Fig. 6.7. Multi-peak Gaussian fit parameters to these curves are presented in Tab. 6.2. The spectrum measured for the undamaged target (blue squares) reveals two peaks at $T_\mathrm{D} = 434\,\mathrm{K}$ and 550 K. This is similar to the
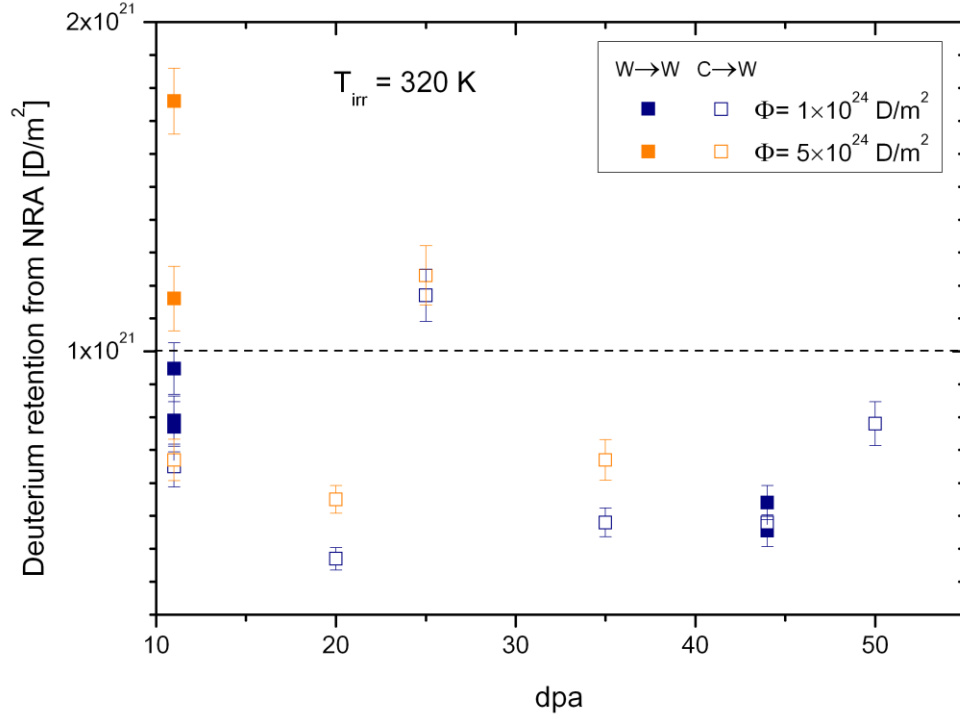
Figure 6.6: Deuterium retention up to $6\,\mu$m (taken from NRA) vs. the number of displacements for W pre-damaged either with $5.5\,$MeV W^{2+} (solid squares) or with $0.5\,$MeV C^+ (empty squares) to various damage levels, after irradiation with $200\,$eV D at $320\,$K to the ion fluences of $1{\times}10^{24}\,$D/m^2 (blue) or $5{\times}10^{24}\,$D/m^2 (orange). A dashed line indicates the retention level from Fig. 5.9 (for lower damage levels up to $1.2\,$dpa).

desorption temperatures T_D [K]	$200\,$eV D ions $\rightarrow$ W, $T_{\mathrm{irr}} = 320\,$K, $\Phi = 1{\times}10^{24}\,$D/m^2		
	carbon	tungsten	undamaged
Peak1	440	433	434
Peak2	490	472	—
Peak3	613	586	550
Peak4	820	826	—

Table 6.2: T_D obtained by fitting Gaussians to the raw data from Fig. 6.7.
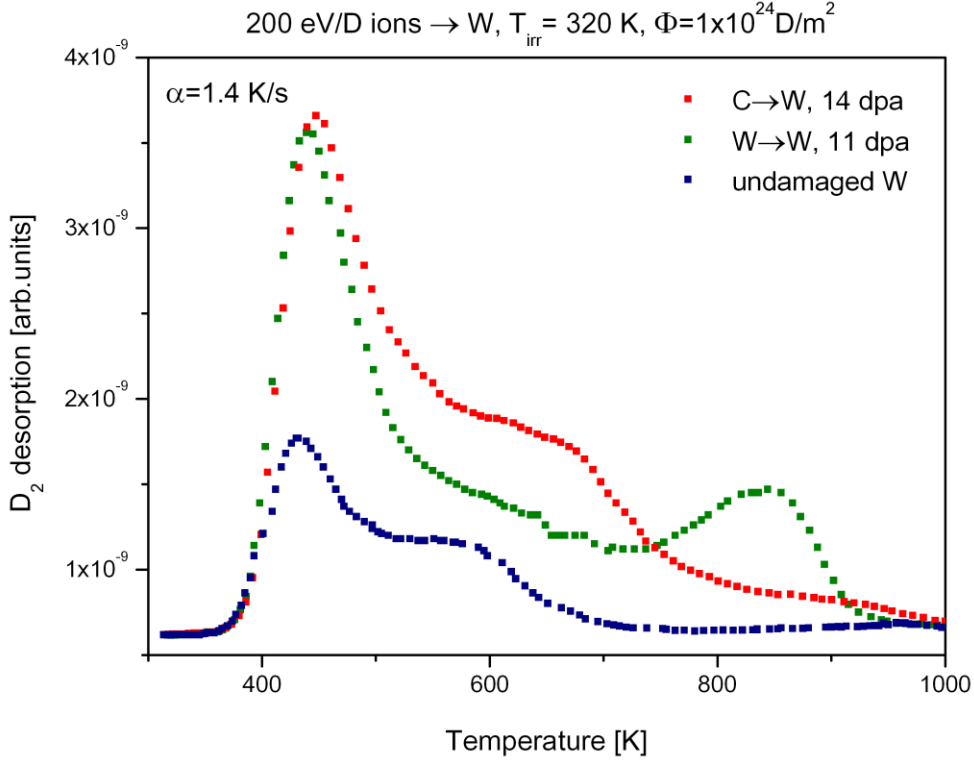
Figure 6.7: Experimental TDS spectra obtained from undamaged tungsten and tungsten pre-implanted with W and C ions up to 11 and 14 dpa, respectively. D irradiation was performed at 200 eV at RT to a fluence of 1×10^{24} D/m^2.

observations made previously in Ch. 5. A resemblance was also found to the damaged targets which display four peaks at < 450, $470 - 490$, $580 - 620$, and ~ 820 K (where, in the case of the C-pre-implanted samples, a long desorption tail rather than a distinct peak was observed). The origin of these peaks was already discussed in Sec. 5.6.3.

In Sec. 5.3.1, the saturation of high-energy traps was questioned, and a suggestion was made that this issue should be investigated at dpa levels higher than 1.2. In Fig. 6.8, TDS spectra obtained from tungsten samples damaged to higher levels of 11 and 44 dpa are shown. For reference, the TDS spectrum from the sample damaged to 1.2 dpa and irradiated to a fluence of 5×10^{23} D/m^2 at 350 K is plotted.

Indeed, it seems that at 1.2 dpa, high-energy trap formation does not reach saturation, and damaging at higher levels introduces more of these defects (with $T_D \sim 820$ K) which have a capacity to store more D. As previously discussed (see Sec. 6.2), at extremely high irradiation fluences, the number of the available traps drops which is also reflected in the TDS spectrum obtained from the sample damaged to 44 dpa where all peaks are
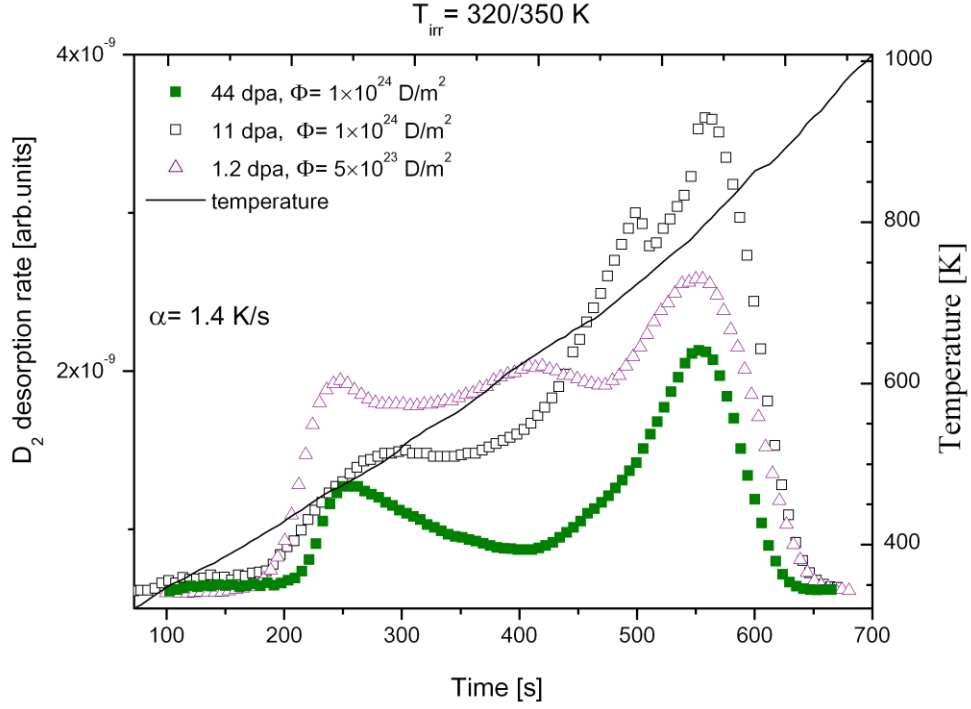
Figure 6.8: TDS spectra in self-implanted W damaged with W ions up to 1.2, 11, and 44 dpa. D irradiation was performed at 200 eV at RT to fluences of either 1×10^{24} D/m^2 or 5×10^{23} D/m^2.

much lower than for 1.2 dpa.

6.4 Discussion

There can be a number of explanations of D diffusion slowing down in the presence of carbon. Firstly, there is a hypothesis that C occupies the interstitial diffusion path which normally would be available to D. Since the D depth profiles in carbon and self-implanted W overlap in the region of $0 - 0.7\,\mu$m, and since the D concentration in this region is comparable for both kinds of damaging ions, this theory can be rejected. Another explanation assumes the surface recombination to increase [37], which leads to a low D concentration outside the implantation zone, and therefore to a lower number of diffusing particles. This can also be excluded, as – due to the presence of ion-induced defects – a large D concentration is observed in the target and there is a large D gradient between the near-surface region and the bulk. The third theory is that C trapped in the lattice bounds with adjacent W atoms and forms WC which has a lower

diffusion coefficient than pure W. The D diffusion coefficient in C is practically zero [139]; therefore, if some kind of tungsten carbon mixture is formed after C-pre-implantation, it may have a diffusion coefficient much lower than that of pure W. Unfortunately, there is no corresponding data available. However, a D retention and diffusion decrease has already been observed with the formation of tungsten carbide [51, 140–142]. According to Luthin and Linsmeier [143], who evaporated thin carbon films onto W substrate and then measured the development of the carbide with temperature, only 5% of WC is present at RT, and W_2C and WC formation starts at $770\,$K and $970\,$K, respectively. In the case of carbon implantation, this situation might look completely different, and a substantial fraction of WC might be present in the material. XRD measurements performed on carbon-implanted W revealed some (difficult to quantify) amount of W_2C and WC in the samples. Additionally, the surface of the samples which contained carbon showed no blistering, whereas pure W samples irradiated at the same D fluence did. As already mentioned in Sec. 2.5, this can also be sign of the presence of WC. Molecular D_2 and CD_4 desorption spectra obtained from samples containing WC revealed a desorption peak in the temperature range of $870 - 1200\,$K [141, 144, 145] which can be assigned to D bound to C. In all C-pre-implanted samples, a desorption tail ranging from $800\,$K to $1000\,$K was observed, but the possibility cannot be excluded that part of the desorbed D came from the ion-induced defects and not from D bound to C. Additionally, all carbon-containing samples had exhibited a desorption peak at around $1000\,$K in the CD_4 (mass 20) spectra, a peak which was registered in samples not damaged with C (mass 20 can also be assigned to heavy water molecules (D_2O)). Therefore, it is impossible to decide whether the observed peak at $1000\,$K corresponds to D bounded to C.

In Iter, C energies will be much lower than those used here, and therefore, the carbon-implanted zone will be shorter. Instead, at elevated temperatures (see Tab. 1.1), C may diffuse to the bulk and form carbides which would hold back the D diffusion.

Chapter 7

Deuterium Diffusion Rate

In the previous chapters, it has been demonstrated that the presence of radiation-induced defects in W will lead to an enhancement of the D retention by a factor five to eight (in the damaged region ranging from $0.2 - 0.7\,\mu$m) in comparison with undamaged tungsten. On the other hand, trapping will hinder D diffusion and therefore reduce the depth to which higher D retention will expand. Thus, the question remains if during Iter's operation time, D will be capable of filling all volumetrically distributed traps present in the tungsten wall. To answer that, trapping of permeating deuterium in defects induced in the rear side of PCW samples was studied in order to help estimate the rate at which D is diffusing to the traps. The back side of the samples was damaged by W ions, and then the front side was exposed to a D plasma at elevated temperatures. Depth profiles of deuterium trapped in the W samples have been measured on both sides up to a depth of $6\,\mu$m by means of NRA.

7.1 Samples

A $500\,\mu$m thick polycrystalline, mechanically mirror-like polished W plate (see Sec. 5.1) and a $25\,\mu$m thick PCW foil (both 99.95 wt.% pure from Goodfellow Cambridge Limited) were cut into pieces of $10 \times 10\,\text{mm}^2$ size. The thick targets were outgassed at $1200\,\text{K}$ for $2\,\text{h}$. No outgassing was performed on the W foils.

Two experiments were performed independently. In the first one, the rear side of the samples was implanted with $5.5\,\text{MeV}$ W^{2+} ions with a projected range $R_\text{p} = 0.4\,\mu$m (damage zone $0.7\,\mu$m) at an ion flux of $5 \times 10^{14}\,\text{W}^{2+}/(\text{m}^2\text{s})$ and to a fluence of $3.5 \times 10^{17}\,\text{W}^{2+}/\text{m}^2$, which corresponds to a damage level of $0.4\,\text{dpa}$ at the maximum of the damage profile. Hereafter, this damage zone will be referred to as A. The front side was exposed to D plasma (see Tab. 7.1). A second type of implantation with $20.2\,\text{MeV}$

sample	thickness [μm]	W irradiation	plasma exposure		
			energy [eV]	fluence [D/m^2]	temperature [K]
R2	25	A	38	3×10^{26}	540
R1	500	A	68	3×10^{26}	605
R3	500	undamaged	68		605

Table 7.1: Sequence of sample preparation in the first experiment. *A* refers to the type of the damage zone as explained in the text.

sample	thickness [μm]	W irradiation	plasma exposure		
			energy [eV]	fluence [D/m^2]	temperature [K]
F0	25	undamaged	48	3×10^{26}	545
F3	25	B	48	3×10^{26}	460
F4	25	B	48	3×10^{26}	550
F6	25	B	48	3×10^{26}	650
F7	25	B	48	3×10^{26}	755
F2	25	B	D$_2$ gas exposure at $T_{\mathrm{irr}} = 550\,$K for $8\,$h$\,20\,$min (the same time as for fluence $3 \times 10^{26}\,$D/m^2)		

Table 7.2: Sequence of sample preparation in the second experiment. *B* refers to the type of the damage zone as explained in the text.

W^{6+} ions with a projected range $R_{\mathrm{p}} = 1.5\,\mu$m (damage zone $2.2\,\mu$m) was done, again on the rear side of the targets, at an ion flux of $1 \times 10^{14}\,$W^{6+}/(m^{2}s) and to a fluence of $4 \times 10^{17}\,$W^{6+}/m^2, which corresponds to a damage level of $0.34\,$dpa at the maximum of the damage profile. This damage zone is labeled B. The front side of these specimens was exposed to a low-energy, high-flux deuterium plasma to a fluence of $3 \times 10^{26}\,$D/m^2 at elevated temperatures ($460 - 755\,$K) in the Linear Plasma Generator at JAEA [107] (see Tab. 7.2). D$_2$ gas exposure was investigated on one self-implanted sample (see Sec. 4.3).

Damaging up to $\sim 0.4\,$dpa is not only sufficient for simulating Iter-like conditions, but also, further damaging is not advantageous because above $0.4\,$dpa, trap density saturation takes place (see Sec. 5.4.1). The damage profiles calculated for both W ion energies at $E_{\mathrm{th}} = 68\,$eV arw shown in Fig. 7.1. Additionally, one $25\,\mu$m (sample F0)
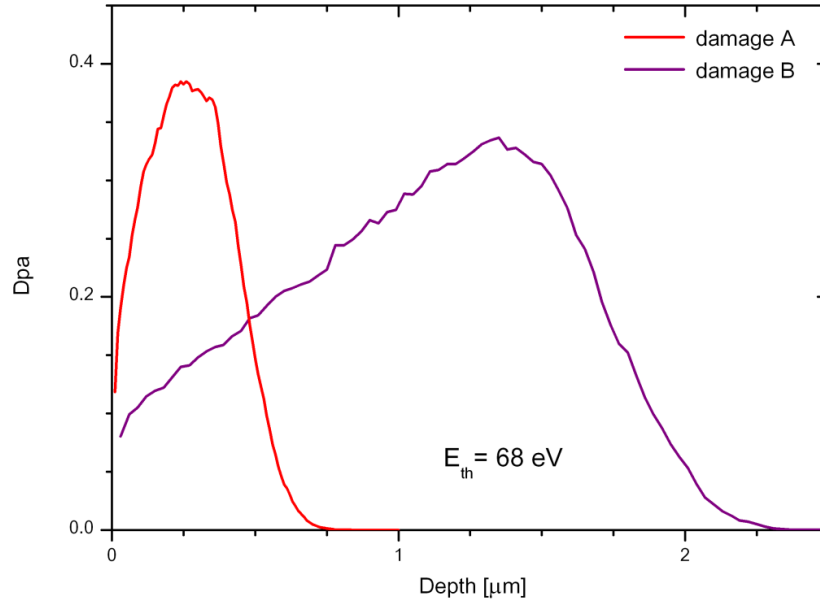
Figure 7.1: Damage distributions in W irradiated with $5.5\,\mathrm{MeV}$ W^{2+} (red) and $20.2\,\mathrm{MeV}$ W^{6+} ions (purple) to damage levels of 0.4 and 0.34 dpa, respectively ($E_{\mathrm{th}} = 68\,\mathrm{eV}$). A and B refer to the different damage zones as explained in the text.

and one $500\,\mu\mathrm{m}$ (sample R3 target were left undamaged and exposed to D plasma at 545 and $605\,\mathrm{K}$, respectively. This means that the mean depth $\bar{x} = (6D\tau)^{1/2}$ (where D is the diffusion rate taken from Frauenfelder [30] and $\tau = 3 \times 10^4\,\mathrm{s}$ is the exposure time) of diffusing deuterium after plasma exposure should be larger than the specimen thickness and equals 4.1 and $6.5\,\mathrm{mm}$ at exposure temperatures of 545 and $605\,\mathrm{K}$, respectively. The such-prepared samples were analyzed on both sides by means of NRA according to the method described in Sec. 4.5.2. For most samples, an analyzing charge of $5\,\mu\mathrm{C}$ was accumulated, but for the targets with low D concentration, the total charge was increased in order to obtain better statistics.

7.2 Front Side

Fig. 7.2 shows D depth profiles measured on the front side of these samples which were exposed to D plasma to a fluence of $3 \times 10^{26}\,\mathrm{D/m^2}$ at different temperatures and comparable energies. It is clear that the D concentration decreases with the irradiation temperature. The near-surface region of the samples irradiated at up to $\sim 600\,\mathrm{K}$ is characterized by a sharp D concentration peak and a quick subsequent drop with depth.
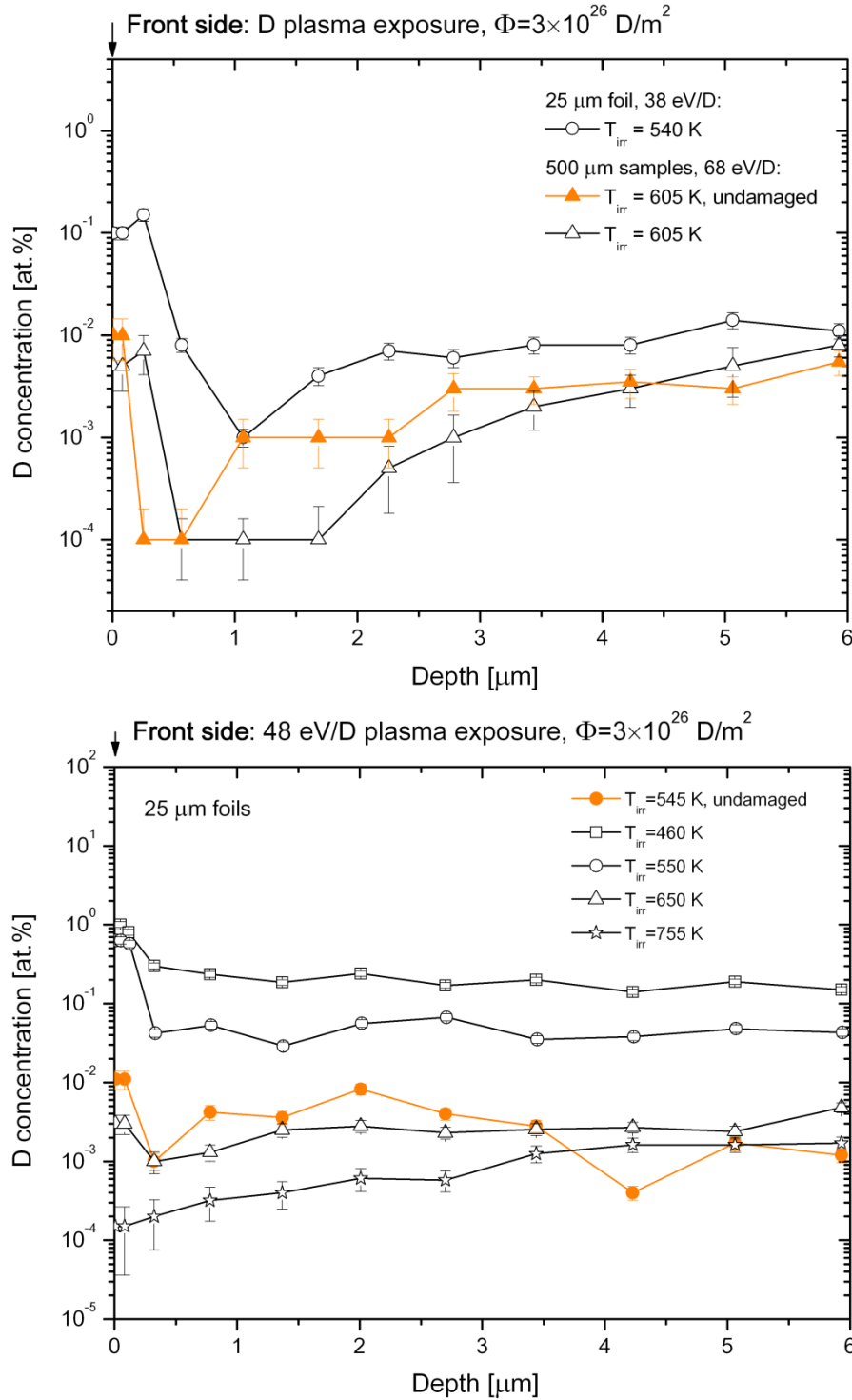
Figure 7.2: Deuterium depth profiles measured on the front side of the specimens which had been exposed to D plasma to a fluence of $3 \times 10^{26}\,\mathrm{D/m^2}$. The D concentration vs. the depth is shown for (a) the first experiment: $25\,\mu\mathrm{m}$ and $500\,\mu\mathrm{m}$ thick samples after exposure to D plasma at $T_{\mathrm{irr}} = 540$ and $605\,\mathrm{K}$, respectively; and (b) the second experiment: $25\,\mu\mathrm{m}$ thick samples after exposure to D plasma at T_{irr} from 460 to $755\,\mathrm{K}$.

In all cases, the bulk concentration remains more or less constant. At $460\,\mathrm{K}$ – in the second experiment – its level turns out to be $0.2\,\mathrm{at.\%}$ which, surprisingly, is two orders of magnitude higher than in the W samples with no damage history on the rear side which were exposed to $38\,\mathrm{eV/D}$ to a fluence of $1 \times 10^{26}\,\mathrm{D/m^2}$ at a similar temperature (see Sec. 5.2).

The same behavior is observed for samples irradiated at around $550\,\mathrm{K}$. For the sample with no damage on the back side, the bulk concentration is $\sim 10^{-3}\,\mathrm{at.\%}$ (see Fig. 7.2b, orange circles), for the sample with a smaller damage region (A) it is almost one order of magnitude higher (see Fig. 7.2a, empty circles), and the target with damage B has a bulk D concentration of $\sim 0.04\,\mathrm{at.\%}$ (see Fig. 7.2b, empty circles). Such trends are not observed for the thick samples irradiated at $605\,\mathrm{K}$ (see Fig. 7.2b). This hints at the possibility that irradiation with W ions of the rear side of a sample generates not only ion-induced defects but also stresses the matrix lattice until plastic deformation occurs to alleviate these tensions [54, 58, 122]. This deformation is assumed to be responsible for the generation vacancies, vacancy complexes, and dislocation loops [133] in the region beyond the defected zone. It should be noted that at these depths (up to several micrometers), the concentration of vacancy-type defects is significantly lower than the vacancy concentration in the damage zone. Such an explanation would provide a rationale for the increase of the bulk D concentration with growing damage in the $25\,\mu\mathrm{m}$ foils and the lack of these observations in the $500\,\mu\mathrm{m}$ targets.

7.3 Rear Side

In the first experiment, no deuterium was detected on the rear side of the $500\,\mu\mathrm{m}$ thick undamaged sample, not even at a level of $5 \times 10^{-4}\,\mathrm{at.\%}$ which is seen in the damaged samples. As already mentioned, the temperature of $605\,\mathrm{K}$ should be sufficiently high for D to permeate through the $500\,\mu\mathrm{m}$ sample, but apparently, it is already too high for effective D trapping in intrinsic defects. In the 20 times thinner undamaged foil irradiated at $540\,\mathrm{K}$ (see Fig. 7.3b), only a small amount of D was observed. A very low D concentration level of $10^{-4}\,\mathrm{at.\%}$ indicates that D cannot be trapped in grain boundaries at this temperature.

In the case of the damaged samples, the results show that the D depth profiles follow the calculated damage profile (see Figs. 7.3 and 7.4). Therefore, atomic D which permeated through the whole width of the material must be trapped in radiation-induced defects like vacancies and vacancy clusters. From Fig. 7.2b, one can see that the D concentration at $605\,\mathrm{K}$ and $755\,\mathrm{K}$ is lower than in the undamaged samples exposed at $545\,\mathrm{K}$. Due to
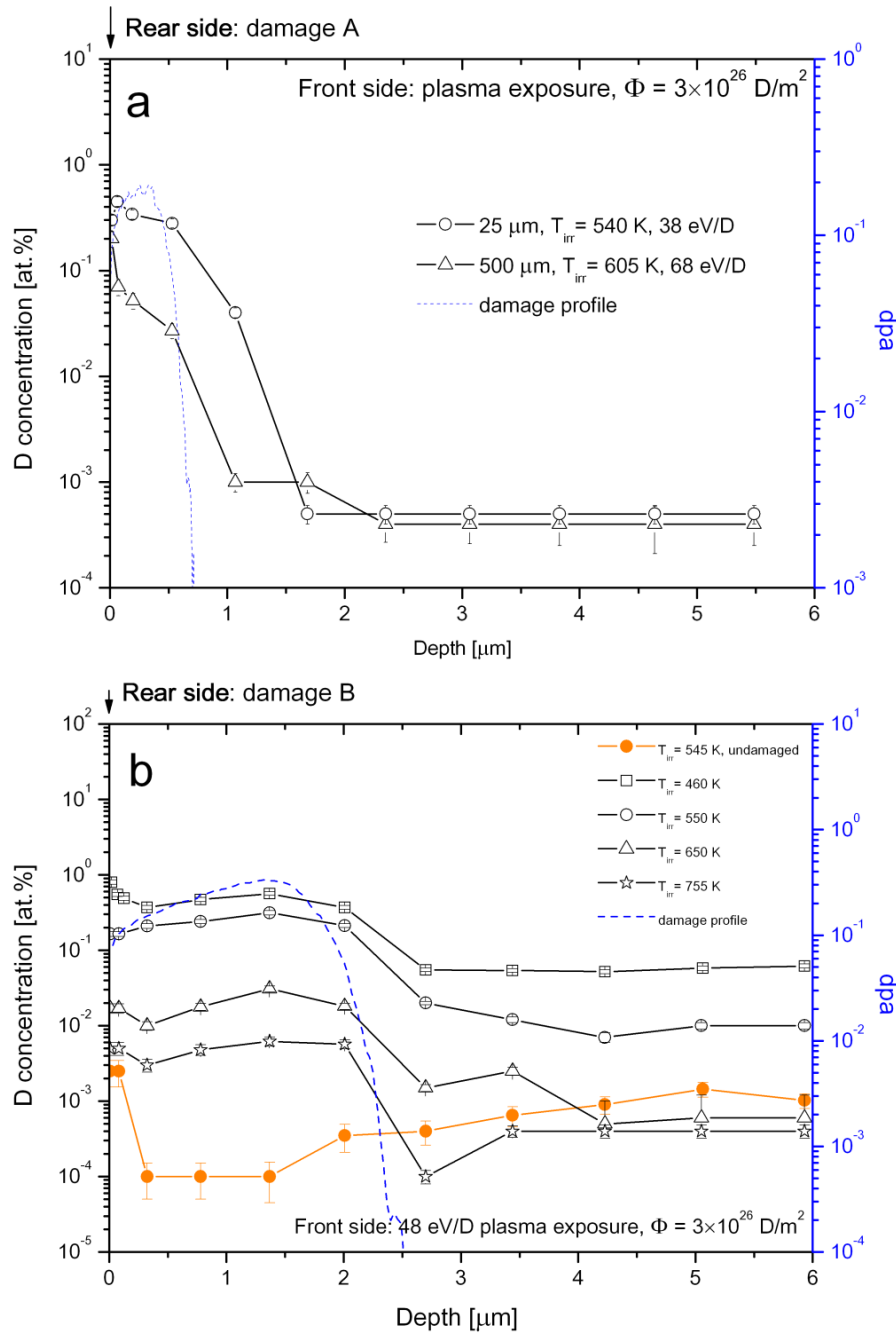
Figure 7.3: Deuterium depth profiles measured on the (damaged) rear side. The front side of the specimens was exposed to D plasma to a fluence of $3 \times 10^{26} \, \text{D/m}^2$. The D concentration vs. the depth is shown for (a) the first experiment: $25 \, \mu\text{m}$ and $500 \, \mu\text{m}$ thick samples after exposure to D plasma at $T_{\text{irr}} = 540$ and $605 \, \text{K}$, respectively; and (b) the second experiment: $25 \, \mu\text{m}$ thick samples after exposure to D plasma at T_{irr} from 460 to $755 \, \text{K}$. The damage profile is shown as a by blue dashed line in both plots.

exposure temperature [K]	D concentration [at.%] at the damage peak	type of damage zone	thickness [μm]
460	0.57	B	25
540	0.34	A	25
550	0.32	B	25
605	0.05	A	500
650	0.03	B	25
755	0.006	B	25

Table 7.3: D concentration measured at the peak of damage zones A and B at various exposure temperatures.

the presence of ion-induced defects, the picture is reversed in Fig. 7.3b. D retention is enhanced not only in the damage zone but also beyond it, resulting in long permeation tails with higher concentration levels than in the undamaged sample (at similar exposure temperatures). This was already discussed in Sec. 7.2 and argued to be a result of plastic deformation at depths beyond the damage zone caused by stress which was introduced by the self-implantation.

Deuterium trapping in the defects present on the rear side of the material strongly depends on the irradiation temperature. On one hand, a low irradiation temperature does not allow for fast permeation; but on the other hand, when the temperature increases, D is bound to the traps less effectively; and additionally, some of the defects introduced in the material anneal out—therefore, the number of trapping sites is reduced. To look for the temperature where the D concentration is highest, the D concentration at the damage peaks – i.e., at $0.4\,\mu$m and $1.5\,\mu$m (see Tab. 7.3) – and the D retention in the rear side (see Fig. 7.7) were compared as a function of the exposure temperature.

The highest measured value for the D concentration at the damage peak lies at $460\,$K, from where the concentration decreases with the exposure temperature. From Fig. 5.11, it seems that only half of the available traps are populated at $460\,$K—or, which is the more likely alternative, a synergetic effect between the D plasma and the defects led to additional trap creation. Such an effect is not observed in the rear side, which suggests that the D retention in "pure" traps was measured there. One can argue that the lower D concentration in the defects introduced in the back side stems from the smaller D diffusive flux to the traps in comparison with the D flux in the front side. Since the back side D concentration obtained from the samples irradiated at similar T_{irr} is comparable for the thin foil and for the thick target (see Tab. 7.3), this hypothesis can be excluded.
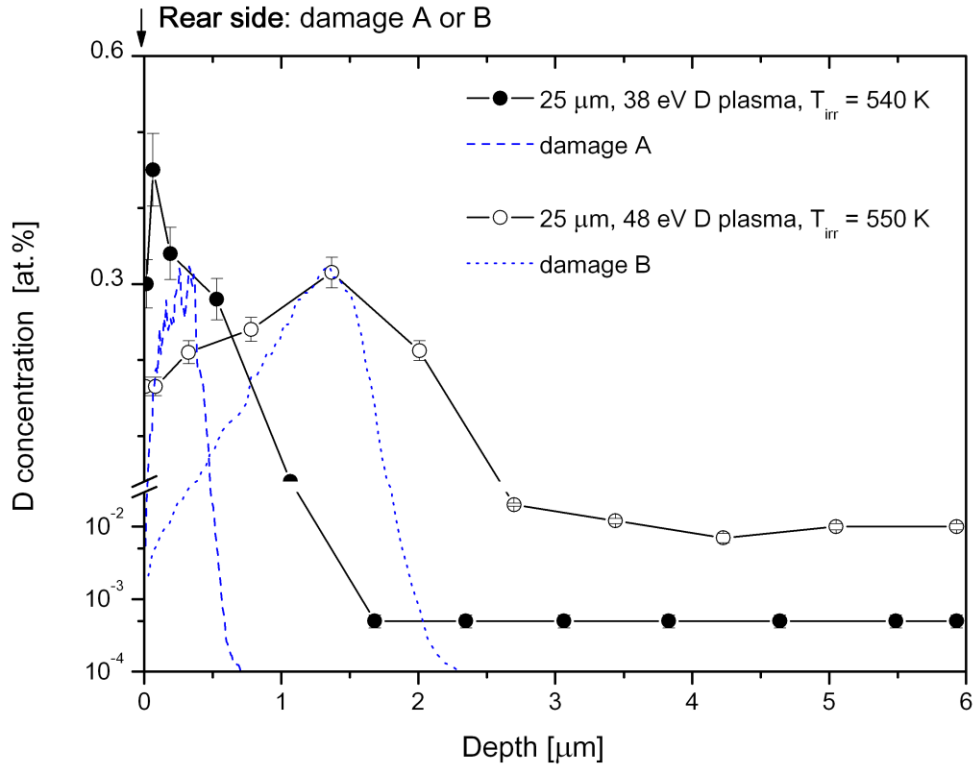
Figure 7.4: Deuterium depth profiles measured on the rear side, damaged either by 5.5 MeV W^{2+} ions up to 0.4 dpa (blue dashed line) or by 20.2 MeV W^{6+} ions up to 0.34 dpa (blue dotted line). The front side was exposed to D plasma to a fluence of 3×10^{26} D/m^2 and temperatures of $540 - 550$ K.

Moreover, the D concentration in the damage peak is comparable for samples irradiated at similar temperatures, of 540 K (A) and 550 K (B), and it appears to be independent of the damage profile (see Tab. 7.3 and Fig. 7.4). This observation indicates that the D diffusive flux is sufficient to populate all traps introduced into the rear side of the samples.

7.4   The Effect of D$_2$ Exposure

As already mentioned, there is a possibility that D trapped in defects which were introduced at the rear side of the material originated not from permeation but from D$_2$ gas exposure. To test that hypothesis, one damaged W sample was exposed to D$_2$ gas, and the D depth profile was measured subsequently (see Fig. 7.5).
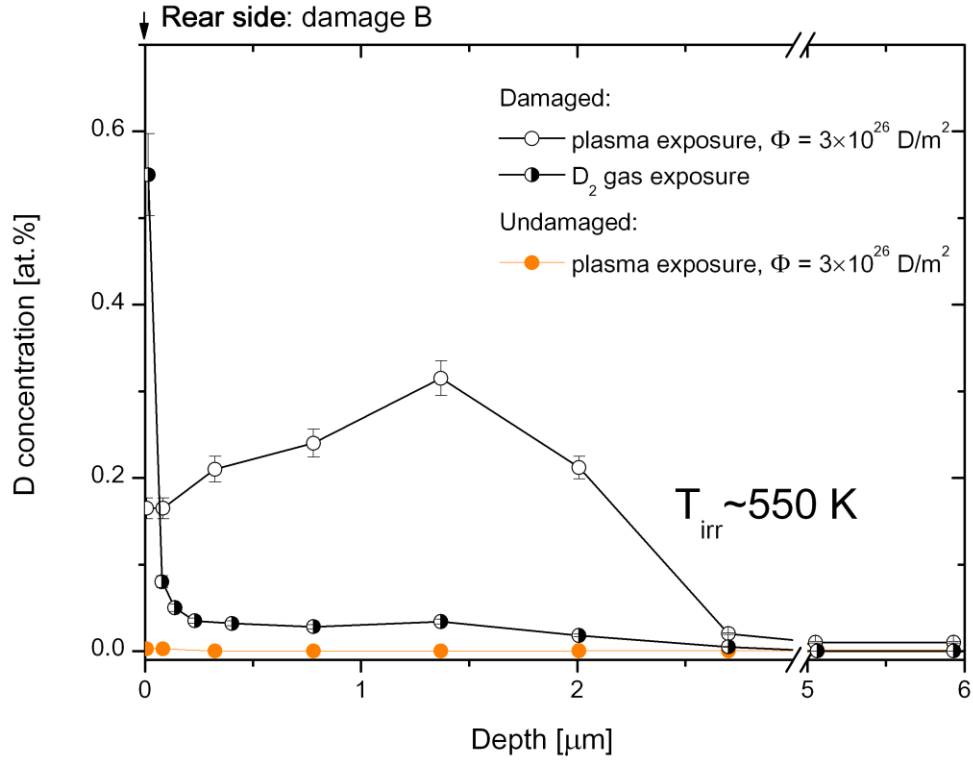
Figure 7.5: Deuterium depth profiles measured on the rear side of the samples exposed to D plasma at around 550 K. The data was obtained from the undamaged and pre-damaged samples directly irradiated with D plasma and from damaged W exposed to D$_2$ gas.

Some gas is indeed found to enter the material. Its depth profile is characterized by a sharp near-surface (80 nm) concentration of 0.55 at.%, and then it quickly decreases to a level of 0.034 at.% in the damaged zone and to a level of 10^{-4} at.% in the bulk. Generally, however, the total contribution from the gas exposure is very small in comparison with the depth profile measured on the damaged sample whose front side was directly exposed to the D plasma. One phenomenon which requires explaining is the occurrence of a sharp near-surface concentration peak in the gas-exposed target and its absence in the directly D-plasma-exposed specimen. If the depth profile measured on the latter sample results from both gas exposure and permeated D, such a concentration peak should be expected. However, the intensity of the near-surface concentration depends strongly on the purity of the surface. Another possible explanation for its absence is an exposure temperature fluctuation which could be as large as the temperature measurement error of $\pm$20 K. This effect should be investigated more closely on the samples exposed to the
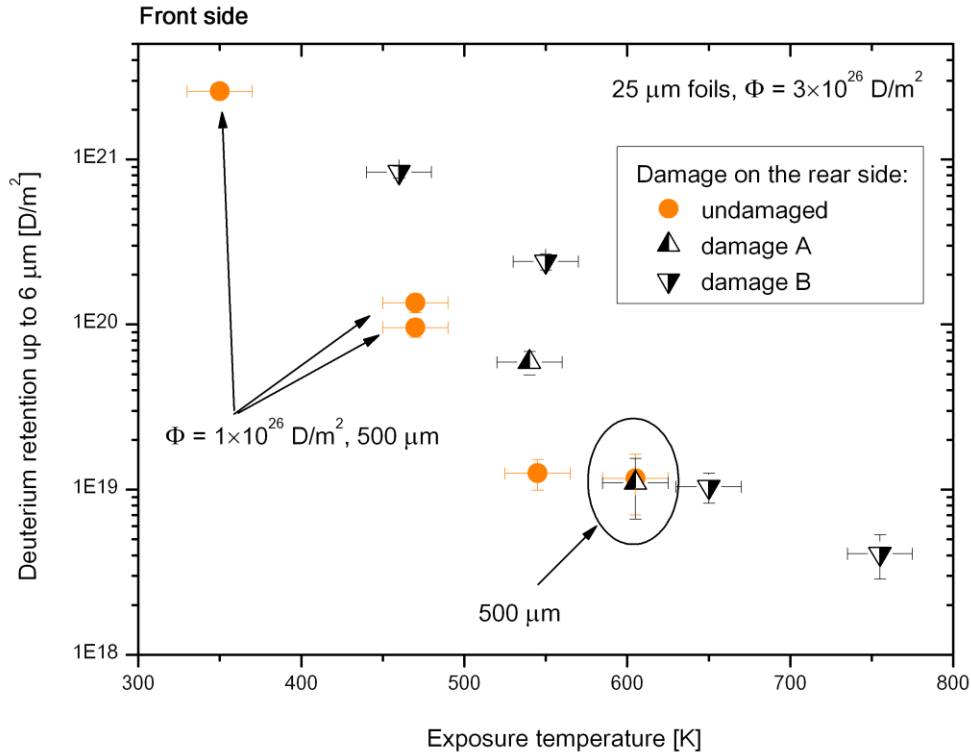
Figure 7.6: Deuterium retention up to $6\,\mu$m (taken from NRA) in the front side of undamaged and damaged PCW samples exposed to D plasma at different energies $(38 - 68\,\text{eV/D})$ to either a fluence of $1\times10^{26}\,\text{D/m}^2$ or $3\times10^{26}\,\text{D/m}^2$, as a function of the exposure temperature.

D_2 gas at other temperatures.

In the undamaged sample, the D concentration (from gas exposure or from permeated D) is very low, suggesting a lack of trapping. This means that the ion-induced defects must, by some mechanism, probably by lowering the absorption potential, cause D_2 gas to enter the material. The reason for that is not clear yet, and the matter requires further investigation.

7.5   Deuterium Retention

The deuterium retention in the front side was taken from NRA measurements as a function of the exposure temperature and is shown in Fig. 7.6. Additionally, some data is included which was already presented in Sec. 5.4 and which was obtained from undamaged PCW samples exposed to D plasma to a fluence of $1\times10^{26}\,\text{D/m}^2$ at $350\,\text{K}$
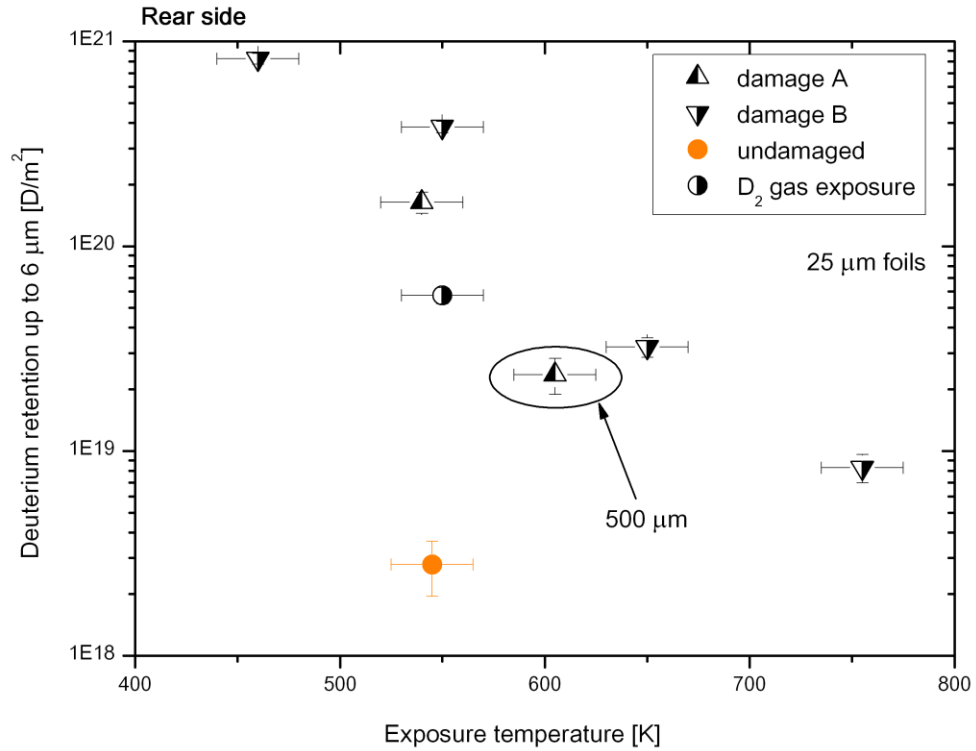
Figure 7.7: Deuterium retention up to $6\,\mu$m (taken from NRA) vs. exposure temperature in the rear side of the undamaged and pre-damaged PCWs after irradiation with D plasma.

and $470\,$K. In the W sample exposed to D plasma at $350\,$K, the D retention lies around $2\times10^{21}\,$D/m^2. As the temperature increases, the D retention decreases to a level of $4\times10^{18}\,$D/m^2 because at elevated temperatures, D trapping is less effective.

From Fig. 7.6, it is even clearer that due to the damaging of the rear side, new defects are present not only in the damage zone but also far beyond it. In the thin specimens, they influence D retention near the plasma-exposed surface. At similar temperatures, D retention is higher in the $25\,\mu$m foils with the damage zone on the rear side. This is not observed in the case of the $500\,\mu$m samples which are too thick for the D concentration on the front side to be influenced by the defects introduced by stress-induced plastic deformation on the back side.

Deuterium retention in the rear side taken from NRA measurements as a function of the exposure temperature is shown in Fig. 7.7. Both experiments confirm the D concentration reduction with increasing exposure temperature which had been observed in the front sides. Naturally, due to the smaller damage region, the D retention obtained
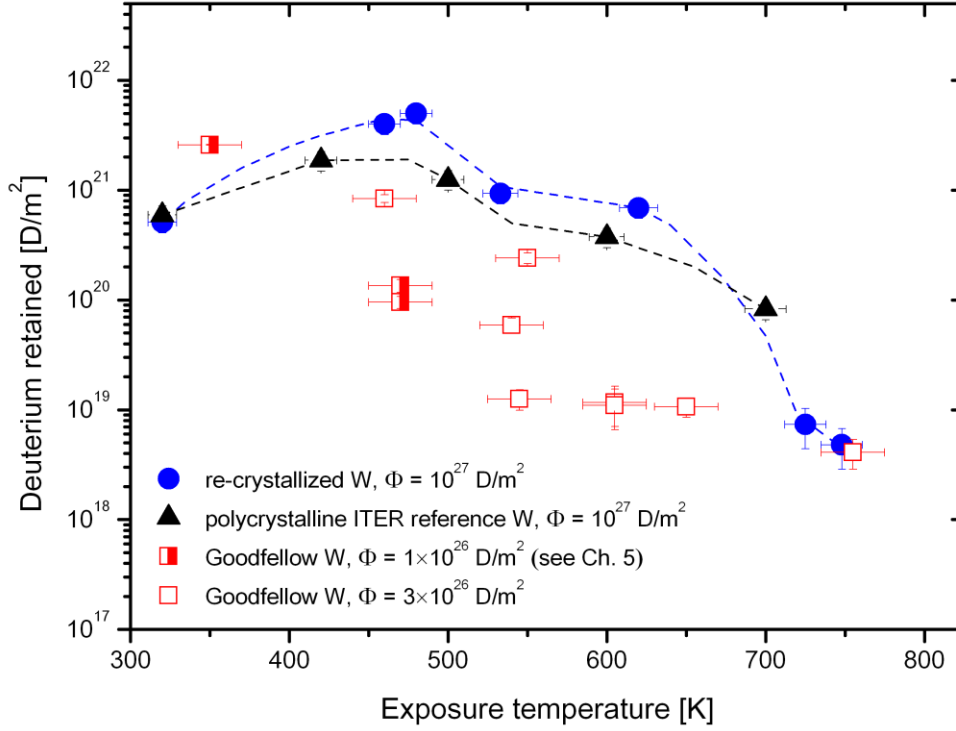
Figure 7.8: Deuterium retention up to $6\,\mu$m (taken from NRA) in re-crystallized W and Iter-grade W exposed to an ion fluence of $10^{27}\,$D/m^2, as well as PCW exposed to fluences of $(1-3)\times 10^{26}\,$D/m^2, as a function of the exposure temperature.

for the first experiment is smaller than in the second. This could not be noticed when comparing D concentrations in the damage peak. At $550\,$K, the deuterium retention in the damaged sample directly exposed to D plasma is two orders of magnitude higher than in the undamaged W and around seven times higher than in the damaged sample exposed to D$_2$ gas. D$_2$ gas exposure at different irradiation temperatures was not yet investigated, but one can assume similar relative contributions in the case of other temperatures.

7.6   Discussion

7.6.1   Retention

The retention of deuterium up to $6\,\mu$m in W depends on the exposure temperature. The maximum retention was observed at $350\,$K, after which point, retention decreased with increasing temperature. This tendency, as well as the retention in the first $6\,\mu$m, differs

from the findings by Alimov et al. [55] who exposed re-crystallized W and Iter-grade W to a fluence ten times higher than in the present case and observed a retention peak at 480 K (see Fig. 7.8). The D retention measured by Alimov et al. at 330 and 750 K is comparable with the values obtained in this work; but at other exposure temperatures, there are inconsistencies between the results. Since the irradiation fluences are far above the fluence required for saturation of D in W [146], this should have no influence on the total D retention.

Therefore, it must be the structure of the material which influences the D retention to such a degree. Grains in the hot-rolled Goodfellow tungsten are elongated parallelly to the surface and are less than $1\,\mu$m in size in the perpendicular direction, whereas in other W materials, grains are either large (up to $200\,\mu$m in the re-crystallized W) or elongated (to a distance of several μm) perpendicularly to the surface (Iter-grade W). For the Goodfellow W, stress field caused by D super-saturation in the near-surface layer [54, 58, 122] loses its intensity propagating into neighboring grains. Therefore, the probability of the formation of vacancy-type defects at depths of several micrometers is significantly lower than for re-crystallized and Iter-grade W where the stress field can extend to a large depth without a loss of density.

The results presented in this chapter are not in agreement with those obtained by Wampler and Doerner [16, 147]. In order to be able to correctly predict the influence of radiation-induced damage on tritium retention, the reason for this discrepancy must be investigated. Fig. 7.9 shows a schematic picture of the results and the experimental input parameters in both the present work and that of Wampler et al. There are a number of reasons for the apparent disagreement which can be classified as being related to the material, the damaging, and the D plasma exposure.

Different materials have different densities of intrinsic defects, therefore the amount of deuterium which reaches the rear site of the sample may not be identical. It is very unlikely that the number of natural defects in Plansee material is large enough to influence the entire process of D diffusion very strongly. Thickness and outgassing in both experiments are comparable and should thus not play any role.

There may be some chemical effects involved in damaging W with silicon ions, in particular: during plasma irradiation at elevated temperatures, some silicides may be formed [148], and D permeation to the defects may be hindered. Additionally, different ions may create different kinds of defects, but in this case, the damage morphology should be comparable. The lower damage levels in Wampler's samples can contribute to the deviating results, but at 0.6 dpa ($E_{\mathrm{th}} = 40\,$eV), at least some D should be found.

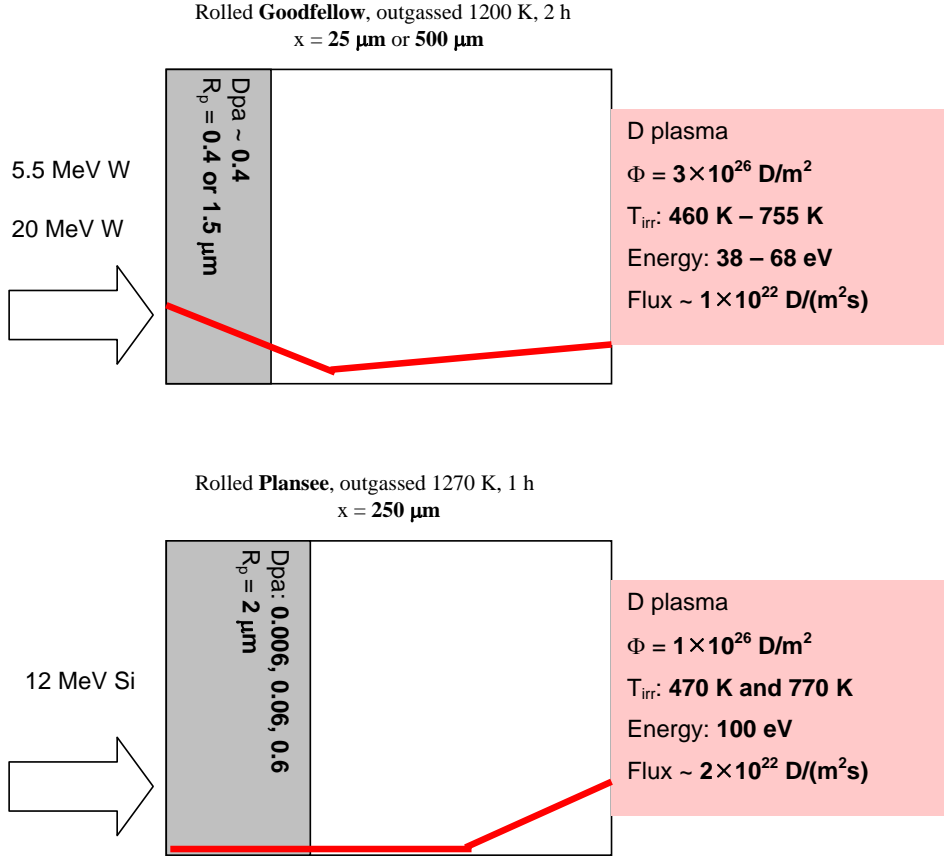All their D plasma exposure parameters are similar to those used in this work. Therefore,

Rolled **Goodfellow**, outgassed 1200 K, 2 h
x = **25 μm** or **500 μm**

5.5 MeV W

20 MeV W

Dpa ~ **0.4**
R_p = **0.4 or 1.5 μm**

D plasma

Φ = **3×10²⁶ D/m²**

T_irr: **460 K – 755 K**

Energy: **38 – 68 eV**

Flux ~ **1×10²² D/(m²s)**

Rolled **Plansee**, outgassed 1270 K, 1 h
x = **250 μm**

12 MeV Si

Dpa: **0.006, 0.06, 0.6**
R_p = **2 μm**

D plasma

Φ = **1×10²⁶ D/m²**

T_irr: **470 K and 770 K**

Energy: **100 eV**

Flux ~ **2×10²² D/(m²s)**

Figure 7.9: Schematic picture of the D depth profile (red line), and experimental parameters, as described in this work (upper graph) and by Wampler and Doerner [16, 147] (lower graph).

there should be no reason for such a discrepancy. Wampler's flux is twice as high, and his implantation fluence is three times lower, which gives a six times shorter exposure time, but the characteristic diffusion length for 470 K is 1 mm; meaning that D should be able to diffuse to traps located 0.25 mm beneath the surface.

Moreover, the difference may be connected to a lack of blistering. Wampler and Doerner [16, 147] observed precipitation on the front surface of their samples which were exposed to D plasma, resulting in a high D concentration on the plasma-exposed side. This precipitation may lead to a reduction of the D permeation flux to defects present 250 μm beneath the surface. The samples investigated in this work revealed no blistering, and the D concentration on the front side was rather low, therefore the diffusive flux was

higher. The reason for the presence of precipitation on Wampler's samples and its absence on the target studied here is unknown, but it suggests that different tungsten-based materials should be investigated in order to be able to make a good choice for Iter.

7.6.2 Model

The main purpose of the research described in this chapter was to investigate the D permeation and trapping in defects introduced in the material at depths of $25\,\mu$m and $500\,\mu$m beneath the surface (rear side). Although the D diffusion was slowest at 460 K, the highest retention and D concentration were observed at the damage peak. With increasing exposure temperature, the D retention decreased but was still higher at 755 K than in the undamaged samples.

Below, a model is given which describes the D behavior during plasma exposure in the samples investigated in this section. In equilibrium, a balance of fluxes leads to a D depth profile as shown in Fig. 7.10. In this case, the diffusion-limited release (i.e., $W > 1$ for $k_{\rm f}$ calculated according to the formula of Anderl et al. [44], see Sec. 2.2) takes place, thus the D concentration at the surfaces is equal to zero.

Three different regions can be distinguished: the D implantation zone: $0 - L_1$ (grey), the bulk: $L_1 - L_2$ (blue), and the self-damaged zone: $L_2 - L$ (yellow). Each zone is characterized by its diffusivity D_{0-2} and solubility S_{0-2}, where for the bulk D_1 and S_1 can be taken from Frauenfelder (see Sec. 2.3), and for the other two regions, the effective diffusivity can be calculated according to [149]:

$$D_{\rm eff} = \frac{D}{1 + K_{\rm T}\rho_{\rm tr}} \tag{7.1}$$

where D is Frauenfelder's diffusivity, $\rho_{\rm tr}$ is a temperature-dependent trap density which can be taken directly from the experiment (see Figs. 7.2 and 7.3), and $K_{\rm T}$ is the trap equilibrium constant which can be expressed as follows:

$$K_{\rm T} = \exp\frac{-(E_{\rm A} - E_{\rm T})}{kT_{\rm irr}} \tag{7.2}$$

Here, $E_{\rm A}$ is the energy required to jump from a solute site into a trap, which, in this approach, is taken to be equal to the activation energy for diffusion (see Eq. (2.19)): 0.39 eV according to Frauenfelder [30]; and $E_{\rm T}$ is the trap energy.

The effective solubilities S in the first and third region can be taken from the general expression:

$$C = Sa \tag{7.3}$$
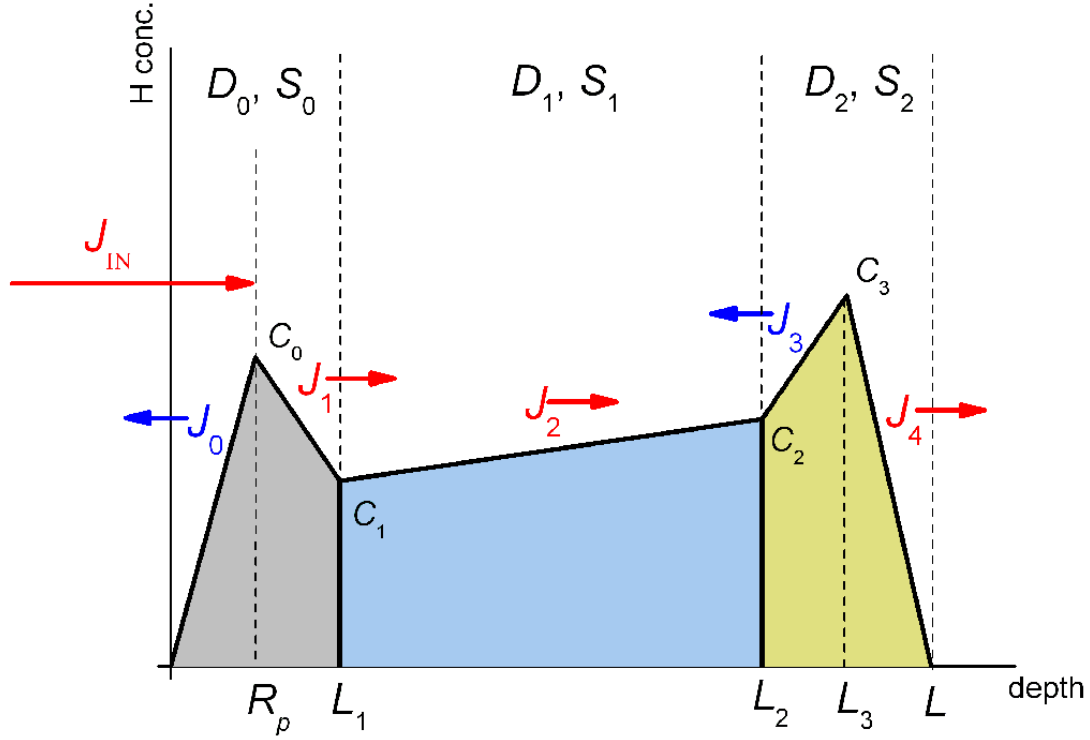
Figure 7.10: Schematic picture of D diffusion to the defects introduced in the rear side of the material (not to scale). The grey area denotes the D implantation region, the blue one the bulk, and the yellow one the zone damaged by self-implantation. Each section is characterized by a different set of diffusivities and solubilities. The D concentrations at different interfaces are shown. Positive fluxes (into the interface) are marked with red arrows, while negative fluxes (away from the interface) are marked with blue arrows.

Where C denotes the D concentration and can be obtained from the experiment (see Figs. 7.2 and 7.3) and a – the so-called activity – is an effective concentration. To obtain the activity, the equations which describe the flux balance have to be solved:

$$
\begin{aligned}
J_{\text{IN}} &= J_1 - J_0 && (7.4) \\
J_1 &= J_2 && (7.5) \\
J_2 &= -J_3 && (7.6) \\
-J_3 &= J_4 && (7.7)
\end{aligned}
$$

Here J_{IN} denotes the D incident flux, J_{0-4} are the inward and outward fluxes which by
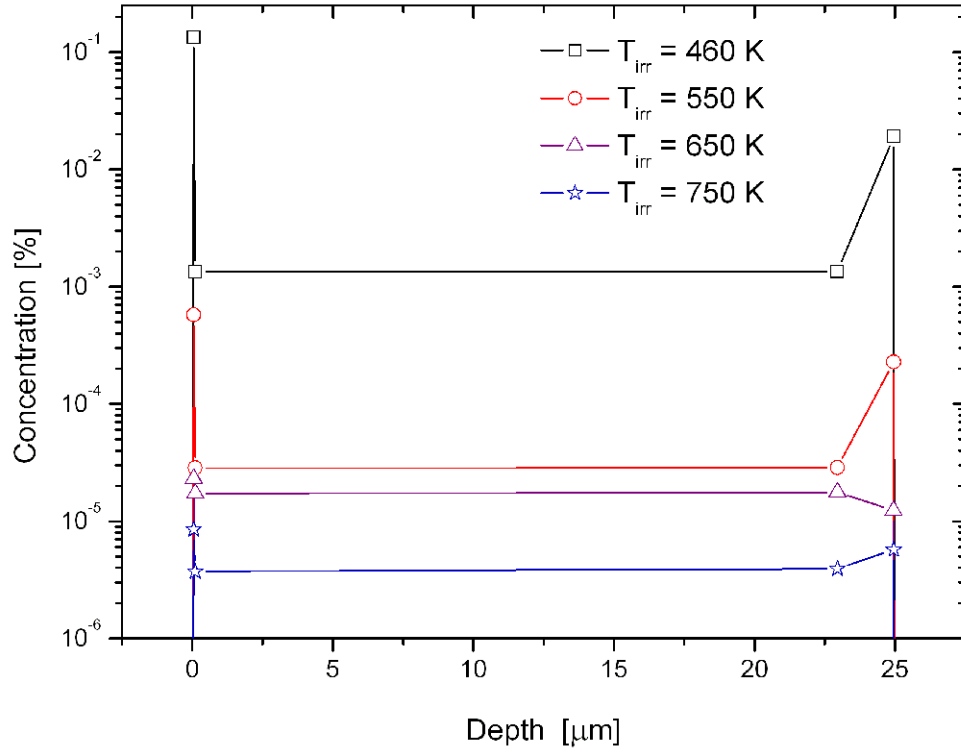
Figure 7.11: The D concentration vs. depth, obtained from simulations reflecting the situation during plasma exposure at elevated temperatures.

using Fick's law and Eq. (7.3), J can be written in a general form (see Sec. 2.2):

$$J = DN_{\mathrm{W}} \left(a \frac{\partial S}{\partial x} + S \frac{\partial a}{\partial x} \right) \tag{7.8}$$

where N_{W} denotes the W atomic density.

Based on the experimental parameters and some assumptions given below, the shape of the D profile during D plasma exposure (flux on) can be understood qualitatively according to the above model (see Fig. 7.11). The D incident flux is $J_{\mathrm{IN}} = 1 \times 10^{22}\,\mathrm{D/(m^2 s)}$, and the trap energies E_{T} are assumed to be $1.45\,\mathrm{eV}$ in the D irradiation zone [48, 137], $0.85\,\mathrm{eV}$ for the intrinsic defects in the bulk [48], and $1.8\,\mathrm{eV}$ for the VCs in the self-implanted zone [137]. For the $48\,\mathrm{eV}$ D plasma, $R_{\mathrm{p}} = 2\,\mathrm{nm}$, $L_2 = 50\,\mathrm{nm}$ is taken from Fig. 7.2a, the thickness of the sample is $L = 25\,\mu\mathrm{m}$, $L - L_3 = R_{\mathrm{p}}$, and – since it is very small – $L - L_2 = 2\,\mu\mathrm{m}$ which is the size of the self-implanted zone.

All simulated profiles (see Fig. 7.11) are in good agreement with the model (see Fig. 7.10) showing that the physics behind the processes are well-understood. In the near-surface layer, D profiles are characterized by a sharp concentration peak due to the plasma irra-

diation and then quickly decreases with depth. Later, permeating D is trapped by the defects introduced by the self-implantation, and its concentration increases significantly. Similarly to the data measured by NRA (see Figs. 7.2 and 7.3), the D concentration decreases with increasing exposure temperature. Quantitatively, the values obtained in this simulation differ from the values obtained by NRA, but the simulations reflect the situation in equilibrium during the plasma exposure (flux on), and the measured data shows trapped D after plasma exposure (flux off).

Chapter 8

Conclusions

Below, the findings of this work are summarized briefly, highlighting novel results and marking areas for future investigations.

8.1 Summary

Retention and trap density

In this work, D retention and trapping in damaged tungsten were studied. First of the kind results were obtained by measurements of D trapping in defects introduced in the rear side of W samples. The combination of this data with results of front side trapping experiments revealed that the trap density measured in the front side (as per standard procedure) does not reflect their actual number because it is disturbed by the interaction of deuterium ions with the defects. The trap density taken from the rear side of the sample is believed to represent the real number of traps introduced by n irradiation of W. In Fig. 8.1, the trapped D-to-W ratio (trap density) is shown as a function of the irradiation temperature. The amount of D trapped in the radiation defects present in the front side (black solid squares) of the targets reveals a synergetic effect between plasma and defects; and it is much higher than in the defects introduced in the rear side (triangles). This is caused by the interaction of D with the traps, e.g.: interstitial-type dislocation loop formation which is favored in the vicinity of superabundant vacancies. The high D trapping in the front side is visible even when substracting the data measured for the undamaged samples (black empty squares) from the raw data obtained for the damaged targets (black solid squares). By doing so, the effect of plasma exposure would be expected to be separated from the trapping effect. It is not, however, as D behaves differently in the presence solely of intrinsic defects (i.e., undamaged W) than
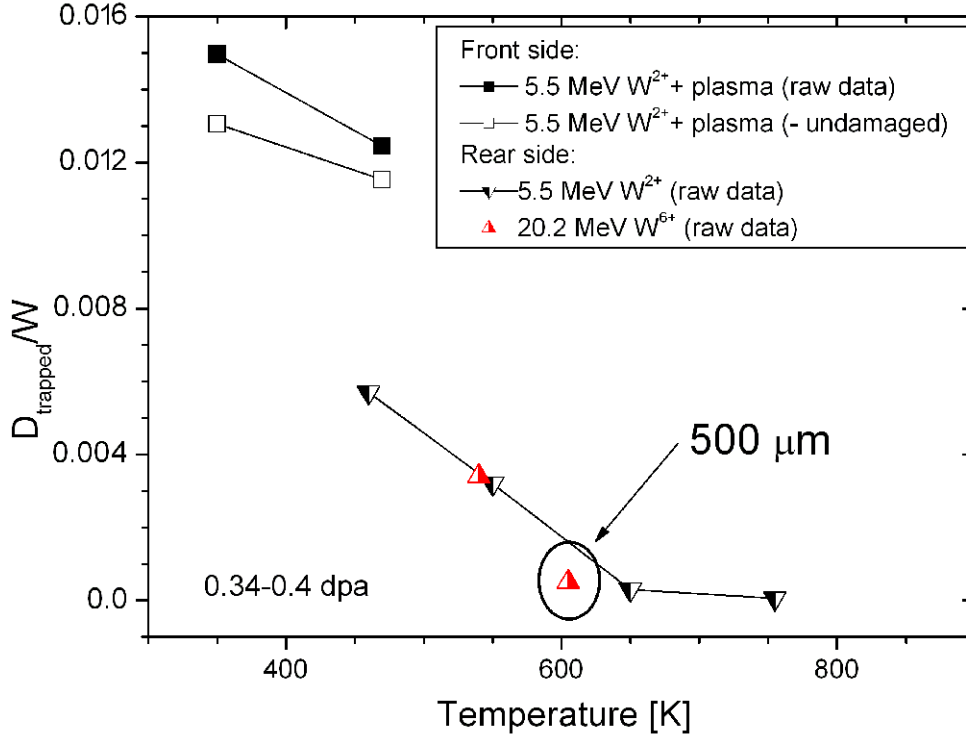
Figure 8.1: Trapped D-to-W ratio (trap density) in the region $0.2 - 0.7\,\mu$m as a function of the exposure temperature, measured in the front (squares) and the back side (triangles) of the samples damaged either by $5.5\,$MeV or $20.2\,$MeV W ions to around $0.4\,$dpa. Mostly, raw data is presented, except in the case where the amount of D trapped in the undamaged W was subtracted from the amount of D trapped in the damaged W (black empty squares) for the samples irradiated under the same conditions.

in the presence of radiation-induced damage. In the rear side, D ions do not interact as strongly with the defects, and therefore, the synergetic effect between the plasma and the defects is not observed on the back side where the D permeated.

By neglecting the interaction of D ions with the defects, and using the back side level of the temperature-dependent trap density (see Fig. 8.1, triangles), one can estimate the tritium retention in Iter at the end of its lifetime (i.e., after $2 \times 10^7\,$s), assuming that D and T are distributed equally in the traps present in Iter's $210\,$m^2 W wall (see Tab. 8.1). The T concentration in solution was calculated according to Eq. (2.16), assuming $\Phi_{\mathrm{diff}} = J_{\mathrm{IN}} = 1 \times 10^{22}\,$T/(m^{2}s) and $x = R_{\mathrm{p}} = 2\,$nm.

With increasing irradiation temperature, the depth x (calculated from Eq. (2.17)) to which the D diffusion extends always increases, and this tendency is reflected in the

temperature [K]	ρ_{tr}	C_{s}	x [mm]	Q_{ret}[g]
460	0.0057	1.4×10^{-5}	1.5	282
550	0.0032	2.9×10^{-6}	1.9	218
650	0.0003	8.1×10^{-7}	6.5	65
755	0.00006	3.2×10^{-7}	14.5	29

Table 8.1: Estimated D retention Q_{ret} in Iter and the depth x to which traps will be populated, calculated at different exposure temperatures and at various, temperature-dependent trap densities ρ_{tr}. The values for Q_{ret} were obtained assuming 50% of T in the $210 \, \text{m}^2$ of the W wall. The realistic tritium mass of $5 \times 10^{-24} \, \text{g}$ was taken.

deuterium retention Q_{ret} (calculated from Eq. (2.18)) which shows a maximum at 460 K before decreasing. The reason for this is that the trap density drops with temperature. These two processes are competing, and, in consequence, the highest D retention of 282 g is reached at an exposure temperature of 460 K. This corresponds to roughly 40% of the overall tritium retention limit.

In Ch. 6, it was shown that in the presence of carbon, the D diffusion is diminished. This effect will play only a minor role in Iter, however, as the carbon energies and concentrations will be much lower than those used in this work.

Mechanism

Based on the results obtained from self-implanted W (see Chs. 5 and 7), the mechanism of damage creation and the D behavior in the defects can be described as follows. Damaging of pure W at RT results in the creation of vacancies and vacancy clusters from which D desorbs at around 820 K. These defects can be removed by annealing at 1200 K for 2 h. The defect development is time-dependent and approaches saturation at 0.4 dpa (i.e., at the end of Iter's lifetime). This means that in Iter, n irradiation is not an important issue—it only accumulates in the late phase of operation. This work is much more relevant for DEMO and other future reactors. According to Igata et al. [133], the trap formation is proportional to the square root of the irradiation fluence (or dpa). In the present work, the former was observed to scale as $\text{dpa}^{0.3}$ up to a level of $\sim 40 \, \text{dpa}$, while further damaging leads to a decrease of the number of traps due to an overlap of the depleted zones. Introducing defects at higher temperatures can cause void formation, and higher temperatures would be required to anneal out these traps. Beyond the damage zone, high stresses occur, leading to plastic deformations like the

creation of dislocation loops. This effect will not be seen in Iter, because n-induced traps will be distributed volumetrically throughout the entire material.

Plasma interaction with the defects will lead to the formation of interstitial-type dislocation loops. These traps, in conjunction with the presence of vacancies and vacancy clusters, will significantly enhance the D/T retention. Due to the presence of dislocation loops, the increase of D/T retention in the first few micrometers will be higher by a factor of five to eight relative to the undamaged W, while this value should be lower in the bulk where D will only interact weakly with the defects. In the presence of radiation-induced defects, the effective solubility of D is increased, which should hold back W surface blistering, crack formation, and flaking.

From this perspective, the worst operation temperature for Iter would be at around $460 - 550\,\mathrm{K}$, while in order to keep deuterium retention low and to avoid tungsten blistering, the effective temperature on the tungsten surface should lie above $800\,\mathrm{K}$. Even in the worst temperature case, the tritium inventory in Iter at the end of its lifetime will be far below the administrative limit, because even if, due to the presence of newly created traps, the T concentration will be high, its diffusion to the bulk will be comparatively slow.

8.2   Future Investigations

In general, W self-implantation seems to be a good substitute for neutrons. Nonetheless, in order to obtain deeper damage profiles, either higher W ion energies or other particles have to be used for damaging. This way, the relation between the stress build-up beyond the damage zone and the size of the damage zone can be investigated. Particle irradiation is not capable of simulating transmutation effects. To this end, rhenium or osmium can be used instead of W ions, in particular since, in the presence of transmutaion products, defect creation occurs at slower rates [100].

The question remains to which depth the trap density level on the front side (see Fig. 8.1, black squares) should be used, and at which point the rear side level (see Fig. 8.1, triangles) should be taken into account when estimating the T retention in Iter. To answer this question, it is necessary to damage W to far greater depths and to investigate the D behavior in thusly enlarged damage regions.

As shown in Sec. 7.6, deuterium behaves differently in different materials, i.e., precipitation and blistering can occur which hinder D diffusion to the traps and therefore lower the D retention. Thus, D retention and trapping in other types of Iter-grade tungsten should be studied.

To account for void formation during n irradiation of tungsten, self-implantation should be performed at elevated temperatures: around 900 K to enable void creation and at around 1350 K to allow for the formation of vacancy-type dislocation loops. By damaging W at RT and subsequently annealing the samples at various temperatures, studies of defect recovery can be performed.

Appendix A

How many vacancies are in a void?

There is no definition of the void size in terms of its diameter or vacancy content. Some time ago, it was accepted that objects observed by SEM are blisters, those observed by TEM are voids, and the ones observed by FIM are vacancies and vacancy clusters. Since the best TEMs now reach a resolution of $\sim 0.15\,\text{nm}$ [151], this criterion seems to be no longer sufficient. In any case, the void size should not be defined by its spatial size, because this feature carries no information about thermodynamic properties of such a void and should be used only as an estimation. One can approximate the void size, knowing that a void surface exhibits the same properties as a material-free surface in which a void exists. Therefore, the relation between the Helmholtz free energy F_S per vacancy and the number of vacancies N_t in the void (see Fig. A.1) can be used [152].

The surface of a void in tungsten with an infinite number of vacancies can be treated as a free surface of tungsten. In this case, the free energy per vacancy equals $0.048\,\text{aJ}$ and will henceforth be considered to be the ground level. The free energy for one vacancy lies at around $0.18\,\text{aJ}$ and is subsequently considered to be the maximum. Now, some limit has to be set by assuming, e.g., that objects with a free energy below 20% of the maximum energy minus the ground level are considered to be voids, and above vacancy clusters. This means that an object which contains 135 and more vacancies can be called a void and can be expected to display the same behavior as a free tungsten surface: e.g., to have the same heat of chemisorption. Objects which contain less than 135 vacancies are called vacancy clusters. Having defined this boundary, one can obtain a connection between the number of vacancies in a void and the void radius (see Fig. A.2).

When voids are formed, they prefer to minimize their potential energy, resulting in a tetrakaidecahedronal shape [150]. For the purpose of the following argument, however, this property is neglected in order to simplify the calculations, and the voids are assumed to be cubic. From the relation between the cubic void size R_{void} and the number of
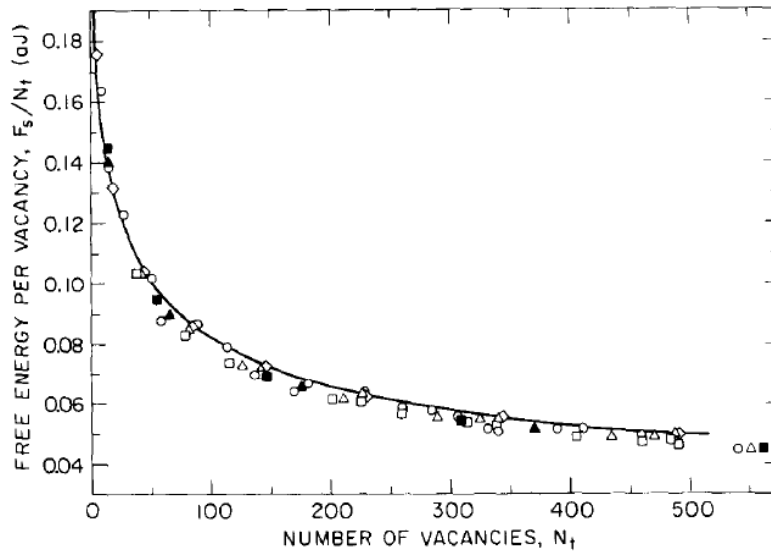
Figure A.1: Helmholtz free energy per vacancy vs. number of vacancies in bcc tungsten. Different symbols denote various void shapes. Source: [150]
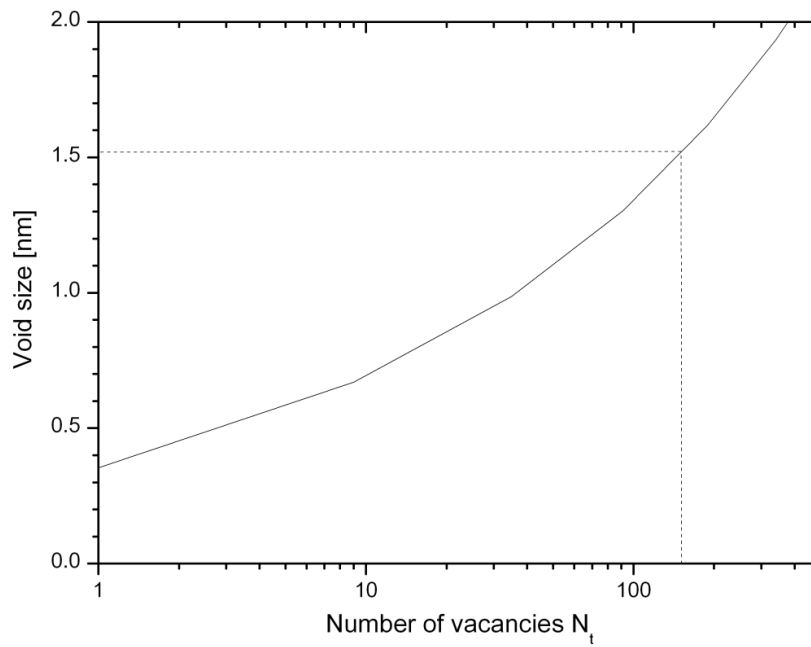
Figure A.2: The void size dependence on the number of vacancies in bcc W. The dashed line corresponds to the threshold between VCs and voids.

vacancies N_t in bcc tungsten – as shown in Fig. A.2 – one can conclude that the minimum void radius should lie around $1.5\,\mathrm{nm}$.

Acknowledgments

Bibliography

[1] http://www.iter.org, 2010.

[2] ITER Technical Basis, G A0 FDR 1 01-07-13 R1.0, 2.13 Material Assessment, 2001.

[3] J. Roth, E. Tsitrone, T. Loarer, V. Philipps, S. Brezinsek, A. Loarte, G. F. Counsell, R. P. Doerner, K. Schmid, O. V. Ogorodnikova, R. A. Causey, Tritium inventory in ITER plasma-facing materials and tritium removal procedures, Plasma Phys. Control. Fusion 50 (2008) 103001.

[4] P. Sardain, B. Michel, L. Giancarli, A. L. Puma, Y. Poitevin, J. Szczepanski, D. Maisonnier, D. Ward, U. Fischer, P. Pereslavtsev, A. Natalizio, J. Collen, A. Orden Martinez, Power plant conceptual study-WCLL concept, Fus. Eng. Des. 69 (2003) 769–774.

[5] H. Iida, V. Khripunov, L. Petrizzi, G. Federici, Nuclear Analysis Group, ITER Naka & Garching Joint Work Sites, Nuclear Analysis Report, G 73 DDD 2 W 0.2, 2004.

[6] Design Requirements and Guidelines Level 1 (DRG1), G A0 GDRD 2 01-07-13 R 1.0, Vienna: IAEA, 2004.

[7] G. Federici, C. H. Skinner, J. N. Brooks, J. P. Coad, C. Grisolia, A. A. Haasz, A. Hassanein, V. Philipps, C. S. Pitcher, J. Roth, W. R. Wampler, D. G. Whyte, Plasma material interactions in current tokamaks and their implications for next step fusion reactors, IAEA, Vienna, Nucl. Fusion 41 (2001) 1967–2137.

[8] ITER Technical Basis, G A0 FDR 1 01-07-13 R1.0, Divertor, 2001.

[9] V. K. Alimov, B. Tyburska, M. Balden, J. Roth, K. Isobe, T. Yamanishi, Surface morphology and deuterium retention in tungsten trioxide exposed to low-energy, high flux D plasma, submitted to J. Nucl. Mater .

[10] R. Neu, M. Balden, V. Bobkov, R. Dux, O. Gruber, A. Herrmann, A. Kallenbach, M. Kaufmann, C. F. Maggi, H. Maier, H. W. Müller, T. Pütterich, R. Pugno, V. Rohde, A. C. C. Sips, J. Stober, W. Suttrop, C. Angioni, C. V. Atanasiu, W. Becker, K. Behler, K. Behringer, A. Bergmann, T. Bertoncelli, R. Bilato, A. Bottino, M. Brambilla, F. Braun, A. Buhler, A. Chankin, G. Conway, D. P. Coster, P. de Marné, S. Dietrich, K. Dimova, R. Drube, T. Eich, K. Engelhardt, H. Fahrbach, U. Fantz, L. Fattorini, J. Fink, R. Fischer, A. Flaws, P. Franzen, J. C. Fuchs, K. Gál, M. G. Muñoz, M. Gemisic-Adamov, L. Giannone, S. Gori, S. da Graca, H. Greuner, A. Gude, S. Günter, G. Haas, J. Harhausen, B. Heinemann, N. Hicks, J. Hobirk, D. Holtum, C. Hopf, L. Horton, M. Huart, V. Igochine, S. Kálvin, O. Kardaun, M. Kick, G. Kocsis, H. Kollotzek, C. Konz, K. Krieger, T. Kurki-Suonio, B. Kurzan, K. Lackner, P. T. Lang, P. Lauber, M. Laux, J. Likonen, L. Liu, A. Lohs, K. Mank, A. Manini, M. Manso, M. Maraschek, P. Martin, Y. Martin, M. Mayer, P. McCarthy, K. McCormick, H. Meister, F. Meo, P. Merkel, R. Merkel, V. Mertens, F. Merz, H. Meyer, M. Mlynek, F. Monaco, H. Murmann, G. Neu, J. Neuhauser, B. Nold, J. Noterdaeme, G. Pautasso, G. Pereverzev, E. Poli, M. J. Pueschel, G. Raupp, M. Reich, B. Reiter, T. Ribeiro, R. Riedl, J. Roth, M. Rott, F. Ryter, W. Sandmann, J. Santos, K. Sassenberg, A. Scarabosio, G. Schall, J. Schirmer, A. Schmid, W. Schneider, G. Schramm, R. Schrittwieser, W. Schustereder, J. Schweinzer, S. Schweizer, B. Scott, U. Seidel, F. Serra, M. Sertoli, A. Sigalov, A. Silva, E. Speth, A. Stäbler, K. Steuer, E. Strumberger, G. Tardini, C. Tichmann, W. Treutterer, C. Tröster, L. Urso, E. Vainonen-Ahlgren, P. Varela, L. Vermare, D. Wagner, M. Wischmeier, E. Wolfrum, E. Würsching, D. Yadikin, Q. Yu, D. Zasche, T. Zehetbauer, M. Zilker, H. Zohm, Plasma wall interaction and its implication in an all tungsten divertor tokamak, Plasma. Phys. Control. Fusion 49 (2007) B59.

[11] B. M. Oliver, R. A. Causey, S. A. Maloy, Deuterium retention and release from highly irradiated annealed tungsten after exposure to a deuterium DC glow discharge, J. Nucl. Mater. 329-333 (2004) 977–981.

[12] M. Fukumoto, H. Kashiwagi, Y. Ohtsuka, Y. Ueda, M. Taniguchi, T. Inoue, K. Sakamoto, J. Yagyu, T. Arai, I. Takagi, T. Kawamura, Deuterium trapping in tungsten damaged by high-energy hydrogen ion irradiation, J. Nucl. Mater. 390-391 (2009) 572–575.

[13] M. Fukumoto, H. Kashiwagi, Y. Ohtsuka, Y. Ueda, Y. Nobuta, J. Yagyu, T. Arai,

M. Taniguchi, T. Inoue, K. Sakamoto, Hydrogen behavior in damaged tungsten by high-energy ion irradiation, J. Nucl. Mater. 386-388 (2009) 768–771.

[14] I. I. Arkhipov, S. L. Kanashenko, V. M. Sharapov, R. Kh. Zalavutdinov, A. E. Gorodetsky, Deuterium trapping in ion-damaged tungsten single crystal, J. Nucl. Mater. 363-365 (2007) 1168–1172.

[15] A. van Veen, H. A. Filius, J. de Vries, K. R. Bijkerk, G. J. Rozing, D. Segers, Hydrogen exchange with voids in tungsten observed with TDS and PA, J. Nucl. Mater. 155-157 (1988) 1113–1117.

[16] W. R. Wampler, R. P. Doerner, The influence of displacement damage on deuterium retention in tungsten exposed to plasma, Nucl. Fusion 49 (2009) 115023.

[17] J. Roth, E. Tsitrone, A. Loarte, T. Loarer, G. Counsell, R. Neu, V. Philipps, S. Brezinsek, M. Lehnen, P. Coad, C. Grisolia, K. Schmid, K. Krieger, A. Kallenbach, B. Lipschultz, R. Doerner, R. Causey, V. Alimov, W. Shu, O. Ogorodnikova, A. Kirschner, G. Federici, A. Kukushkin, EFDA PWI Task Force, ITER PWI Team, Fusion for Energy, ITPA SOL/DIV, Recent analysis of key plasma wall interactions issues for ITER, J. Nucl. Mater. 390-391 (2009) 1–9.

[18] D. G. Whyte, On the consequence of neutron induced damaged for volumetric fuel retention in plasma facing materials, J. Nucl. Mater. 390-391 (2009) 911–915.

[19] W. Eckstein, Computer Simulation of Ion-Solid Interactions, Springer, Berlin, 1991.

[20] http://www.srim.org/SRIM/Tutorials/Tutorials.htm, 2010.

[21] R. A. Causey, Hydrogen isotope retention and recycling in fusion reactor plasma-facing components, J. Nucl. Mater. 300 (2002) 91–117.

[22] V. K. Alimov, K. Ertl, J. Roth, Deuterium retention and lattice damage in tungsten irradiated with D ions, J. Nucl. Mater. 290-293 (2001) 389–393.

[23] W. Eckstein, C. Garcia-Rosales, J. Roth, W. Ottenberger, Sputtering data, Report 9/82, Max-Planck-Institut für Plasmaphysik, Garching, 1993.

[24] B. L. Doyle, A simple theory for maximum H inventory and release: a new transport parameter, J. Nucl. Mater. 111-112 (1982) 628–635.

[25] W. Möller, The behaviour of hydrogen atoms implanted into metals, Nucl. Instrum. Methods 209-210 (1983) 773–790.

[26] W. M. Shu, Y. Hayashi, K. Okuno, Surface recombination of hydrogen in plasma-driven permeation, J. Nucl. Mater. 220-222 (1995) 497–500.

[27] D. N. Beshers, An investigation of interstitial sites in the bcc lattice, J. Appl. Phys. 36 (1965) 290–300.

[28] Y.-L. Liu, Y. Zhang, G.-N. Luo, G.-H. Lu, Structure, stability and diffusion of hydrogen in tungsten: A first-principles study, J. Nucl. Mater. 390-391 (2009) 1032–1034.

[29] A. P. Zakharov, V. M. Sharapov, A. A. Babad-Zakhryapin, Permeation of hydrogen through molybdenum and tungsten at elevated temperatures, Proc. 1st Int. Congress on Hydrogen in Metals, Paris, France, 217–221, 1972.

[30] R. Frauenfelder, Solution and diffusion of hydrogen in tungsten, J. Vac. Sci. Tech. 6 (1968) 388–397.

[31] A. K. Zhetbaev, A. N. Ozerny, Y. G. Sevostianov, Using of the Mossbauer effect on ^{181}Ta for study of the hydrogen diffusion in tungsten, Fiz. Met. Metalloved. 62 (1986) 749–752.

[32] G. E. Moore, F. C. Unterwald, Thermal dissociation of hydrogen, J. Chem. Phys. 40 (1964) 2639–2652.

[33] L. N. Ryabchikov, Mass spectrometric investigation of degassing of molybdenum, tungsten, and niobium on heating them in a vacuum, Ukr. Phys. J. 9 (1964) 293–302.

[34] G. A. Esteban, A. Perujo, L. A. Sedano, K. Douglas, Hydrogen isotope diffusive transport parameters in pure polycrystalline tungsten, J. Nucl. Mater. 295 (2001) 49–56.

[35] G. Benamati, E. Serra, C. H. Wu, Hydrogen and deuterium transport and inventory parameters through W and W-alloys for fusion reactor applications, J. Nucl. Mater. 283-287 (2000) 1033–1037.

[36] T. Otsuka, T. Hoshihira, T. Tanabe, Visualization of hydrogen depth profile by means of tritium imaging plate technique: determination of hydrogen diffusion coefficient in pure tungsten, Phys. Scr. T138 (2009) 014052.

[37] P. Franzen, C. Garcia-Rosales, H. Plank, V. K. Alimov, Hydrogen trapping in and release from tungsten: Modeling and comparison with graphite with regard to its use as fusion reactor material, J. Nucl. Mater. 241-243 (1997) 1082–1086.

[38] C. Garcia-Rosales, P. Franzen, H. Plank, J. Roth, E. Gauthier, Re-emission and thermal desorption of deuterium from plasma sprayed tungsten coatings for application in ASDEX-upgrade, J. Nucl. Mater. 233-237 (1996) 803–808.

[39] C. A. Wert, C. Zener, Interstitial atomic diffusion coefficients, Phys. Rev. 76 (1949) 1169.

[40] Y. Fukai, H. Sugimoto, Diffusion of hydrogen in metals, Adv. Phys. 34 (1985) 263–326.

[41] H. Wipf, Solubility an diffusion of hydrogen in pure metals and alloys, Phys. Scr. T94 (2001) 43–51.

[42] A. A. Mazayev, R. G. Avarbe, Y. N. Wilk, O rastvorimosti vodoroda v volframye pri vysokich temperaturach i davdyenyach, Izv. Akad. Nauk. 6 (1968) 223–226.

[43] A. P. Zakharov, V. M. Sharapov, E. I. Evko, Hydrogen permeability of polycrystalline and monocrystalline molybdenum and tungsten, translated from Fiziko-Khimicheskaya Mekhanika Materialov 9 (1973) 29–33, Institute of Physical Chemistry, Academy of Sciences of the USSR, Moscow.

[44] R. A. Anderl, D. F. Holland, G. R. Longhurst, R. J. Pawelko, C. L. Trybus, C. H. Sellers, Deuterium transport and trapping in polycrystalline tungsten, Fus. Tech. 21 (1992) 745–752.

[45] O. V. Ogorodnikova, J. Roth, M. Mayer, Deuterium retention in tungsten in dependence of surface conditions, J. Nucl. Mater. 313-316 (2003) 469–477.

[46] V. K. Alimov, Deuterium Retention in Pure and Mixed Plasma Facing Materials, Phys. Scr. T108 (2004) 46–56.

[47] R. A. Causey, R. Doerner, H. Fraser, R. D. Kolasinski, J. Smugeresky, K. Umstadter, R. Williams, Defects in tungsten responsible for molecular hydrogen isotope retention after exposure to low energy plasmas, J. Nucl. Mater. 390-391 (2009) 717–720.

[48] O. V. Ogorodnikova, J. Roth, M. Mayer, Pre-implantation and pre-annealing effects on deuterium retention in tungsten, J. Nucl. Mater. 373 (2008) 254–258.

[49] O. V. Ogorodnikova, J. Roth, M. Mayer, Ion-driven deuterium retention in tungsten, J. Appl. Phys. 103 (2008) 034902.

[50] M. Poon, A. A. Haasz, J. W. Davis, R. G. Macaulay-Newcombe, Impurity effects and temperature dependence of D retention in single crystal tungsten, J. Nucl. Mater. 313-316 (2003) 199–203.

[51] M. Poon, J. W. Davis, A. A. Haasz, Effect of carbon pre-implantation on deuterium retention in tungsten, J. Nucl. Mater. 283-287 (2000) 1062–1067.

[52] A. A. Haasz, J. W. Davis, M. Poon, R. G. Macaulay-Newcombe, Deuterium retention in tungsten for fusion use, J. Nucl. Mater. 258-263 (1998) 889–895.

[53] V. K. Alimov, B. M. U. Scherzer, Deuterium retention and re-emission from tungsten materials, J. Nucl. Mater. 240 (1996) 75–80.

[54] A. A. Haasz, M. Poon, J. W. Davis, The effect of ion damage on deuterium trapping in tungsten, J. Nucl. Mater. 266-269 (1999) 520–525.

[55] V. K. Alimov, W. M. Shu, J. Roth, K. Sugiyama, S. Lindig, M. Balden, K. Isobe, T. Yamanishi, Surface morphology and deuterium retention in tungsten exposed to low-energy, high flux pure and helium-seeded deuterium plasmas, Phys. Scr. T138 (2009) 014048.

[56] H. Eleveld, A. van Veen, Deuterium interaction with impurities in tungsten studied with TDS, J. Nucl. Mater. 191-194 (1992) 433–438.

[57] B. M. U. Scherzer, in Sputtering by particle bombardment II, ed. R. Behrisch, Chapter 7: Development of surface topography due to gas ion implantation, Springer, Berlin, 1983.

[58] J. B. Condon, T. Schober, Hydrogen bubbles in metals, J. Nucl. Mater. 207 (1993) 1–24.

[59] K. Tokunaga, M. J. Baldwin, R. P. Doerner, N. Noda, Y. Kubota, N. Yoshida, T. Sogabe, T. Kato, B. Schedler, Blister formation and deuterium retention on tungsten exposed to low energy and high flux deuterium plasma, J. Nucl. Mater. 337-339 (2005) 887–891.

[60] T. Matsui, S. Muto, T. Tanabe, TEM study on deuterium-irradiation-induced defects in tungsten and molybdenum, J. Nucl. Mater. 283-287 (2000) 1139–1143.

[61] R. Sakamoto, T. Muroga, N. Yoshida, Microstructural evolution induced by low energy hydrogen ion irradiation in tungsten, J. Nucl. Mater. 220-222 (1995) 819–822.

[62] R. Sakamoto, T. Muroga, N. Yoshida, Retention and desorption of implanted deuterium and high-Z plasma facing materials, J. Nucl. Mater. 233-237 (1996) 776–780.

[63] J. H. Evans, An interbubble fracture mechanism of blister formation on helium-irradiated metals, J. Nucl. Mater. 68 (1977) 129–140.

[64] J. H. Evans, The role of implanted gas and lateral stress in blister formation mechanism, J. Nucl. Mater. 76-77 (1978) 228–234.

[65] J. Roth, R. Behrisch, B. M. U. Scherzer, Blistering of niobium due to 0.5 to 9 keV helium and hydrogen bombardment, J. Nucl. Mater. 53 (1974) 147–153.

[66] E. P. EerNisse, S. T. Picraux, Role of integrated lateral stress in surface deformation of He-implanted surfaces, J. Appl. Phys. 48 (1997) 9–17.

[67] T. Venhaus, R. Causey, R. Doerner, T. Abeln, Behavior of tungsten to high fluences of low energy hydrogen isotopes, J. Nucl. Mater. 290-293 (2001) 505–508.

[68] W. Wang, J. Roth, S. Lindig, C. H. Wu, Blister formation of tungsten due to ion bombardment, J. Nucl. Mater. 299 (2001) 124–131.

[69] K. Tokunaga, R. P. Doerner, R. Seraydarian, N. Noda, N. Yoshida, T. Sogabe, T. Kato, B. Schedler, Modification of tungsten coated carbon by low energy and high flux deuterium irradiation, J. Nucl. Mater. 307-311 (2002) 126–129.

[70] M. Y. Ye, H. Kanehara, S. Fukuta, N. Ohno, S. Takamura, Blister formation on tungsten surface under low energy and high flux hydrogen plasma irradiation in NAGDIS-I, J. Nucl. Mater. 313-316 (2003) 72–76.

[71] T. Shimada, H. Kikuchi, Y. Ueda, A. Sagara, M. Nishikawa, Blister formation in tungsten by hydrogen and carbon mixed ion beam irradiation, J. Nucl. Mater. 313-316 (2003) 204–208.

[72] W. M. Shu, High-dome blisters formed by deuterium-induced local superplasticity, Appl. Phys. Lett. 92 (2008) 211904–1–3.

[73] G.-N. Luo, W. M. Shu, M. Nishi, Incident energy dependence of blistering at tungsten irradiated by low energy high flux deuterium plasma beams, J. Nucl. Mater. 347 (2005) 111–117.

[74] W. M. Shu, G.-N. Luo, T. Yamanishi, Mechanism of retention and blistering in near-surface region of tungsten exposed to high flux deuterium plasmas of tens of eV, J. Nucl. Mater. 367-370 (2007) 1463–1467.

[75] W. M. Shu, E. Wakai, T. Yamanishi, Blister bursting and deuterium bursting release from tungsten exposed to high fluence of high flux and low energy deuterium plasma, Nucl. Fusion 47 (2007) 201–209.

[76] W. M. Shu, M. Nakamichi, V. K. Alimov, G.-N. Luo, K. Isobe, T. Yamanishi, Deuterium retention, blistering and local melting at tungsten exposed to high-fluence deuterium plasma, J. Nucl. Mater. 390-391 (2009) 1017–1021.

[77] T. Shimada, Y. Ueda, M. Nishikawa, Mechanism of blister formation on tungsten surface, Fus. Eng. Des. 66-68 (2003) 247–251.

[78] Y. Ueda, T. Shimada, M. Nishikawa, Impacts of carbon impurities in hydrogen plasmas on tungsten blistering, Nucl. Fusion 44 (2004) 62–67.

[79] Y. Ueda, T. Funabiki, T. Shimada, K. Fukumoto, H. Kurishita, M. Nishikawa, Hydrogen blister formation and cracking behavior for various tungsten materials, J. Nucl. Mater. 337-339 (2005) 1010–1014.

[80] T. Funabiki, T. Shimada, Y. Ueda, M. Nishikawa, Effect of tungsten microstructure on blister formation by hydrogen and carbon mixed ion beam irradiation, J. Nucl. Mater. 329-333 (2004) 780–784.

[81] N. Y. Park, Y. C. Kim, H. K. Seok, S. H. Han, S. Cho, P. R. Cha, Molecular dynamics simulation of irradiation damage in tungsten, Nucl. Instrum. Methods Phys. Res. B 265 (2007) 547–552.

[82] J. R. Beeler, Jr., Displacement spikes in cubic metals. I. α-iron, copper, and tungsten, Phys. Rev. 150 (1966) 470–487.

[83] A. F. Bobkov, V. T. Zabolotnyi, L. I. Ivanov, G. M. Kukavadze, N. A. Makhlin, A. L. Suvorov, Field Ion Microscopy of radiation defects in tungsten irradiated with 50-keV W ions. I. Method and results and II. Discussion and experimental results, At. Energ. 48 (1980) 326–327, translation to English and published by Springer, New York.

[84] W. S. O. T. Inal, 800 MeV proton damage in tungsten and molybdenum: a Field-Ion-Microscope observation, J. Nucl. Mater. 99 (1981) 94–99.

[85] J. Fikar, R. Schaeublin, Molecular dynamics simulation of radiation damage in bcc tungsten, Nucl. Instrum. Methods Phys. Res. B 255 (207) 27–31.

[86] Q. Xu, N. Yosida, T. Yoshiie, Dynamic simulation of multiplier effects of helium plasma and neutron irradiation on microstructural evolution in tungsten, Mater. Trans. 46 (2005) 1255–1260.

[87] L. K. Keys, J. Moteff, Neutron irradiation and defect recovery of tungsten, J. Nucl. Mater. 34 (1970) 260–280.

[88] Q. Xu, T. Yoshiie, H. C. Huang, Molecular dynamics simulation of vacancy diffusion in tungsten induced by irradiation, Nucl. Instrum. Methods Phys. Res. B 206 (2003) 123–126.

[89] G. S. Was, T. Allen, Radiation induced segregation in multicomponent alloys: effect of particle type, Mater. Charact. 32 (1994) 239–255.

[90] P. Vladimirov, S. Bouffard, Displacement damage and transmutations in metals under neutron and proton irradiation, C. R. Physique 9 (2008) 303–322.

[91] G. S. Was, Fundamentals of Radiation Material Science, Metals and Alloys, Springer, Berlin, 2007.

[92] G. H. Kinchin, R. S. Pease, The displacement of atoms in solids by radiation, Rep. Prog. Phys. 18 (1955) 1–51.

[93] M. J. Norgett, M. T. Robinson, I. M. Torrens, A proposed method of calculating displacement dose rates, Nucl. Eng. Des. 33 (1975) 50–54.

[94] J. Lindhard, V. Nielsen, M. Scharff, P. V. Thomsen, Integral equations governing radiation effects, Mat. Fys. Medd. Dan. Vidensk. Selsk. 33 (1963) 1–42.

[95] W. Möller, W. Eckstein, TRIDYN - Binary Collision simulation of atomic collisions dynamic composition changes in solids, Report 9/64, Max-Planck-Institut für Plasmaphysik, Garching, 1988.

[96] M. Attardo, J. M. Galligan, A Field Ion Microscope study of neutron irradiated tungsten, Phys. Stat. Sol 16 (1966) 449–457.

[97] M. J. Attardo, J. M. Galligan, J. G. Y. Chow, Interstitial removal in Stage-III recovery of neutron-irradiated W, Phys. Rev. Lett. 19 (1967) 73–74.

[98] D. Jeannotte, J. M. Galligan, Energy of motion of vacancies in tungsten, Phys. Rev. Lett. 19 (1967) 232–233.

[99] L. K. Keys, J. P. Smith, J. Moteff, High-temperature recovery of tungsten after neutron irradiation, Phys. Rev. 176 (1968) 851–856.

[100] J. C. He, A. Hasegawa, K. Abe, Effects of transmutation elements on the defect structure development of W irradiated by protons and neutrons, J. Nucl. Mater. 377 (2008) 348–351.

[101] P. M. G. Nambissan, P. Sen, Positron annihilation studies on alpha irradiated tungsten, Solid State Commun. 71 (1989) 1165–1167.

[102] P. M. G. Nambissan, P. Sen, Positron annihilation study of the annealing behaviour of alpha induced defects in tungsten, Radiat. Eff. Defects Solids 124 (1992) 215–221.

[103] Z. Shengyun, X. Yongjun, W. Zhiqiang, Z. Yongnan, Z. Dongmei, D. Enpeng, Y. Daqing, M. Fukuda, M. Mihara, K. Matsuta, T. Minamisono, Positron annihilation lifetime spectroscopy on heavy ion irradiated stainless steels and tungsten, J. Nucl. Mater. 343 (2005) 330–332.

[104] T. Troev, E. Popov, P. Staikov, N. Nankov, T. Yoshiie, Positron simulations of defects in tungsten containing hydrogen and helium, Nucl. Instrum. Methods Phys. Res. B 267 (2009) 535–541.

[105] High Voltage Engineering Europa B.V., Manual for 3MV Tandetron accelerator, brochure, 2010.

[106] High Voltage Engineering Europa B.V., Tandetron accelerator system, brochure, 2010.

[107] G. Luo, W. M. Shu, H. Nakamura, S. O'Hira, M. Nishi, Ion species control in high flux deuterium plasma beams produced by a linear plasma generator, Rev. Sci. Instrum. 75 (2004) 4374–4378.

[108] N. Yao, Focused Ion Beam System, Basics and Applications, Cambridge University Press, Cambridge, 2007.

[109] http://mfwiki.ipp.mpg.de/index.php/Pww_rks, 2010.

[110] J. R. Tesmer, M. Nastasi, Handbook of Modern Ion Beam Materials Analysis, Material research society, Pittsburgh, Pennsylvania, 1995.

[111] M. Mayer, RESOLNRA: A new program for optimizing the achievable depth resolution of ion beam analysis methods, Nucl. Instrum. Methods Phys. Res. B 266 (2008) 1852–1857.

[112] H. M. Kuan, T. W. Bonner, J. R. Risser, An investigation of the $C^{12} + He^3$ reactions at bombarding energies between 1.8 and 5.4 MeV, Nucl. Phys. 51 (1964) 481–517.

[113] M. Mayer, SIMNRA User's Guide, Technical report, Report 9/113, Max-Planck-Institut für Plasmaphysik, Garching, 1997.

[114] R. A. Jarjis, Nuclear Cross Section Data for Surface Analysis, University of Manchester Press, Department of Physics, Manchester, 1979.

[115] V. K. Alimov, M. Mayer, J. Roth, Differential cross-section of the D(^3He, p)^4He nuclear reaction and depth profiling of deuterium up to large depths, Nucl. Instrum. Methods Phys. Res. B 234 (2005) 169–175.

[116] M. Mayer, E. Gauthier, K. Sugiyama, U. von Toussaint, Quantitative depth profiling of deuterium up to very large depths, Nucl. Instrum. Methods Phys. Res. B 267 (2009) 506–512.

[117] W. H. Press, S. A. Teukolsky, W. T. Vetterling, B. P. Flannery, Numerical Recipes, The Art of Scientific Computing, Cambridge University Press, Cambridge, 1986.

[118] R. Fischer, M. Mayer, W. von der Linden, V. Dose, Energy resolution enhancement in ion beam experiments with Bayesian probability theory, Nucl. Instrum. Methods Phys. Res. B 136-138 (1998) 1140–1145.

[119] U. von Toussaint, R. Fischer, K. Krieger, V. Dose, Depth profile determination with confidence intervals from Rutherford backscattering data, New J. Phys. 1 (1999) 11.1–11.13.

[120] G. M. Wright, M. Mayer, K. Ertl, G. de Saint-Aubin, J. Rapp, Hydrogenic retention in irradiated tungsten exposed to high-flux plasma, Internal Report, EFDA Task WP09-PWI-05-03/FOM, 2010.

[121] H. Eleveld, A. van Veen, Void growth and thermal desorption of deuterium from voids in tungsten, J. Nucl. Mater. 212-215 (1994) 1421–1425.

[122] V. K. Alimov, J. Roth, M. Mayer, Depth distribution of deuterium in single- and polycrystalline tungsten up to depths of several micrometers, J. Nucl. Mater. 337-339 (2005) 619–623.

[123] M. Fukumoto, Y. Ohtsuka, Y. Ueda, M. Taniguchi, M. Kashiwagi, T. Inoue, K. Sakamoto, Blister formation on tungsten damaged by high energy particle irradiation, J. Nucl. Mater. 375 (2008) 224–228.

[124] K. L. Wilson, D. N. Seidman, A field ion microscope study of the point defect structure of a depleted zone in ion W^+ irradiated tungsten, NBS, Gaithersburg, in: Proc. Conf. on Defects and Defect Clusters in bcc Metals and Their Alloys. Ed. R. J. Arsenault, 216–239, 1973.

[125] L. A. Beavan, R. M. Scanlan, D. N. Seidman, The defect structure of depleted zones in irradiated tungsten, Acta Metall. 19 (1971) 1339–1350.

[126] K. L. Wilson, M. I. Baskes, D. N. Seidman, An in situ field-ion microscope study of the recovery behavior of ion-irradiated tungsten and tungsten alloys, Acta Metall. 28 (1980) 89–102.

[127] C.-Y. Wei, M. I. Current, D. N. Seidman, Direct observation of primary state damage of ion-irradiated tungsten, I. Three-dimensional spatial distribution of vacancies, Philos. Mag. 44 (1981) 459–491.

[128] R. M. Scanlan, D. L. Styris, D. N. Seidman, An in situ field ion microscope study of irradiated tungsten I. Experimental results, Philos. Mag. 23 (1971) 1439–1457.

[129] R. M. Scanlan, D. L. Styris, D. N. Seidman, An in situ field ion microscope study of irradiated tungsten, II. Analysis and interpretation, Philos. Mag. 23 (1971) 1459–1478.

[130] T. Terao, Y. Hayashi, H. Yosida, Y. Yashiro, FIM observation of radiation damages in neutron-irradiated W, Scr. Metall. 12 (1978) 827–829.

[131] K. Lacefield, J. Moteff, J. P. Smith, Neutron radiation damage in tungsten single crystals, Philos. Mag. 13 (1966) 1079–1081.

[132] R. C. Rau, R. L. Ladd, J. Moteff, Voids in irradiated tungsten and molybdenum, J. Nucl. Mater. 33 (1969) 324–327.

[133] N. Igata, K. Shibata, S. Sato, Fim observation of defect clusters in tungsten irradiated with 200 keV C ion, Radiat. Eff. Defects Solids 41 (1979) 251–260.

[134] R. C. Rau, Vacancy dislocation loops in irradiated and annealed tungsten, Philos. Mag. 18 (1968) 1079–1084.

[135] V. K. Alimov, J. Roth, R. A. Causey, D. A. Komarov, C. Linsmeier, A. Wiltner, F. Kost, S. Lindig, Deuterium retention in tungsten exposed to low-energy high-flux clean and carbon-seeded deuterium plasmas, J. Nucl. Mater. 375 (2008) 192–201.

[136] A. A. Haasz, J. W. Davis, Deuterium retention in beryllium, molybdenum and tungsten at high fluences, J. Nucl. Mater. 241-243 (1997) 1076–1081.

[137] M. Poon, A. A. Haasz, J. W. Davis, Modelling deuterium release during thermal desorption of D^+-irradiated tungsten, J. Nucl. Mater. 374 (2008) 390–402.

[138] R. Kirchheim, Solubility and diffusivity of hydrogen in complex materials, Phys. Scr. T94 (2001) 58–67.

[139] R. A. Causey, The interaction of tritium with graphite and its impact on tokamak operations, J. Nucl. Mater. 162-164 (1989) 151–161.

[140] H. Atsumi, T. Tanabe, Hydrogen retention in high-Z materials with various contents of carbon, J. Nucl. Mater. 258-263 (1998) 896–901.

[141] H. Kimura, Y. Nishikawa, T. Nakahata, M. Oyaidzu, Y. Oya, K. Okuno, Chemical behavior of energetic deuterium implanted into tungsten carbide, Fus. Eng. Des. 81 (2006) 295–299.

[142] V. K. Alimov, K. Ertl, J. Roth, K. Schmid, Retention of ion-implanted deuterium in tungsten pre-irradiated with carbon ions, J. Nucl. Mater. 282 (2000) 125–130.

[143] J. Luthin, C. Linsmeier, Carbon films and carbide formation on tungsten, Surface Sci. 454-456 (2000) 78–82.

[144] E. Igarashi, Y. Nishikawa, T. Nakahata, A. Yoshikawa, M. Oyaidzu, Y. Oya, K. Okuno, Dependence of implantation temperature on chemical behavior of energetic deuterium implanted into tungsten carbide, J. Nucl. Mater. 363-365 (2007) 910–914.

[145] T. Hino, F. Hirano, Y. Yamauchi, Y. Hirohata, Hydrogen retention and erosion of carbon-tungsten mixed material, Fus. Eng. Des. .

[146] C. H. Skinner, A. A. Haasz, V. K. Alimov, N. Bekris, R. A. Causey, R. E. H. Clark, J. P. Coad, J. W. Davis, R. P. Doerner, M. Mayer, A. Pisarev, J. Roth, T. Tanabe, Recent advances on hydrogen retention in ITER's plasma-facing materials: beryllium, carbon, and tungsten, Fus. Sci. Tech. 54 (2008) 891–921.

[147] W. R. Wampler, R. P. Doerner, Deuterium retention in tungsten from exposure to plasma, Phys. Scr. T138 (2009) 014037.

[148] A. Singh, W. S. Khokle, K. Lal, Structural and material properties of tungsten silicide formed at low temperature, Vac. 45 (1994) 867–869.

[149] A. H. M. Krom, A. D. Bakker, Hydrogen trapping models in steel, Metall. Mater. Trans. B 31 (2000) 1475–1482.

[150] M. R. Mruzik, K. C. Russell, Equilibrium forms of small voids in metals, Surface Sci. 67 (1977) 205–225.

[151] FEI Company, application note, High-resolution imaging on C_s-corrected Titan^{TM} 80-300, 2010.

[152] Prof. dr hab. K.I. Wysokiński, UMCS Lublin, Poland, private communication, 2010.